Institut National de la Recherche Scientifique
Centre Énergie, Matériaux et Télécommunications
and
University of Applied Sciences Munich
Faculty 06: Micro- and Nanotechnology

Developing Instrumentation for High Temperature In Situ Transmission Electron Microscope Measurements and Stability Study of TiO_2

Master Thesis
Winter Term 2024/25

Name:	Philipp Wieland
Program:	Master's in Energy and Material Sciences at INRS Master's in Micro- and Nanotechnologies at HM
Director INRS:	Prof. Dr. Kenneth Beyerlein
Director HM:	Dr. Constanze Eulenkamp

Submission Date
14th October, 2024

Abstract

This thesis focuses on two main aspects: the development of an external viewing screen camera system for transmission electron microscopy and the investigation of the anatase-rutile phase transformation in TiO_2. The external camera system, designed as a robust alternative to the internal post-GIF camera, was calibrated and compared in terms of magnification, contrast, field of view, and measurement accuracy. While the internal camera provided higher resolution and contrast, the external system offered a significantly larger field of view and improved durability, making it a reliable addition to the microscope.

In parallel, the Protochips Aduro heating system was used to heat powdered TiO_2 nanoparticles during in situ TEM experiments to observe the complete transformation from anatase to rutile. Although slight phase changes were observed, full transformation was not achieved due to inaccuracies in the calibration of the heating system, as evidenced by the failure to reach the melting points of sputtered aluminum (660.3 °C) and zinc nanoparticles (419.5 °C). The actual temperature was estimated to be around 400 °C at a target temperature of 1000 °C. Future work will focus on recalibrating the heating system to ensure accurate temperature control and allow further studies of phase transformations in TiO_2.

Kurzzusammenfassung

Diese Arbeit konzentriert sich auf zwei Hauptaspekte: die Entwicklung eines externen Kamerasystems für die Transmissionselektronenmikroskopie und die Untersuchung der Phasenumwandlung von Anatas-Rutil in TiO_2. Das externe Kamerasystem wurde als robuste Alternative zur internen Post-GIF Kamera entwickelt, kalibriert und hinsichtlich Vergrößerung, Kontrast, Sichtfeld und Messgenauigkeit verglichen. Während die interne Kamera eine höhere Auflösung und einen besseren Kontrast lieferte, bot das externe System ein deutlich größeres Sichtfeld und eine bessere Haltbarkeit, was es zu einer zuverlässigen Ergänzung des Mikroskops machte.

Parallel dazu wurde das Aduro-Heizsystem von Protochips verwendet, um pulverisierte TiO_2-Nanopartikel während In-situ-TEM-Experimenten zu erhitzen, um die vollständige Umwandlung von Anatas zu Rutil zu beobachten. Obwohl leichte Phasenveränderungen beobachtet wurden, konnte die vollständige Umwandlung aufgrund von Ungenauigkeiten bei der Kalibrierung des Heizsystems nicht erreicht werden, wie das Nichterreichen der Schmelzpunkte von gesputtertem Aluminium (60,3 Grad Celsius) und Zink-Nanopartikeln (419,5 Grad Celsius) beweist. Die tatsächliche Temperatur wurde auf etwa 400 Grad Celsius bei einer Zieltemperatur von 1000 Grad Celsius geschätzt. Zukünftige Arbeiten werden sich darauf konzentrieren, das Heizsystem neu zu kalibrieren, um eine genaue Temperaturkontrolle zu gewährleisten und weitere Untersuchungen der Phasenumwandlungen in TiO_2 zu ermöglichen.

Résumé

Cette thèse se concentre sur deux aspects principaux : le développement d'un système de caméra externe pour la microscopie électronique à transmission et l'étude de la transformation de phase anatase-rutile dans le dioxyde de titane (TiO2). Le système de caméra externe, conçu comme une alternative robuste à la caméra interne post-GIF, a été étalonné et comparé en termes de grossissement, de contraste, de champ de vision et de précision de mesure. Alors que la caméra interne offrait une résolution et un contraste plus élevés, le système externe offrait un champ de vision nettement plus large et une meilleure durabilité, ce qui en faisait un complément fiable au microscope.

Parallèlement, le système de chauffage Protochips Aduro a été utilisé pour chauffer des nanoparticules de titane dioxyde (TiO2) en poudre pendant des expériences TEM in situ, afin d'observer la transformation complète de l'anatase en rutile. Bien que de légers changements de phase aient été observés, la transformation complète n'a pas été réalisée en raison d'imprécisions dans l'étalonnage du système de chauffage. L'impossibilité d'atteindre les points de fusion des nanoparticules d'aluminium (660,3 °C) et de zinc (419,5 °C) pulvérisées en est la preuve. La température réelle a été estimée à environ 400 °C pour une température cible de 1000 °C. Les travaux futurs porteront sur le recalibrage du système de chauffage afin de garantir un contrôle précis de la température et de permettre d'autres études sur les transformations de phase dans le dioxyde de titane.

Synopsis

The synopsis is a concise French version of the Master's thesis, covering everything from the introduction to the conclusion. It highlights the main themes and important points discussed, and explains the working hypotheses that guided the research. It also outlines the main research objectives, describes the methods used, and summarizes the main findings and results. The aim of this summary is to provide the reader with a clear understanding of the main contributions of the thesis and insights into the research conducted.

Le synopsis est une version française concise du mémoire de master qui couvre l'ensemble du document, de l'introduction à la conclusion. Il met en évidence les principaux thèmes et les points importants abordés, en expliquant les hypothèses de travail qui ont guidé la recherche. Il expose également les principaux objectifs de la recherche, décrit les méthodes utilisées et résume les principales conclusions et les résultats. Ce résumé a pour but de permettre au lecteur de bien comprendre les principales contributions de la thèse ainsi que les perspectives de la recherche menée.

1 Introduction

Le dioxyde de titane (TiO_2) ou titane est un matériau largement utilisé en raison de ses propriétés polyvalentes et de ses applications dans des domaines tels que la photocatalyse, les cellules solaires, le stockage de l'énergie et les pigments (Lee and Zuo, 2004). Les deux principales phases du dioxyde de titane sont l'anatase et le rutile. Le rutile est thermodynamiquement stable, tandis que l'anatase est métastable et se transforme en rutile lorsqu'elle est chauffée (Hanaor and Sorrell, 2011). Cette transformation de phase affecte significativement les propriétés optiques et électroniques du matériau, qui sont critiques pour l'efficacité du matériau dans des applications telles que la photocatalyse et le photovoltaïque (Koparde and Cummings, 2008).

L'étude des transformations de phase du dioxyde de titane est essentielle pour comprendre comment des facteurs tels que la température, la taille des particules et les conditions environnementales affectent les changements structurels (Hanaor and Sorrell, 2011). Le microscope électronique à transmission (eng. Transmission Electron Microscope (TEM)) est l'un des outils les plus efficaces pour observer ces transformations en temps réel à l'échelle atomique, en particulier pour la transition anatase-rutile.

Cette thèse se concentre sur deux aspects: (1) le développement et l'étalonnage d'un système de caméra externe à écran de visualisation (eng. Viewing Screen (VS)) pour étendre les capacités d'imagerie du MET, et (2) l'étude de la transformation de phase anatase-rutile du titane dans des conditions de chauffage contrôlées. La caméra VS externe offre un champ de vision plus large et une durabilité améliorée par rapport à la caméra interne post-GIF. Elle a été testée et comparée en termes de niveaux de grossissement, de contraste, de champ de vision et de précision des mesures.

En outre, un système de chauffage Protochips a été utilisé pour appliquer une chaleur contrôlée à AEROXIDE® TiO_2 P25, une forme commerciale de dioxyde de titane d'Evonik avec une taille de particule de 24 nm. L'objectif était d'observer la transformation complète de l'anatase en rutile à des températures supérieures à 400 °C (Czanderna et al., 1958). Le chauffage de l'échantillon dans le MET a permis d'observer en temps réel les changements structurels à la fois en mode image et en mode diffraction.

Cependant, le système de chauffage Protochips n'a pas atteint les températures attendues, comme en témoigne son incapacité à faire fondre les nanoparticules de zinc et d'aluminium pulvérisé, dont les points de fusion sont respectivement de 419.5 °C et 660.3 °C (American Elements, 2024). Cet écart suggère une erreur d'étalonnage dans le système, qui n'a entraîné qu'une transformation partielle de l'anatase en rutile, ce qui nécessite un nouvel étalonnage.

2 Principes de base de la microscopie électronique à transmission

L'étude des nanoparticules de titane nécessite un microscope à haute résolution, tel que le microscope électronique à transmission JEOL JEM-2100Plus. Ce chapitre donne un aperçu de la fonctionnalité de la MET, en se concentrant sur les caractéristiques clés requises pour les études de transformation de phase in situ du titane.

2.1 Microscope

Le microscope électronique à transmission JEOL JEM-2100Plus, modifié pour les mesures dynamiques résolues dans le temps, est un outil puissant pour l'imagerie et la manipulation de la matière à l'échelle micro et nanométrique. Fonctionnant dans un vide poussé, il génère des images en détectant les signaux provenant de l'interaction entre un faisceau d'électrons et l'échantillon (Beun, 1994). La Figure 2.1 illustre les principaux composants du MET: le canon à électrons LaB6 (a), qui génère le faisceau d'électrons, et une série de lentilles électromagnétiques — condenseur (b), objectif (c) et projecteur (d) — qui focalisent le faisceau et le guident à travers l'échantillon (e) (Luo, 2016).

Les électrons transmis forment une image qui est projetée sur l'écran phosphorescent (f), également appelé écran de visualisation, qui émet une lumière verte. Cette image peut également être projetée sur une caméra (g) placée sous le VS. L'écran de visualisation peut être soulevé pour révéler la caméra, qui la protège ainsi des dommages potentiels causés par le faisceau à haute énergie. La caméra Gatan Ultrascan, connectée à un ordinateur, capture des images en mode Gatan Imaging Filter (GIF). Dans ce mode, le faisceau d'électrons est orienté de manière à guider les électrons du faisceau vers le capteur de la caméra à travers une colonne située sous le VS. En mode non GIF, l'image est projetée sur le VS.

Outre la formation d'images, le faisceau d'électrons génère des signaux secondaires qui peuvent être utilisés pour la microscopie électronique analytique afin d'obtenir des informations sur les propriétés chimiques et structurelles de l'échantillon (Williams and Carter, 2008). Comme le montre la Figure 2.2, ces signaux comprennent le faisceau direct, qui est utilisé pour l'imagerie, et les électrons diffusés de manière élastique, qui sont essentiels pour produire des figures de diffraction.

Les échantillons TEM ont généralement une taille comprise entre le μm^2 et le nm^2 et doivent répondre à des exigences spécifiques. Ils doivent notamment être suffisamment fins pour permettre la transmission des électrons et résister à un vide poussé. Ces échantillons sont montés sur des grilles TEM spécialisées, dont le matériau, l'espacement et la fonctionnalité varient en fonction de l'application (Pella, n.d.). Différents porte-échantillons sont disponibles pour manipuler et positionner l'échantillon en vue d'une analyse in situ.

2.2 Imagerie

La méthode d'imagerie d'un MET est similaire à celle d'un microscope à lumière transmise, qui projette la lumière sur un écran à travers un échantillon (semi-)transparent (Murphy, 2012). Dans un MET, cependant, les électrons traversent l'échantillon pour former l'image. La luminosité dépend de l'intensité du faisceau d'électrons, tandis que le contraste dépend du contraste de phase dû à la diffusion des électrons (Lee and Zuo, 2011). Ce chapitre se concentre sur le mode GIF, car le mode non-GIF sera abordé ultérieurement lors de la mise en service de la caméra VS externe.

Le MET offre une large gamme de grossissements (JEOL, n.d.). À faible grossissement (x150 à x1500), il affiche des caractéristiques de l'ordre du micromètre, utiles pour les vues d'ensemble. Les grossissements moyens (x2000 à x10k) permettent de suivre les changements de forme des particules, tandis que les grossissements plus élevés (x12k à x30k) révèlent les détails à l'échelle nanométrique. Les grossissements les plus élevés (x40k à x120k) permettent de distinguer les couches atomiques individuelles, ce qui est essentiel pour la caractérisation des cristaux et les mesures de l'espacement atomique. Cela est particulièrement utile pour étudier les transformations de phase telles que la transition anatase-rutile dans des particules uniques. La Figure 2.3 illustre ces grossissements.

2.3 Diffraction

La capacité de la MET à produire des diagrammes de diffraction fournit des informations importantes sur la structure cristalline d'un échantillon, en particulier sur sa nature cristalline (Borchardt-Ott and Sowa, 2018). Le réseau cristallin agit comme un réseau de diffraction et, lorsque le faisceau d'électrons le traverse, il crée des figures d'interférence spécifiques au matériau et à la phase. Ces figures se manifestent sous forme de taches (provenant de grains uniques avec un ordre à longue portée) ou d'anneaux (provenant de cristaux multiples avec des orientations différentes) (Fultz and Howe, 2013). Le rayon et l'intensité des anneaux dépendent de l'angle de diffraction et de la longueur de la caméra, comme le montre la Figure 2.4.

Les angles de diffraction ($2\,\theta$) sont calculés à l'aide de la condition de Bragg, qui décrit l'interférence constructive des ondes diffusées par les plans atomiques. L'équation de la condition de Bragg (Équation 1) relie la longueur d'onde des électrons (λ), qui est de 2,508 pm à 200 kV, à l'espacement des plans du réseau (d) et à l'angle de diffraction θ. En mode diffraction, le faisceau direct est bloqué par un obturateur de faisceau afin de protéger la caméra de son intensité élevée.

La figure de diffraction est particulièrement utile pour distinguer les phases anatase et rutile du titane, car leurs paramètres de réseau diffèrent. L'observation de ces figures permet d'étudier in situ des transformations de phase telles que la transition anatase-rutile.

3 Mise en service de la caméra de l'écran de visualisation externe

Un TEM projette généralement des images via l'écran de visualisation (VS) ou une caméra intégrée. À l'INRS, la caméra intégrée est la norme pour les mesures en mode imagerie et diffraction. Pour capturer des images VS, une caméra externe doit être installée. L'objectif de cette caméra externe VS est de fournir une méthode de mesure alternative et de permettre des applications supplémentaires qui ne sont pas possibles avec la caméra intégrée. Compte tenu de la fragilité de la caméra GIF, la nouvelle caméra devrait également servir de solution de secours en cas de dommage. Ce chapitre est consacré à l'intégration de la caméra externe, à l'évaluation de ses caractéristiques et à la comparaison de ses avantages et inconvénients avec la caméra TEM post-GIF.

3.1 Étalonnage de la caméra externe

Ce chapitre décrit l'installation de la caméra externe VS, le flux de travail de la capture d'images à l'analyse, et l'étalonnage de la barre d'échelle pour différents grossissements et longueurs de caméra en mode non GIF.

3.1.1 Installation du nouveau système de caméra

Un appareil photo reflex numérique à objectif unique (eng. Digital Single-Lens Reflex (DSLR)) a été choisi pour capturer les images du VS en raison de son adaptabilité et de sa résolution élevées. Le modèle spécifique choisi est le Nikon D60, équipé d'un objectif Nikon "AF-P DX NIKKOR 18-55mm f/3.5-5.6G VR". Les paramètres de l'appareil photo, tels que la sensibilité ISO, l'ouverture et la vitesse d'obturation, peuvent être ajustés en fonction de la lumière ambiante et de l'intensité de la lumière émise par le VS.

Avant d'installer l'appareil photo, la monture doit être configurée. Il est important de bien positionner la caméra devant le VS et de s'assurer qu'elle est à la bonne hauteur pour capturer toute la surface de l'écran. En raison de l'espace limité sur la table devant le VS, il n'est pas possible d'utiliser un trépied disponible dans le commerce. Un trépied personnalisé est donc construit à l'aide de composants optomécaniques de Thorlabs. La configuration finale est présentée à la Figure 3.1.

Pour garantir une imagerie optimale, le point focal de l'appareil photo doit être aligné sur le centre du VS. La longueur focale est fixée à 35 mm pour englober l'ensemble de la VS. La sensibilité ISO, réglage de gain numérique indiquant la sensibilité à la lumière du capteur d'image, varie de 100 à 1600 sur le Nikon D60. Les valeurs ISO inférieures produisent moins de bruit, mais nécessitent plus de lumière, tandis que les valeurs supérieures permettent d'augmenter la luminosité au détriment du bruit.

L'ouverture de l'objectif, indiquée par le "nombre-f", contrôle la quantité de lumière passant à travers l'objectif et affecte la profondeur de champ de l'image. Sur le Nikon D60, l'ouverture peut varier de f/3,5 à f/38. Une ouverture plus petite permet une plus grande profondeur de champ, mais moins de lumière, tandis qu'une ouverture plus grande permet plus de lumière, mais réduit la profondeur de champ.

Le temps d'exposition est contrôlé par la vitesse d'obturation, qui détermine la durée d'exposition du capteur d'image à la lumière. Le Nikon D60 offre des vitesses d'obturation allant de 1/4000 à 30 s. Les vitesses d'obturation plus courtes réduisent la luminosité mais minimisent le flou de bougé, tandis que les vitesses d'obturation plus longues permettent d'obtenir des images plus lumineuses.

Une fois l'appareil photo configuré, les réglages d'ouverture et d'ISO peuvent rester constants, seule la vitesse d'obturation devant être ajustée en fonction de la luminosité ambiante. La première étape consiste à déterminer l'ouverture optimale, en équilibrant la profondeur de champ et l'apport de lumière. Des tests ont été effectués avec des réglages d'ouverture allant de f/5 à f/32, comme le montre la Figure 3.2.

Les résultats des tests d'ouverture indiquent que le réglage optimal est f/8, où la profondeur de champ couvre correctement l'ensemble du VS et où le temps d'exposition peut être raisonnablement réduit à 5 s pour une image de haute qualité. La sensibilité ISO a ensuite été évaluée de 100 à 1600, les résultats étant présentés dans la Figure 3.3.

Les tests montrent que la sensibilité ISO 800 offre le meilleur équilibre entre bruit et qualité. Si la sensibilité ISO 100 produit un bruit minimal, elle nécessite un temps d'exposition maximal de 30 s, ce qui limite la flexibilité. La sensibilité ISO 1600 réduit le temps d'exposition à 2,5 s, mais introduit un bruit important, ce qui compromet la qualité de l'image. À 800 ISO, le temps d'exposition est réduit à 5 s tout en maintenant des niveaux de bruit acceptables.

Le temps d'exposition doit pouvoir être adapté en raison des variations de la lumière ambiante et des différences entre les modes image et diffraction dans le MET, qui affectent la luminosité et le contraste. En règle générale, le temps d'exposition est fixé à environ 2,5 s pour le mode image et à 10 s pour le mode diffraction.

Après avoir configuré avec succès le reflex numérique et optimisé les paramètres d'imagerie, il est possible de capturer des images de haute qualité. Les réglages optimaux comprennent une ouverture de f/8, une sensibilité ISO de 800 et des vitesses d'obturation réglables en fonction du mode. Les images capturées sont enregistrées au format JPEG à une résolution de 3872 x 2592 pixels.

3.1.2 Processus de correction de la perspective

Les images prises à un angle de 45° produisent une perspective déformée qui doit être corrigée pour minimiser les erreurs de mesure. Le logiciel choisi pour cette tâche est DxO Viewpoint, qui corrige efficacement la perspective de l'image, rapidement et facilement. Son interface utilisateur est présentée dans la Figure 3.4.

Dans la Figure 3.4, un exemple d'image DSLR est montré à gauche, tandis que les paramètres de correction de la perspective sont mis en évidence à droite. Ce processus de correction utilise l'option "Rectangle", qui permet à l'utilisateur de superposer une forme rectangulaire aux coins de l'écran. Cette forme sert de référence au logiciel pour ajuster automatiquement l'image à la bonne perspective. En outre, l'option "Ratio H/V" permet d'affiner la correction.

La Figure 3.5 montre les résultats de la correction de la perspective. À gauche, l'image originale prise avec le reflex numérique; à droite, l'image corrigée. Dans la version corrigée, un rectangle blanc est créé et aligné sur les coins extérieurs du VS. Le logiciel manipule l'image de manière à ce que les angles à l'intérieur du rectangle soient ajustés à 90°, assurant ainsi une représentation plus précise de la perspective originale.

Pour vérifier la précision de la correction de la perspective, on peut examiner le rapport entre la longueur et la hauteur du rectangle sur le VS. Par exemple, la longueur est de 78 mm et la hauteur de 56 mm, ce qui donne un rapport de 1,39. Ce rapport peut être vérifié en mesurant les pixels de l'image corrigée. S'il y a des divergences, elles peuvent être corrigées à l'aide du réglage du rapport H/V. En règle générale, tout ajustement du rapport H/V modifie de 0,01 le rapport du rectangle dans l'image manipulée.

3.1.3 Étalonnage

Après avoir optimisé les réglages du reflex numérique, l'étape suivante consiste à étalonner la barre d'échelle de l'écran de visualisation (VS) pour chaque grossissement en mode image et chaque longueur de caméra en mode diffraction. L'étalonnage est essentiel pour obtenir des mesures précises et nécessite une pièce normalisée aux dimensions connues (DIN e.V., 1995). Un réseau en or pur avec un pas fixe de 2 160 lignes par mm, donnant un pas de 463 nm entre deux lignes, est utilisé à cette fin (Pella, n.d.).

Il est essentiel que tous les composants et les réglages restent cohérents pendant l'étalonnage, seuls le grossissement et la longueur de la caméra du MET variant. La position et les réglages du reflex numérique ainsi que la correction de la perspective doivent rester inchangés. Seul le temps d'exposition est ajusté pour correspondre aux différentes intensités lumineuses du VS dans les différents modes du MET, afin de garantir des images de même luminosité. Toutes les mesures de pixels ont été effectuées à l'aide d'ImageJ. Un exemple d'étalonnage en modes image et diffraction est illustré à la Figure 3.6.

Dans la Figure 3.6, le côté gauche montre l'étalon-or à un grossissement de x100k en mode image, tandis que le côté droit montre le même échantillon en mode diffraction à une longueur de caméra de 250cm. Les lignes rouges et bleues représentent les mesures prises dans ImageJ, où la ligne rouge correspond à la partie mesurée de l'échantillon et la ligne bleue indique la barre d'échelle.

L'étalonnage en mode diffraction se concentre sur la mesure du premier anneau de diffraction de l'or, qui a une structure cubique à faces centrées et une constante de réseau de a, b et c = 4.078 Å

(Wyckoff, 1963). L'espace d dans le plan [1 1 1] est calculé comme suit: $d1 = a/\sqrt{3}$, ce qui donne $d_1G = 2.356\,\text{Å}$. Cette valeur est convertie en espace réciproque avec $k = 1/d_1$, ce qui donne $k_G = 4.245\,1/\text{nm}$. Pour minimiser l'erreur de mesure des pixels, toute la surface du premier anneau est mesurée, comme le montre la Figure 3.6. Le rayon peut être calculé à l'aide de la formule $r = \sqrt{(surface/\pi)}$.

L'étalonnage de la barre d'échelle en mode image est divisé en deux parties: la première pour les grossissements où l'espacement des lignes est visible (x15k à x250k) et la seconde pour les grossissements plus élevés (x300k à x1,2M) en utilisant les défauts dans l'échantillon. Pour les distances de lignes visibles, la circonférence a été mesurée plutôt qu'une distance unique afin de réduire les erreurs d'étalonnage. La Figure 3.6 ci-contre en donne un exemple. Pour les grossissements plus importants, la distance réelle entre deux défauts ou points saillants est mesurée.

Dans la Figure 3.7, l'image de gauche montre un échantillon à un grossissement de 400k et l'image de droite le montre à un grossissement de 500k. La distance entre les zones mises en évidence est mesurée à l'aide d'une barre d'échelle calibrée à x400k. En utilisant des mesures de pixels, la barre d'échelle peut être étalonnée jusqu'à x1,2 M, bien que la précision de l'étalonnage diminue avec l'augmentation du grossissement en raison de facteurs tels que la correction de la perspective.

Pour étalonner la caméra VS externe, une première évaluation de l'erreur de mesure a été réalisée. L'installation est restée cohérente pendant plusieurs mesures, les variations n'étant introduites que par l'opérateur. À un grossissement de x60k, la distance entre deux lignes de l'étalon-or a été mesurée et s'est avérée être un minimum de 463 nm et un maximum de 472 nm. Cela donne une déviation maximale de 9 nm, soit une déviation relative de 2%, ce qui est inférieur à la limite acceptable de 5%.

En conclusion, la barre d'échelle a été étalonnée pour chaque grossissement et longueur de caméra du MET avec une erreur de mesure d'environ 2%. Cet étalonnage permet d'effectuer des mesures précises de l'échantillon à l'aide de la caméra VS externe, de sorte que les dimensions réelles peuvent être calculées sur la base de la barre d'échelle étalonnée et des dimensions en pixels des caractéristiques de l'échantillon et de la barre d'échelle. Le Tableau 3.1 donne un aperçu de tous les étalonnages pour chaque mode TEM, ce qui confirme que le système est configuré et prêt à servir d'alternative à la caméra TEM post-GIF.

3.2 Comparaison avec la caméra TEM post-GIF

Le microscope électronique à transmission (MET) est équipé d'une caméra intégrée qui est calibrée après chaque changement de filament. Elle est gérée par le programme "DigitalMicrograph", qui prend également en charge l'analyse. Cette section compare la caméra intégrée au nouveau modèle VS, en se concentrant sur les niveaux de grossissement, le champ de vision et le contraste. En outre, la précision des deux systèmes est évaluée, avec pour objectif une erreur de mesure inférieure à 5%.

3.2.1 Niveaux de grossissement

Le premier aspect examiné est celui des niveaux de grossissement dans les modes image et diffraction, chaque mode ayant un grossissement affiché et un grossissement réel. Le grossissement affiché se réfère aux valeurs affichées par le logiciel TEM, étiquetées "TEM Non-GIF Magnification"" et "TEM GIF Magnification"". En revanche, le grossissement réel correspond à l'image projetée de l'échantillon, étiquetée "VS Magnification" et "GIF Camera Magnification".

En mode GIF, les grossissements réels sont calibrés périodiquement et stockés dans DigitalMicrograph. Pour le mode non-GIF, le grossissement réel peut être calculé à partir de la longueur réelle de la barre d'échelle D0 (en mm) et de la longueur calibrée D1 (en nm) à l'aide de l'Équation (3).

Ce calcul est effectué pour chaque grossissement non GIF et les résultats sont résumés dans le Tableau 3.2, qui compare les grossissements affichés pour les deux systèmes. Les deux grossissements critiques sont surlignés en jaune, ce qui montre que les grossissements réels des caméras VS et GIF sont presque identiques, ce qui permet des comparaisons précises.

Pour le mode diffraction, le grossissement réel peut être dérivé de l'angle de diffraction $2\,\theta$ et du rayon R du premier anneau de diffraction, comme le montre la Figure 2.4. L'angle de diffraction est calculé en utilisant la condition de Bragg, la longueur d'onde des électrons dans le MET à 200 kV étant donnée comme $\lambda_(TEM) = 2.508\,\mathrm{pm}$ et l'espacement d de l'anatase dans le plan [101] comme $d_A = 3.516\,\text{Å}$. Le rayon R dans l'espace réel est calculé à partir de la barre d'échelle calibrée dans l'espace réciproque.

Ce calcul a été effectué pour chaque longueur de caméra en mode non-GIF, et les résultats sont présentés dans le Tableau 3.3, qui indique les longueurs de caméra affichées pour les deux systèmes. Un paramètre important est surligné en jaune, confirmant que les longueurs de caméra sont presque identiques, ce qui garantit des comparaisons précises en mode diffraction.

Les grossissements réels étant établis pour les deux systèmes de caméra en mode image et en mode diffraction, il est possible de comparer leurs capacités analytiques en se concentrant sur les réglages ayant le même grossissement réel, comme indiqué dans les Tableaux 3.2 et 3.3.

3.2.2 Champ de vision

Dans cette comparaison, le champ de vision (FOV) fait référence à la zone observable de l'échantillon à tout moment (Wright and Barrett, 2013) et dépend du nombre de pixels du capteur d'image et de la résolution des pixels. Alors que le nombre de pixels est constant pour chaque capteur, la résolution des pixels, qui correspond à la zone couverte par un seul pixel, varie avec le grossissement du MET. En mode non GIF, la longueur focale de l'objectif du reflex numérique affecte également la résolution des pixels, c'est pourquoi elle est fixée à 35 mm.

La forme de la zone observable diffère d'un système à l'autre: le VS capture une zone circulaire

$A = \pi * \frac{d_{sensor}^2}{4}$ tandis que la caméra GIF capture une zone carrée $A = d_{sensor}^2$, les deux dépendant du diamètre du capteur d'image (d_sensor). Le champ de vision peut être calculé pour n'importe quel grossissement à l'aide de l'Équation (6).

Le "NumberOfPxiels" fait référence au diamètre du capteur en pixels pour chaque système, tandis que la "pixel resolution" est dérivée de la barre d'échelle calibrée.

Si l'on compare les champs de vision à un même grossissement réel, la VS à x200k a une surface de 756 971 nm^2, tandis que la caméra GIF à x12k a une surface de 32 616 nm^2. Cela signifie que la VS a une surface 23 fois supérieure à celle de la caméra GIF. Le champ de vision plus large de la caméra VS permet d'examiner de plus grandes zones d'échantillons avec le même grossissement, ce qui constitue un avantage significatif.

3.2.3 Contraste

Le contraste fait référence à la différence de luminosité ou d'intensité entre les parties d'une image, ce qui est essentiel pour distinguer les caractéristiques (Rahimi-Nasrabadi et al., 2021). Il est compris entre 0 (noir) et 255 (blanc), les valeurs intermédiaires représentant des nuances de gris. Un contraste élevé améliore la visibilité du spécimen, avec un contraste maximal de 255 entre les pixels noirs et blancs. En micrographie numérique, un tracé d'intensité 1D le long d'une ligne sélectionnée permet de mesurer les différences d'intensité.

Pour la comparaison, les mêmes grossissements réels ont été utilisés: x80k (mode non-GIF) et x4k (mode GIF) en mode image, et 120cm et 10cm en mode diffraction. Les nanoparticules de TiO_2 ont été choisies pour l'échantillon en raison de leurs propriétés distinctes, qui permettent des mesures précises. La Figure 3.8 montre la zone de l'échantillon et les lignes de mesure du contraste, en comparant les images de la caméra VS et GIF.

La Figure 3.9 montre la différence d'intensité entre les particules et l'arrière-plan, le contraste de la VS culminant à 20 (différence entre 110 et 90) et celui du GIF à 115 (185 et 70). Le contraste moyen de la VS est de 15, tandis que celui du GIF est de 65. La Figure 3.10 compare le contraste entre deux particules avec un contraste VS de 11 et un contraste GIF de 87. En mode diffraction, le contraste a été mesuré sur le premier anneau de diffraction (Figure 3.11), la caméra GIF présentant un contraste plus élevé (36) que la VS (23). La Figure 3.12 présente le diagramme d'intensité en détail.

Dans l'ensemble, la caméra GIF offre un meilleur contraste dans les deux modes, ce qui améliore l'analyse, bien que le VS offre toujours un contraste suffisant pour l'examen. Bien que l'intensité varie en raison de facteurs externes, le rapport entre l'intensité et le contraste reste constant.

3.3 Résumé

La mise en place de la caméra externe du VS a commencé par le montage et l'étalonnage du reflex numérique sur un trépied personnalisé devant le VS. L'ouverture a été réglée sur f/8, l'ISO sur 800, avec des temps d'exposition variables – typiquement 2,5 s pour le mode image et 10 s pour le mode diffraction. DxO Viewpoint a été utilisé pour corriger la perspective, et ImageJ a été utilisé pour mesurer les pixels.

La caméra VS étalonnée a été comparée à la caméra TEM interne post-GIF en examinant des aspects clés tels que le grossissement, le champ de vision et le contraste, ainsi que l'erreur de mesure. Les deux systèmes ont leurs points forts. La caméra GIF offre un grossissement plus important (x2,1k à x1,5M), une meilleure résolution des pixels et un contraste plus élevé, avec une erreur de mesure de seulement 0,6% en mode diffraction et de -2,6% en mode image.

Par ailleurs, le reflex numérique offre un champ de vision beaucoup plus large - 23 fois plus grand que celui de l'appareil photo GIF au même grossissement. Il est également plus robuste, immunisé contre les dommages causés par le faisceau d'électrons, ce qui garantit un fonctionnement continu pendant l'opération TEM. Le système DSLR est plus facile à apprendre et à utiliser, avec moins de réglages et moins de risques de dommages.

4 Microscopie électronique à transmission in situ du dioxyde de titane

Après la mise en service réussie de la caméra VS externe, l'étude in situ de la stabilité thermique du titane peut commencer. Avant de commencer, il est important de comprendre le matériau et sa production. Le titane est synthétisé depuis les années 1940 (Evonik, 2017) et a été étudié pour la première fois par microscopie électronique dans les années 1950 (Czanderna et al., 1958). Il est donc nécessaire de faire un examen de l'évolution historique et des recherches récentes. Enfin, le système Protochips utilisé pour l'étude in situ est présenté.

4.1 Introduction au TiO_2

Le dioxyde de titane (TiO_2), également connu sous le nom de titane, est un composé inorganique présent naturellement dans les minéraux et souvent synthétisé industriellement (Koparde and Cummings, 2008). Il est composé d'un atome de titane et de deux atomes d'oxygène et se présente sous différentes phases: rutile, anatase et brookite (Hanaor and Sorrell, 2011). Ces phases diffèrent par leur structure atomique, ce qui se traduit par des propriétés différentes. Le rutile est la seule phase stable, tandis que l'anatase et la brookite sont métastables à toutes les températures. Les phases métastables peuvent se transformer en phase rutile stable lorsqu'une énergie supplémentaire est appliquée, un processus qui n'est pas réversible (Buschow et al., 2001). Cette discussion se concentrera sur la transformation de l'anatase en rutile, tandis que la brookite, une phase intermédiaire, ne sera pas examinée plus avant (Lee and Zuo, 2004).

Les propriétés uniques de chaque phase les destinent à des applications différentes. Le rutile est utilisé comme pigment blanc dans les peintures, les écrans solaires et les aliments (Ntsikelelo et al., 2020), tandis que l'anatase est privilégiée dans les cellules solaires, la photocatalyse et l'optoélectronique en raison de ses capacités d'oxydation et de réduction efficaces (Reyes-Coronado et al., 2008). L'utilité de l'anatase dans la décomposition des polluants organiques souligne l'importance de comprendre sa stabilité thermique, car ces propriétés sont perdues après la transformation en rutile.

L'anatase et le rutile appartiennent tous deux au système cristallin tétragonal, mais diffèrent par le groupe spatial et les paramètres de la cellule unitaire, le rutile étant plus compact (Rezaee et al., 2011). Leurs structures sont présentées dans la Figure 4.1 et les paramètres de leurs cellules unitaires sont indiqués dans le Tableau 4.1. La transformation de l'anatase en rutile commence généralement à 600 °C, mais la pression et la température influencent ce processus. La Figure 4.2 illustre l'effet de la pression sur la température de transformation, ce qui est pertinent pour les expériences in situ réalisées dans un environnement de vide poussé où la température de transformation reste autour de 600 °C (Hanaor and Sorrell, 2011). Plusieurs facteurs peuvent influencer cette température, tels que la taille et la forme des particules (rapport d'aspect), la surface, l'atmosphère, le volume de l'échantillon, le type de récipient, la vitesse de chauffage, le temps de trempage, la contamination (par les matières premières et le récipient) et la technique de mesure (Hanaor and Sorrell, 2011).

4.2 Production de dioxyde de titane

Avant d'examiner le comportement du titane dans diverses applications, il est essentiel de comprendre son processus de fabrication, car celui-ci influence considérablement les propriétés clés du matériau, telles que la taille, la forme et la surface des particules. Ces paramètres sont directement liés à la méthode de synthèse, les procédés industriels les plus courants étant les procédés au chlorure et au sulfate. L'AEROXIDE® TiO_2 P25 produit par Evonik (anciennement Degussa) est utilisé pour les expériences de cet article.

Evonik utilise un procédé pyrogénique, ou synthèse à la flamme, pour produire des oxydes métalliques tels que le dioxyde de titane (Evonik, 2017). Dans ce procédé, tous les réactifs, y compris le chlorure de titane ($TiCl_4$), sont vaporisés et introduits dans une flamme d'oxyhydrogène sous la forme d'un mélange homogène. Des oxydes métalliques sont formés par l'hydrolyse rapide du $TiCl_4$, tandis que du chlorure d'hydrogène (HCl) gazeux est produit comme sous-produit. La Figure 4.3 illustre le processus complet de synthèse par flamme des oxydes métalliques.

La synthèse commence par la vaporisation de $TiCl_4$, qui est mélangé à de l'air (principalement de l'oxygène) dans une chambre de mélange. Ce mélange est ensuite introduit dans un brûleur avec de l'hydrogène, ce qui entraîne son hydrolyse rapide. La réaction est résumée par l'Équation chimique (7).

Lorsque le mélange traverse la flamme, l'aérosol qui en résulte est refroidi et l'oxyde de titane en phase solide est séparé des sous-produits gazeux corrosifs, en particulier le HCl. L'élimination de l'acide chlorhydrique pendant la désacidification permet d'obtenir un produit pur. Les principales propriétés du TiO_2 produit, telles que la taille, la distribution et la surface des particules, sont largement déterminées au cours de cette synthèse à la flamme, qui peut être affinée en ajustant les concentrations des réactifs, la température de la flamme et le temps passé dans le brûleur.

Le modèle simplifié de formation de particules pendant la synthèse par flamme est illustré à la Figure 4.4. Ce modèle montre comment les nucléides (minuscules gouttelettes) se forment dans la flamme à partir du mélange de chlorure métallique, d'oxygène et d'hydrogène. Ces nucléides entrent en collision pour former des gouttelettes plus grosses, qui finissent par se solidifier en particules primaires. Lorsque la température baisse, les particules primaires s'agrègent, mais ne fusionnent pas complètement. Enfin, les agrégats coalescent pour former des agglomérats qui constituent le produit final. Le contrôle précis de ce processus permet la production d'oxydes métalliques de haute pureté avec des propriétés ciblées, y compris le contrôle de la composition proportionnelle des phases cristallines anatase et rutile.

L'AEROXIDE® TiO_2 P25 produit par ce procédé est composé d'environ 85% d'anatase et 15% de rutile. Malgré les températures élevées de la flamme (environ 2000 °C), la phase rutile, plus stable sur le plan thermodynamique, n'est présente qu'en petites quantités. En effet, le rutile se forme de préférence à la surface des particules, où il s'imbrique avec l'anatase. Le produit final se caractérise par une pureté de dioxyde de titane supérieure à 99,5%, obtenue par un recuit à 1000 °C pendant deux heures pour éliminer l'eau physisorbée et chimisorbée.

La taille moyenne des particules d'AEROXIDE® TiO_2 P25 est d'environ 24 nm avec une déviation standard de 5 nm, ce qui le rend adapté aux applications techniques nécessitant une surface spécifique élevée. En raison de sa finesse, le P25 n'a pas les propriétés de pigment généralement associées au dioxyde de titane, mais il est particulièrement utile comme support de catalyseur, dans les réactions photocatalytiques et comme stabilisateur thermique pour les silicones.

4.3 Modifications du TiO_2 en fonction du temps à des températures élevées

La production de titane par hydrolyse à la flamme remonte à 1940, et les études sur la transformation des phases à l'aide de la microscopie électronique ont débuté dans les années 1950. Les recherches se poursuivent, notamment sur le potentiel de la phase anatase pour les applications énergétiques durables. Malgré des études approfondies, la stabilité thermique de l'anatase reste incomprise en raison des nombreux facteurs qui l'influencent.

La transformation anatase-rutile a été étudiée par Czanderna et al. (1957), qui ont montré une transformation complète à 728 °C pendant 4 h. En dessous de 610 °C, le taux de transformation est lent et augmente de manière significative au-dessus de 730 °C. Le temps, la température et les impuretés ont été identifiés comme des facteurs d'influence, mais l'atmosphère n'a pas eu d'effet significatif. Cependant, Iida et al. (1961) ont constaté que la pression affectait légèrement la transformation à 900 °C dans l'oxygène, l'air et l'argon, sans affecter la croissance des grains. En 1966, Vahldieic a constaté une diminution du taux de transformation avec l'augmentation de la pression à un taux de $dTdP = -0.02\,^{\circ}\mathrm{C\,bar^{-1}}$.

Les recherches de Gribb et al. (1997) ont montré que les particules d'anatase les plus fines (taille moyenne de 25 nm) se transforment plus rapidement, 80% d'entre elles étant transformées à 525 °C après 24 h. Ces résultats confirment les conclusions antérieures selon lesquelles les particules plus petites inversent les stabilités de phase. En 2001, Gouma et al. ont étudié des poudres de dioxyde de titane disponibles dans le commerce (taille moyenne de 100 nm) et ont observé une transformation complète de la phase après 8 h à 1000 °C. Ils ont proposé trois scénarios de transformation (Figure 4.5). En 2004, Lee et al. ont constaté que la croissance du rutile était accélérée par l'absorption de l'anatase environnante à 750 °C.

D'autres études menées par Hu et al. (2003) ont montré une relation presque linéaire entre la taille des particules d'anatase et le taux de transformation (Figure 4.6). La taille critique pour la transformation était de 15 nm, les particules plus grosses étant plus susceptibles de se transformer. Ayache et al. (2010) ont confirmé cette hypothèse en constatant que les particules plus petites (32 nm en moyenne) se transformaient plus rapidement que les plus grosses, la transformation se produisant à 650 °C.

En 2020, Ntsikelelo et al. ont observé des changements de taille de particules dans les nanoparticules de titane, confirmant l'existence d'une phase hybride anatase-rutile à 400 °C. Bachina et al. (2021) ont étudié le processus de transformation et ont constaté une transition complète anatase-rutile entre 700 °C et 900 °C (Figure 4.7).

Dans l'ensemble, des facteurs tels que la taille des particules, la température et l'orientation influencent la transformation, les particules plus petites présentant une stabilité accrue. Cependant, la taille critique exacte pour la transition anatase-rutile reste incertaine. La compréhension du comportement de l'AEROXIDE® TiO_2 P25 d'Evonik est essentielle pour isoler ces propriétés et leur rôle dans le processus de transformation.

4.4 Système de chauffage in situ

Le support Aduro de Protochips, associé à la puce électronique Fusion Select Heating (E-FHDS-VO-10), permet un traitement thermique in situ et des études de stabilité thermique du titane à l'intérieur du MET. Cela permet l'observation en temps réel des transitions de phase et des changements structurels jusqu'à 1000 °C (Protochips, n.d.(b)). Protochips est spécialisé dans le contrôle in situ, produisant des supports et des puces pour la manipulation thermique et électrique dans les microscopes électroniques, ce qui est essentiel pour étudier la transformation anatase-rutile.

La puce électronique Fusion-Select-Heating, qui mesure 4 mm x 4,65 mm x 300 µm, possède une membrane en nitrure de silicium de 40 nm avec neuf trous de 8 µm pour la transparence des électrons. La puce est fournie avec des numéros de série uniques et des fichiers d'étalonnage (Protochips, 2020). La Figure 4.8 montre la structure de la puce, dans laquelle le chauffage par effet Joule se produit lorsqu'un courant électrique est appliqué, permettant des montées en température rapides jusqu'à 1000 °C par minute (Protochips, n.d.(b)).

Le porte-échantillon Aduro (Figure 4.9) relie la puce aux périphériques. Quatre broches métalliques se connectent à l'alimentation Keithley et permettent le contrôle via le logiciel Fusion 500 (Figure 4.10). Le logiciel gère la température, le temps et les conditions expérimentales, tandis que la vérification du dispositif assure l'intégrité du système avant de commencer l'expérience (Protochips, n.d.(e)). Dans le "Channel A Setup" (Figure 4.11), les utilisateurs définissent les paramètres de l'expérience tels que la température, les taux de chauffage et les cycles afin de garantir un contrôle précis pendant les études thermiques.

5 Étude de la transformation de phase du dioxyde de titane

Après avoir présenté le titane, passé en revue l'état actuel de la technique et décrit le système Protochips pour les expériences in situ dans le TEM, l'étude va maintenant se concentrer sur la stabilité thermique du titane. L'objectif est d'étudier la transformation de l'anatase en rutile dans des conditions variables de temps et de chaleur. La préparation et la procédure expérimentale seront décrites, puis une discussion détaillée des résultats sera proposée. Comme les résultats diffèrent de ceux généralement rapportés dans la littérature, une analyse approfondie des sources d'erreur potentielles est effectuée pour identifier les raisons possibles de ces divergences.

5.1 Procédure expérimentale

La stabilité thermique du titane est étudiée à l'aide du système Protochips avec le porte-échantillon Aduro et la puce électronique Fusion Select Heating (numéro de série FS40486-9), en utilisant Evonik AEROXIDE® TiO2 P25 avec une taille moyenne de particules de 24 nm.

La préparation de l'échantillon implique la dilution de la poudre de titane dans une solution pour permettre son application sur la membrane de la puce (Protochips, n.d.(d)). En raison de l'agglomération au cours de la fabrication, les particules sont trop grosses pour permettre une observation efficace (Evonik, 2017). La dilution améliore la dispersion de l'échantillon, ce qui est bénéfique pour l'imagerie TEM, et utilise généralement de l'acétone comme solvant (Lee and Zuo, 2004 ; Lee and Zuo, 2011). Un mélange de 3 ml d'acétone et d'une pointe de microspatule de poudre de titane est sonifié pendant 60 minutes (Protochips, n.d.(c)), puis appliqué sur la membrane de la puce électronique. Il faut ensuite le laisser s'évaporer complètement pour éviter tout problème dans la chambre à vide du TEM.

Après la préparation de l'échantillon, le système Protochips doit être mis sous tension pendant une heure (Protochips, n.d.(b)). Le porte-échantillon Aduro est monté et placé dans le MET avec des câbles reliant le porte-échantillon, l'alimentation électrique et l'ordinateur. Le fichier d'étalonnage de la puce électronique est chargé après une vérification réussie de l'appareil.

Pour commencer l'étude de stabilité thermique, veuillez suivre les recommandations du fabricant. Evonik indique que la phase anatase se transforme complètement en rutile à 800 °C après 3 h (Evonik, 2017). Ayache et al. (2010) rapportent une transformation complète à 900 °C pour des particules de taille similaire. Plusieurs expériences sont réalisées à des températures comprises entre 800 °C et 1000 °C, chacune pendant 3 h. Cette plage couvre les capacités du système Protochips, est cohérente avec les études précédentes et donne un aperçu des changements de comportement avec l'augmentation de la température.

5.2 Discussion des résultats

La même partie de l'échantillon a été observée à la fois en mode image et en mode diffraction, révélant des changements dans la taille et la forme des particules, ainsi que la transformation de la structure cristalline de l'anatase en rutile à des grossissements élevés. En mode image (Figure 5.1), l'emplacement initial de l'échantillon (a) présentait des particules bien réparties avec des "lacs" distincts qui ont servi de points de repère pour chaque expérience. Après un chauffage de 3 h à 800 °C (b), 900 °C (c) et 1000 °C (d), des changements significatifs dans la forme et la distribution des particules ont été observés, en particulier à 1000 °C où les particules se sont regroupées sous forme de gouttelettes. Ce comportement ne reflète pas une fusion, car le TiO_2 fond à 1843 °C (Kurt J. Lesker Company GmbH, 2020), et est cohérent avec la littérature qui montre que les particules d'anatase augmentent en taille avant de se transformer en rutile (Bachina et al., 2021).

Pour confirmer cette transformation, l'espacement d des particules a été mesuré à fort grossissement et a révélé un espacement de réseau de 3,55 Å (Figure 5.2), correspondant à l'anatase. Cela indique que même après un chauffage à 1000 °C, la transformation complète n'a pas eu lieu. Étant donné les limites des mesures sur une seule particule, l'analyse du schéma de diffraction a été utilisée pour obtenir une vision plus large du comportement de l'échantillon, comme le montre la Figure 5.3.

Le schéma de diffraction, enregistré au même endroit que la Figure 5.1, montre un fort signal d'anatase (a) avec quelques taches de rutile, en accord avec les spécifications d'Evonik de 85% d'anatase et 15% de rutile. Après 3 h à 800 °C (b), 900 °C (c) et 1000 °C (d), une légère augmentation de l'intensité de l'anneau de rutile a été observée. CrysTBox a été utilisé pour quantifier les changements d'intensité de chaque anneau (Figure 5.4). L'intensité initiale de l'anneau rutile était de 0,357 et est passée à 0,532 après 1000 °C. Bien que cela suggère une certaine transformation, l'augmentation globale de l'intensité peut indiquer une augmentation du bruit de fond plutôt qu'un changement de phase clair.

Malgré un chauffage de 9 h à des températures supérieures à 800 °C, les résultats n'étaient pas cohérents avec les affirmations de la littérature concernant une transformation complète après 3 h à 800 °C (Evonik, 2017). Des résultats similaires ont été obtenus lors d'expériences supplémentaires, dont une réalisée en dehors du TEM pour évaluer les effets de la pression et de l'oxygène. La seule référence bibliographique présentant des résultats comparables concernait des particules de dioxyde de titane plus grosses (100 nm), qui ont été entièrement transformées après 8 h à 1000 °C (Gouma and Mills, 2001). La transformation incomplète et le respect des limites de température pourraient être dus à des erreurs dans la sélection des échantillons, la préparation, l'étalonnage du système ou la fonctionnalité du porte-échantillon. Une analyse complète des erreurs est nécessaire pour en savoir plus.

5.3 Analyse des erreurs du système

Les résultats des mesures contredisent 70 années de recherche sur le comportement du titane, ce qui suggère une défaillance probable du système expérimental. Pour analyser la défaillance du système, la première étape consiste à vérifier que le système de chauffage atteint la température prévue pour l'échantillon. Cela peut être testé efficacement en utilisant un échantillon dont le point de fusion et la structure cristalline sont connus. Le point de fusion indique une rupture de la structure cristalline, qui peut être observée en mode diffraction comme la disparition des anneaux de diffraction (Borchardt-Ott and Sowa, 2018).

L'aluminium (Al), dont le point de fusion est de 660.3 °C (Czanderna et al., 1958), a été sélectionné pour être testé dans la plage de chauffage des Protochips. L'échantillon d'aluminium a été pulvérisé à l'arrière de la puce électronique afin d'éviter de court-circuiter le circuit électrique situé à l'avant. L'aluminium pulvérisé, visible sous la forme d'une ombre grise/argentée, est illustré à la Figure 5.5 avec une épaisseur de 30 nm ±5 nm.

Pendant l'expérience de chauffage, l'échantillon d'aluminium a été monté dans le support Aduro et le fichier d'étalonnage correct pour la puce électronique (numéro de série FS40486-5) a été chargé. La température a été réglée manuellement et augmentée progressivement tandis que l'échantillon était observé en mode diffraction. Les figures de diffraction obtenues à température ambiante (a), à 660 °C (b) et à 1000 °C (c) sont illustrées à la Figure 5.6. L'absence de changement dans le diagramme de diffraction indique que l'échantillon n'a pas fondu, ce qui suggère que la limite de température du porte-échantillon a été atteinte. La durée de 30 minutes de l'expérience exclut un temps de chauffage insuffisant, et l'épaisseur de 30 nm de l'échantillon devrait permettre des changements immédiats à la température de fusion. Bien que la hauteur de l'échantillon ait changé en raison des ajustements de la mise au point, ce qui indique un changement de température (Protochips, n.d.(a)), elle n'était pas assez élevée pour faire fondre l'aluminium, peut-être en raison d'erreurs d'étalonnage.

Pour tester plus avant cette hypothèse, le zinc (Zn), qui fond à 419.5 °C (Czanderna et al., 1958), a été choisi. Des nanoparticules de zinc (SkySpring Nanomaterials Inc. #9921XH) ont été déposées sur la face avant de la puce électronique sans dilution afin d'éviter la formation de ZnO, dont le point de fusion est beaucoup plus élevé (1975 °C) (International Labor Organization, 2017). Bien que cette préparation ait produit des agrégats plus importants, comme le montre la Figure 5.7, la configuration expérimentale a reflété celle de l'échantillon d'aluminium.

L'échantillon de Zn a été chauffé et les diagrammes de diffraction avant (a), pendant (b) et après (c) le chauffage sont présentés dans la Figure 5.8. Un léger changement dans le diagramme de diffraction a été observé à 1000 °C, les anneaux extérieurs s'estompant, ce qui indique une approche possible de la température de fusion. Cependant, les anneaux sont restés visibles, confirmant que l'échantillon n'a pas fondu pendant les 30 minutes.

En conclusion, le système Protochips ne semble pas pouvoir atteindre les températures spécifiées. Bien que le changement de hauteur z observé suggère un certain chauffage, il est probablement dû à des erreurs de calibrage lors de l'installation initiale par un technicien de Protochips il y a un an. La transformation minimale de l'anatase en rutile renforce l'hypothèse selon laquelle une certaine chaleur a atteint l'échantillon, mais pas la température prévue.

Étant donné la transformation incomplète du titane et le fait que les points de fusion de l'aluminium et du zinc n'ont pas été atteints, on estime que la température maximale atteinte est inférieure à 420 °C, probablement autour de 400 °C - la température la plus basse rapportée pour la transformation de l'anatase en rutile. En raison de contraintes de temps, il n'a pas été possible d'approfondir l'étude ; la prochaine étape consistera en un recalibrage du système par Protochips, suivi d'une étude de la température de transformation du titane d'Evonik.

5.4 Résumé

Le but de l'étude est d'observer la transformation de l'anatase en rutile dans l'AEROXIDE® TiO_2 P25 d'Evonik, caractérisé par une taille moyenne de particules de 24 nm. La poudre est diluée dans 3 ml de solution d'acétone et soumise à un bain sonique pendant 60 minutes pour assurer une bonne dispersion. Le titane devrait se transformer complètement d'anatase en rutile après 3 h à 800 °C.

Des expériences de chauffage in situ ont été réalisées à l'aide du porte-échantillon Aduro de Protochips à des températures de 800 °C, 900 °C et 1000 °C pendant une durée totale de 3 h. Au cours de ces expériences, seuls des changements minimes dans la taille et la forme des particules ont été observés en mode image. Cependant, l'intensité du premier anneau de diffraction du rutile a augmenté au fil du temps, indiquant une légère transformation de l'anatase en rutile. Notamment, l'étendue de la transformation observée n'était qu'une fraction du nombre total de particules, ce qui soulève des inquiétudes quant à la procédure expérimentale. Même après avoir chauffé l'échantillon pendant 9 h à des températures supérieures à 800 °C, la transformation limitée suggère des problèmes potentiels avec le système de chauffage.

Pour vérifier cette hypothèse, des expériences supplémentaires ont été réalisées avec des nanoparticules de zinc et de l'aluminium pulvérisé en raison de leur faible point de fusion. La fusion de ces échantillons entraîne une modification de la structure cristalline, observable en mode diffraction par la disparition des anneaux de diffraction. Cependant, le système Protochips n'a pas réussi à atteindre les points de fusion des deux échantillons (Al = 660.3 °C et Zn = 419.5 °C). Ce résultat indique une erreur d'étalonnage dans le système, suggérant que la température affichée ne reflète pas exactement la température atteinte.

La variation de la hauteur Z pendant le chauffage, due à l'expansion thermique de la membrane et de l'échantillon, indique qu'une certaine chaleur est générée. Sur la base de la transformation limitée de l'anatase en rutile et de l'impossibilité d'atteindre le point de fusion du zinc, on estime que la température maximale atteinte au cours des expériences était d'environ 400 °C. Cette estimation est cohérente avec les températures les plus basses rapportées par les chercheurs. Elle est également cohérente avec la température de transformation la plus basse rapportée pour l'anatase.

Pour résoudre ces problèmes, le système de chauffage devra être soigneusement vérifié et recalibré par Protochips afin de s'assurer que la température affichée corresponde à la température réellement atteinte. Une fois le système validé, l'étude de la température de transformation de la poudre Evonik TiO_2 pourra reprendre.

6 Conclusion

L'objectif principal de cette étude était de mettre en service un système de caméra VS externe et d'étudier la transformation de l'anatase en rutile à l'aide d'un système d'électrons de transmission in situ. L'étude a porté sur les performances de la caméra et l'évaluation de la transformation de phase dans le TiO_2, en tenant compte des erreurs potentielles du système de chauffage.

La caméra VS externe, montée sur un trépied personnalisé, a servi d'alternative efficace à la caméra TEM interne post-GIF. Elle offrait un champ de vision 23 fois plus grand, ce qui augmentait la fiabilité des expériences à long terme, tout en étant plus facile à utiliser et moins susceptible d'être endommagée. Cependant, la caméra GIF présentait des erreurs de mesure plus faibles en modes diffraction (0,6%) et image (-2,6%), ce qui la rendait plus précise pour une analyse détaillée, bien que le système externe réponde aux exigences générales de précision pour les applications TEM (moins de 5%).

Pour les expériences de chauffage in situ, l'AEROXIDE® TiO_2 P25 d'Evonik (taille moyenne des particules: 24 nm) a été soumis à des traitements thermiques à 800 °C, 900 °C et 1000 °C pendant 9 h. La transformation attendue de l'anatase en rutile, qui se produit généralement après 3 h à 800 °C (Evonik, 2017), n'a pas eu lieu. Seuls des changements mineurs dans la taille et la forme des particules ont été observés, ainsi qu'une légère augmentation de l'intensité du rutile dans le mode de diffraction, indiquant une transformation incomplète.

Des essais avec des nanoparticules d'aluminium et de zinc pulvérisées, dont les points de fusion connus sont respectivement de 419.5 °C et 660.3 °C (Czanderna et al., 1958), ont montré que le système de chauffage de Protochips n'atteignait pas les points de fusion, ce qui suggère une erreur d'étalonnage. Pour résoudre ce problème, le système de chauffage devra être recalibré par Protochips afin de s'assurer que les températures affichées reflètent bien les températures réelles pendant les expériences. Une fois recalibré, le système de chauffage permettra de déterminer avec plus de précision la température de transformation de la poudre de titane d'Evonik. Une fois ce problème d'étalonnage résolu, les études ultérieures permettront de mieux comprendre le comportement de transformation de phase du TiO_2 à haute température.

En outre, l'étude de l'influence de différentes atmosphères et tailles de particules sur la température de transformation peut fournir des informations plus approfondies sur le comportement thermodynamique du TiO_2. L'intégration d'outils analytiques avancés, tels que la surveillance en temps réel et les techniques combinées de chauffage et de manipulation électrique, pourrait améliorer la compréhension de la stabilité des phases et de la cinétique de transformation dans les matériaux nanocristallins. Cela permettrait d'optimiser l'utilisation du TiO_2 dans des applications allant de la photocatalyse au stockage de l'énergie.

Table of Contents

List of Figures

List of Tables

List of Acronyms

Al	Aluminum.
DSLR	Digital Single-Lens Reflex.
GIF	Gatan Imaging Filter.
TEM	Transmission Electron Microscope.
VS	Viewing Screen.
Zn	Zinc.

1 Introduction

Titanium dioxide (TiO_2), also known as Titania, is a widely used material due to its versatile properties and applications. Its nanocrystalline form is used in various fields such as photocatalysis, solar cells, energy storage and as a pigment (Lee and Zuo, 2004). Among the different phases of TiO_2, anatase and rutile are the most prominent. Rutile is the thermodynamically stable phase, while anatase is metastable and can transform to rutile upon heating (Hanaor and Sorrell, 2011). This phase transformation is of particular interest because it significantly affects the optical and electronic properties of the material, which are critical for its effectiveness in applications such as photocatalysis and photovoltaics (Koparde and Cummings, 2008).

The study of phase transformations in TiO_2 is essential for understanding how temperature, particle size and environmental conditions affect structural changes in the material (Hanaor and Sorrell, 2011). One of the most effective ways to observe these transformations is with a Transmission Electron Microscope (TEM). This technique allows real-time observation of structural changes at the atomic scale and provides insight into the anatase to rutile transformation.

The focus of this thesis is twofold: first, to develop and calibrate an external Viewing Screen (VS) camera system to extend the imaging capabilities of the TEM for analysis, and second, to study the anatase-rutile phase transformation in Titania under controlled heating conditions. The external VS camera system was implemented as an alternative to the more delicate internal TEM camera, providing a larger field of view and improved durability against potential electron beam damage. This new system was tested and compared to the established internal camera in terms of magnification levels, contrast, field of view and measurement accuracy.

The second aspect of this study involves the use of Protochips heating system to apply controlled heat to TiO_2 samples during in situ TEM experiments. Using AEROXIDE® TiO_2 P25, a commercial form of Titania from Evonik with an average particle size of 24 nm, the goal was to observe the complete transformation from anatase to rutile at elevated temperatures. This transformation begins at temperatures above 400 °C and accelerates rapidly with increasing temperature, with anatase gradually converting to rutile over time (Czanderna et al., 1958). By heating the sample in the TEM, it was possible to observe small structural changes in both image and diffraction modes.

However, during these experiments it became apparent that the Protochips heating system was not reaching the expected temperatures, as indicated by the inability to melt zinc nanoparticles and sputtered aluminum, which have known melting points at 419.5 °C and 660.3 °C respectively (American Elements, 2024). This discovery pointed to a calibration error in the heating system that resulted in inaccurate temperature readings. As a result, the phase transformation from anatase to rutile was only partially achieved and further recalibration of the system was deemed necessary.

2 Basic Principles of Transmission Electron Microscopy

To study Titania nanoparticles, a microscope with very high resolution is required. The type of microscope with the highest resolution is an electron microscope, specifically a Transmission Electron Microscope (TEM) This chapter gives a general overview of the functionality of the TEM and highlights the functions that are essential for the in situ study of the phase transformation of Titania.

2.1 Microscope

The TEM is commonly used to image, measure and manipulate matter at the micro- and nanoscale. It creates images by capturing the signals from the interaction of the electron beam with the sample in a high vacuum (Beun, 1994). The TEM used is a modified version of the JEOL JEM-2100Plus, which is also capable of time resolved measurements. For a better understanding of how a fundamental TEM works, a schematic overview is shown in Figure 2.1.

Figure removed due to copyrights issues

Figure 2.1: Schematic overview of a TEM (modified from Luo, 2016)

Cross section of a TEM. The electron beam is generated at the top by the electron gun (a) and passed through the column via several lenses (b-d). The electron beam transmits the specimen (e) on the specimen holder and an image is projected onto the phosphor screen (f) or camera (g) for image capture (Luo, 2016).

This sectional view in shows all the components that are important for understanding the design and operation of the microscope (Luo, 2016). At the top of the TEM is the electron gun (a), which in the JEOL TEM is a LaB6 filament. The LaB6 filament produces an electron beam when heated with an acceleration voltage of 200 kV. The electron beam is directed through the column by different types of lenses, namely the condenser lenses (b), the objective lens (c) and the projector lens (d). These are electromagnetic lenses that guide the path of the electrons and are located before and after the specimen (e). The electrons must pass through the specimen and reach the end of the column where an image is projected. The image can be displayed on the phosphor screen (f), called the Viewing Screen (VS), and on a camera (g) located below the VS. The projected image visualizes the interaction of the electrons with the sample. The VS emits green light when hit by electrons. The brightness of the emitted light corresponds to the number of electrons hitting the screen. The VS is motorized from the control panel and, when raised, reveals the integrated camera. The VS also serves as a protection for the camera, as it is very sensitive and can be easily damaged by the high-energy electron beam due to its high intensity. The camera used in the TEM for this thesis is the Gatan Ultrascan. The camera is connected to a computer to capture images directly. When using the camera, the Gatan Imaging Filter (GIF) mode is used. In this mode, the electron beam is directed to help guide the electrons from the beam to the camera's sensor through a column located below the VS (not shown in Figure 2.1). Non-GIF mode is used to project an image onto the VS.

Electrons also have the advantage of interacting with the sample and producing a variety of secondary signals. These signals can be used in analytical electron microscopy to obtain information about the chemical and structural properties of the sample (Williams and Carter, 2008). An overview of the spectra of the signals produced by a high-energy beam is shown in Figure 2.2. For our purposes, the most important signals come from the direct beam and the elastic scattering of electrons generated by transmitted electrons. The direct beam is used to image the sample and the elastic scattered electrons are important for the diffraction pattern.

Figure removed due to copyrights issues

Figure 2.2: Signals generated by a high-energy beam (from Williams and Carter, 2008)

Signals generated by the interaction of the high-energy electron beam with a thin sample, which can be used for analysis. Important for the imaging and diffraction modes are the direct beam and the elastically scattered electrons (Williams and Carter, 2008).

Finally, it is important for the functionality of the microscope to clarify the boundary conditions for a sample. The sample area that can be examined with a TEM is generally in the range of µm^2 to nm^2. The sample must be thin enough to allow electrons to pass through and to withstand the high vacuum. The sample must be deposited on a TEM grid. There are different types of grids for many different applications and also different types of holders that can move, tilt and manipulate the sample in situ. The grids vary in spacing, material, shape and functionality (Pella, n.d.).

2.2 Imaging

The method of imaging with a TEM is similar to the principle of a transmitted light microscope. The light microscope sends light through a (semi-)transparent specimen and projects it onto a screen (Murphy, 2012). The features on the projected image depend on the thickness and transparency of the material. The TEM works in a similar way, but instead of light, electrons transmit the sample to project an image. The brightness depends on the intensity of the electron beam and the contrast depends on the phase contrast of the electron scattering (Lee and Zuo, 2011). This chapter focuses on the GIF mode as the non-GIF mode will be discussed later in the commissioning of the external VS camera.

In image mode, it is possible to display a wide range of scales (JEOL, n.d.). At the lowest magnifications, from x150 to x1500, this TEM can display features on the micrometer scale and is used to obtain an overview of a relatively large area on the sample. The medium magnification range, from x2000 to x10k, allows for examining changes in particle shape while still providing a broader view of the sample. Higher magnifications, from x12k to x30k, reveal nanoscale features, and at the highest magnifications, from x40k to x120k, it becomes possible to distinguish individual atomic layers. This is particularly useful in crystal characterization, where atomic spacing can be measured, and materials and phases can be identified. This capability is especially valuable for studying phase transformations, such as the anatase to rutile transition, in single particles. An overview of the different scales is shown in Figure 2.3.

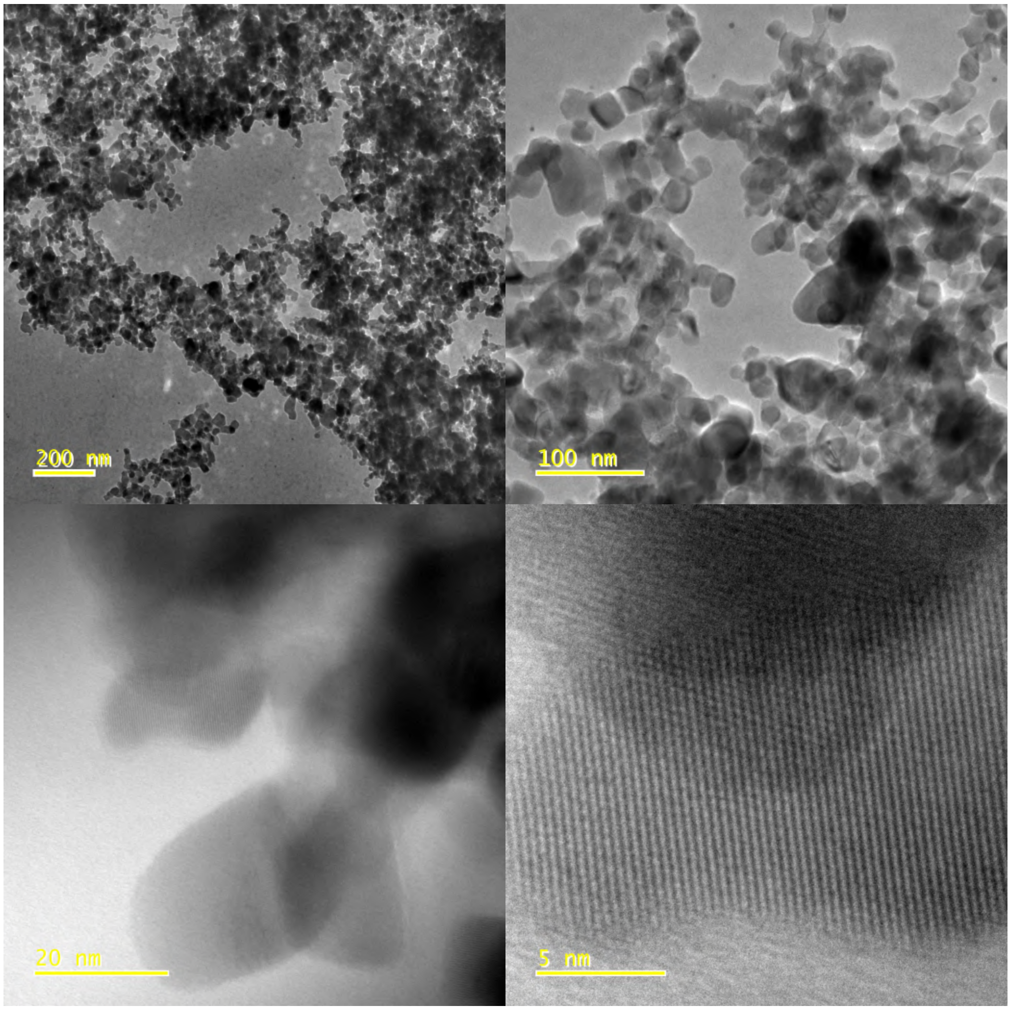

Figure 2.3: Image mode at different magnification levels

Overview of Titania nanoparticles at different magnifications. The magnification level is low (top left) at x1000, medium (top right) at x4000, high (bottom left) at x30k and highest (bottom right) at x120k. This illustrates the progression in magnification from an overview of clusters (top left) to the visualization of the distance between the lattice planes (botom right). All images were taken with the post-GIF camera.

2.3 Diffraction

A TEM specific feature is the ability to generate diffraction patterns. This makes it possible to provide information about the crystal structure of a sample, especially its crystalline nature (Borchardt-Ott and Sowa, 2018). The crystal lattice acts as a diffraction grating. The electron beam passing through the grating creates an interference pattern as it exits the grating. The interference is material and phase specific and produces an image of rings and spots (Fultz and

Howe, 2013). Spots are produced by materials that contain long-range order in the lattice. This can also come from single grains as they have a uniform lattice orientation. Rings are produced by a collection of a large number of crystals with different orientations. Each grain produces its lattice specific diffraction spots and the collection of grains results in diffraction rings. The radius of the rings as well as their intensity is material and phase specific. The generated diffraction radius depends on the diffraction angle and the camera length as shown in Figure 2.4.

Figure removed due to copyrights issues

Figure 2.4: Reduced effective camera length using lenses (from Williams and Carter, 2008)

In a TEM, lenses can modify the electron path without changing its diffraction angle (2θ), allowing adjustments to the camera length L without altering the true electron path length. (Williams and Carter, 2008)

The electron beam passes through the sample and is diffracted. The angle of diffraction ($2\,\theta$) is material and phase specific and can be calculated using the Bragg condition. In general, it describes the specific condition under which constructive interference occurs when waves are scattered by the atomic planes in a crystalline material (Borchardt-Ott and Sowa, 2018). These constructive interferences result in spots and rings in the diffraction pattern. The diffraction angle θ can be derived from the Bragg condition with:

$$\lambda = 2 * d * sin(\theta) \tag{1}$$

The incident wavelength (λ) of an electron in the TEM at 200 kV is $\lambda_{\mathrm{TEM}} = 2.508\,\mathrm{pm}$. The distance between the lattice planes is d and affects the resulting scattering angle. In Figure 2.4 the radius R depends on the camera length L and is given in ”cm”. Since only a small part of the high-energy electron beam is diffracted, it is necessary to protect the post-GIF camera from the direct beam with a beam blocker.

In the diffraction mode it is also important to introduce the Selected Area Aperture. It is located between the sample and the projected image and is used to limit the area of the electron beam hitting the sample. This makes it possible to focus the electron beam on an even smaller area of the sample. The diffraction mode is particularly interesting for this study because it effectively distinguishes between the different phases of Titania. Titania has different lattice parameters for the anatase and rutile phases. Therefore, it is possible to study the change in the diffraction pattern as a means of studying the phase transformation in situ.

In the diffraction mode it is also important to introduce the apertures in a TEM. The most important one for this work is located between the sample and the projected image. This is the Selected Area Aperture and works in image mode. It is used to limit the area of the electron beam hitting the sample. This makes it possible to focus the electron beam on an even smaller area of the sample. The diffraction mode is particularly interesting for this study because it effectively distinguishes between the different phases of Titania, as it has different lattice parameters for the anatase and rutile phases. Therefore, it is possible to study the change in the diffraction pattern as a means of studying the phase transformation in situ.

3 Commissioning the External Viewing Screen Camera

A TEM generally has two ways to project an image, the VS and an integrated camera. The integrated camera is already an established method for measurements at the laboratory in both image mode and diffraction mode. To capture images from the VS, an external camera must be set up. The goal of this chapter is to integrate an external camera, quantify its properties and find out its advantages and disadvantages compared to the integrated post-GIF TEM camera.

3.1 Calibration of the External Camera

The external VS camera should not only be an alternative way to make measurements, but also add other applications that are not feasible with the integrated camera. The GIF camera is very delicate and prone to damage, so the new camera should also be a way to continue using the TEM even if the GIF camera is damaged. This chapter covers the setup of the external VS camera, the process from image capture to analysis and the calibration of the scale bar for each magnification and camera length in non-GIF mode.

3.1.1 Setup of the new Camera System

A Digital Single-Lens Reflex (DSLR) camera was chosen to capture images of the VS because of its adaptability and high resolution (Nikon, 2008). The DSLR used is the Nikon D60 with a Nikon "AF-P DX NIKKOR 18-55mm f/3.5-5.6G VR" lens. Depending on the ambient brightness in the lab and the light emitted from the VS, the camera settings can be adjusted, mainly the ISO sensitivity, aperture and exposure time (Peterson, 2010).

Before setting up the camera, the mount must be configured. The camera must be securely positioned in front of the VS and high enough to capture the entire area of the VS. The space on the table in front of the VS is very limited, so no commercially available tripod fits. The stand was custom-built using optomechanical parts from Thorlabs. The finished stand with the DSLR mounted in front of the VS can be seen in Figure 3.1.

Figure 3.1: Mounted DSLR in front of the viewing screen

The camera on the tripod must be placed in front of the VS so that the center of the camera's focus point aligns with the center of the VS. The focal length is set to 35 mm to ensure the camera captures the entire VS.

ISO sensitivity refers to the sensitivity of the image sensor to light and is a digital gain setting (Peterson, 2010). For the Nikon D60, it ranges from 100 to 1600 (Nikon, 2008). A low value is less sensitive to light, but has the advantage of less noise in the image. A higher value increases the brightness of the image, but also increases the noise.

The lens aperture controls the amount of light that passes through the lens to the image sensor and affects the depth of field (Peterson, 2010). The aperture is indicated by the "f-number", which is the ratio of the focal length to the diameter of the aperture. A lower f-number results in a more open aperture and therefore a brighter image, but less depth of field. The aperture can be set between f/3.5 and f/38 (Nikon, 2007).

The exposure time is controlled by the shutter speed and regulates the time the image sensor is exposed to light. A DSLR has a shutter that blocks incoming light in its default (resting) position. Depending on the selected exposure time, the DSLR lifts the shutter and lets light hit the sensor (Peterson, 2010). For the Nikon D60, the exposure time can be set from 1/4000 s to 30 s (Nikon, 2008). A shorter exposure time results in a darker image, but is less susceptible to motion blur.

Since the position and area of interest remains fixed, the aperture and ISO sensitivity settings can be kept constant after setup. Only the exposure time must be adjusted due to the varying brightness in the laboratory and the brightness of the light emitted by the VS. The image and diffraction modes of the TEM also affect the brightness of the image because each mode has different light intensities and illuminated areas.

The first setting to find the optimum value for is the aperture. The optimal aperture is small enough so that the depth of field extends over the entire area of the VS. At the same time, it is large enough to let in enough light for a reasonable exposure time to produce a high-quality image. With a fixed focal length of 35mm, the aperture has been tested from f/5 to f/32, as shown in Figure 3.2.

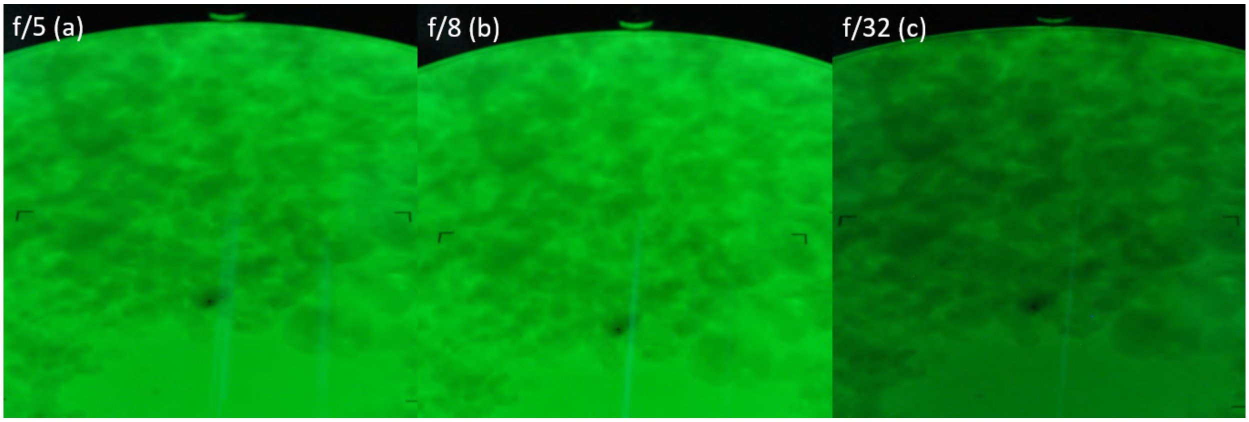

Figure 3.2: Effect of aperture on image quality

Comparison of different aperture settings and their effect on image quality. Largest aperture (f/5, a) on the left, smallest aperture (f/32, c) on the right and optimum setting (f/8, b) in the center. Clear difference in depth of field at large aperture (a) and brightness at small aperture (c).

The effect of aperture on depth of field and brightness is shown at three different settings. On the left is an example of the widest aperture. Here, the depth of field is too small to cover the entire screen. On the right in Figure 3.2 is the smallest aperture. It allows too little light to pass through, making it impossible to capture a high-quality image, even with other settings adjusted to increase brightness. The optimum is shown in the middle of Figure 3.2 with an aperture of f/8. Here, the depth of field covers the entire area of the VS and it is still bright enough with a shorter exposure time of 5 s compared to 30 s with the smaller aperture. The next setting to examine is the ISO sensitivity. The optimal sensitivity increases the brightness of the image without increasing the noise, which reduces the quality of the image. The ISO sensitivity was tested from 100 to 1600 and the results are shown in Figure 3.3.

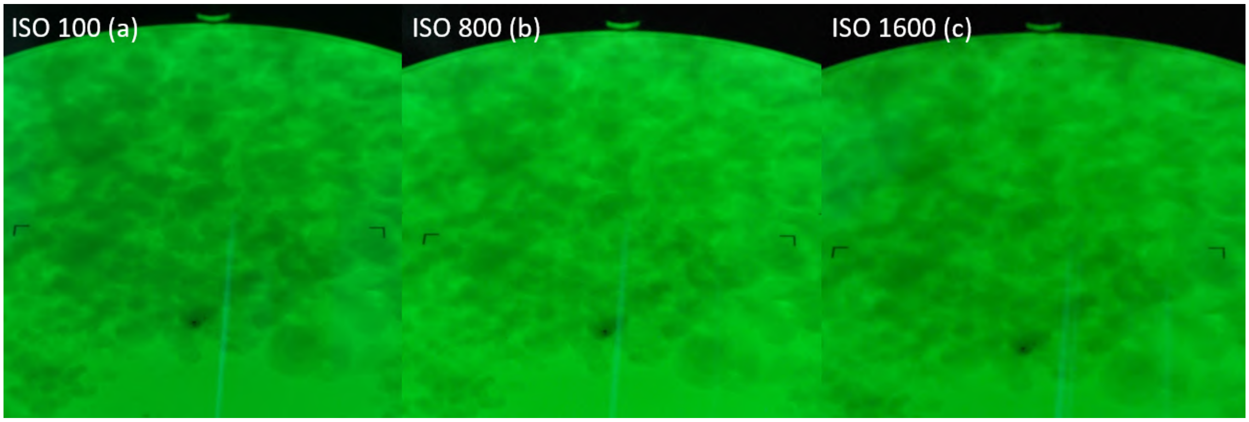

Figure 3.3: Effect of ISO sensitivity on image quality

Comparison of different ISO sensitivity settings and their effect on image quality. Lowest setting (100,a) on the left, highest (1600, c) on the right and optimum (800, b) in the middle. There is no visual difference between a ISO sensitivity of 100 and 800, but there is a big difference in exposure time (30s with 100, 5s with 800). The highest value has increased noise, which significantly reduces image quality (c).

The effect of ISO sensitivity on brightness and noise is shown in three different settings. Only the exposure time is adjusted to keep the brightness constant. At the lowest sensitivity on the left in Figure 3.3, the image has the least noise, but the exposure time is at a maximum of 30 s. The highest sensitivity on the right in this figure reduces the exposure time to 2.5 s, but the noise is significantly higher and distorts the features of the sample. The optimum between noise and quality is at 800 and can be seen in the middle of Figure 3.3. The noise is slightly higher than ISO 100, but the exposure time is reduced to 5 s. This gives much more flexibility in adjusting the camera to different lighting conditions.

The exposure time cannot be set to a specific value due to several factors. The brightness in the laboratory and on the VS varies. The image mode and diffraction mode of the TEM differ in the intensity of emitted light and the size of the illuminated area. The brightness also affects the contrast of the sample and can be changed depending on the analysis. A good estimate for the exposure time is around 2.5 s in image mode and 10 s in diffraction mode.

After setting up the tripod for the DSLR and adjusting the settings for the imaging process to the optimum, it is now possible to take high quality images. The optimum aperture is f/8. The optimum ISO sensitivity is 800. The exposure time depends on the mode and type of analysis to be performed on the image. The images are then saved in JPEG format with a resolution of 3872 x 2592 pixels.

3.1.2 Perspective Correction Process

The images are taken at a 45° angle, causing a distorted perspective. To reduce measurement errors, the perspective must be corrected using ”DxO Viewpoint”, which provides a quick and easy solution. Its interface can be seen in Figure 3.4.

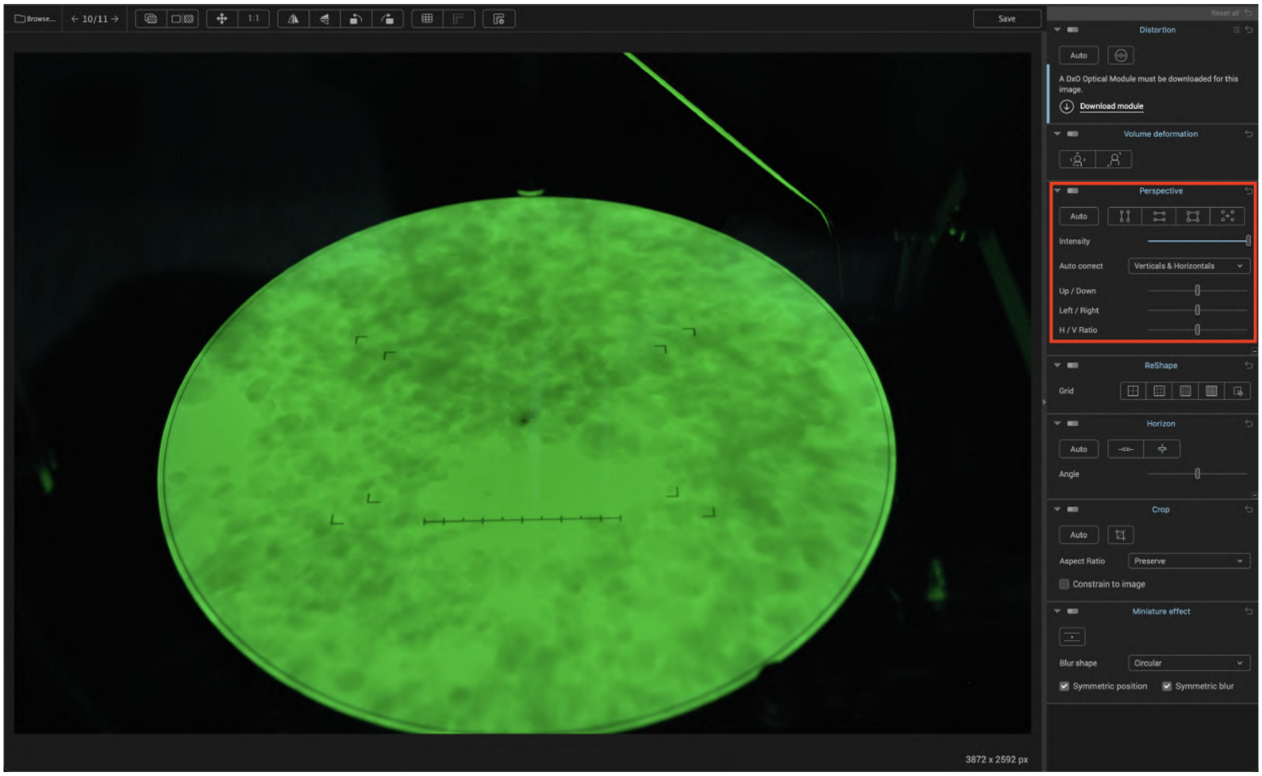

A DxO Optical Module must be downloaded for this image.

Auto correct: Verticals & Horizontals

Aspect Ratio: Preserve

☐ Constrain to image

Blur shape: Circular

☑ Symmetric position ☑ Symmetric blur

Figure 3.4: Interface of DxO Viewpoint

DxO Viewpoint interface with an unedited image taken with the DSLR. The perspective correction tools are on the right, with the main functions (”Rectangle” and ”H/V Ratio”) in the highlighted area in red under ”Perspective”. (Labs, 2024)

On the left is an example of an image taken with the DSLR. On the right, the perspective correction settings are highlighted in red. In this section, the ”Rectangle” option is used for the correction. It uses a rectangular shape as a reference that can be placed over the corners of the VS. It automatically adjusts the image to the correct perspective. It is possible to fine-tune the corrected perspective with the ”H/V Ratio” option. An example of how to perform perspective correction is shown in Figure 3.5

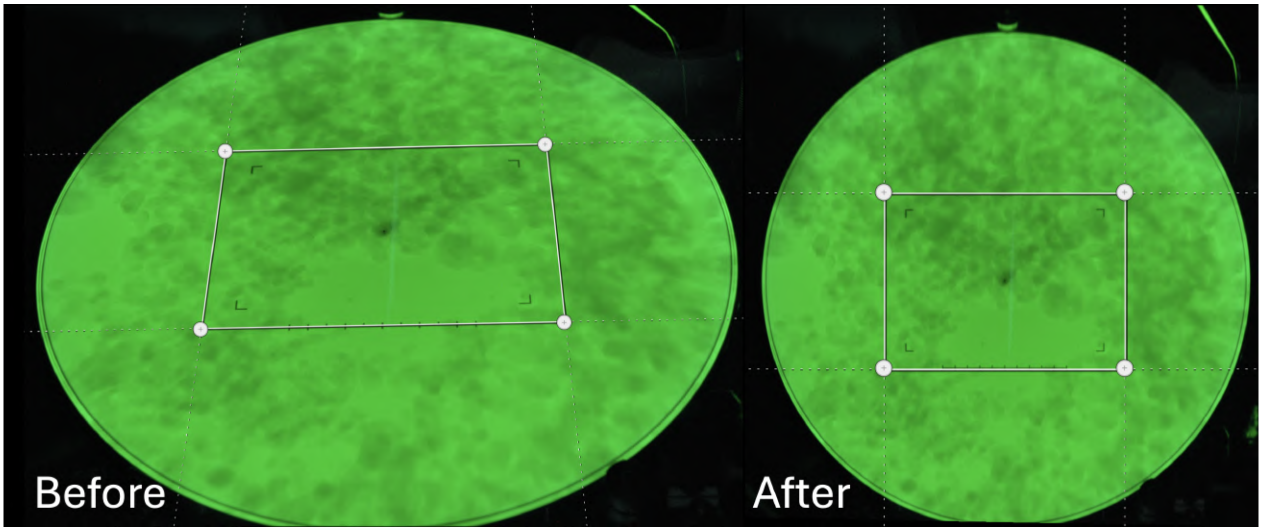

Figure 3.5: Before and after perspective correction

Images before (left) and after (right) perspective correction. The "Rectangle" function is selected and the change due to perspective correction is visualized by the white rectangle. The ratio of length to height has been adjusted with "H/V Ratio".

On the left is the image taken with the DSLR and on the right is the image after perspective correction. The white rectangle is generated and aligned with the outer corners of the VS. In the after image, the image is automatically manipulated by the software so that the angle inside the rectangle is 90°. The result of the perspective correction can be verified by examining the ratio of the length to the height of the rectangle on the VS. The length on the VS is 78 mm and the height is 56 mm, giving a ratio of 1.39. This ratio can be controlled by pixel measurements of the corrected image. Deviations can be corrected with the H/V ratio setting. Typically, for each point changed in the H/V ratio, the ratio of the rectangle on the manipulated image changes by 0.01.

3.1.3 Calibration

After defining the DSLR settings and ensuring the image is suitable for measurements, the VS scale bar can be calibrated for each magnification in image mode and for each camera length in diffraction mode, enabling accurate measurements. Calibrating the microscope requires a standardized part with known dimensions (DIN e.V., 1995), such as a special grating with a fixed pitch. For diffraction mode calibration, the part must be a pure material. A standard pure gold grating with 2160 lines per mm and a pitch of 463 nm meets these criteria (Pella, n.d.).

During calibration, all components and settings must remain consistent, except for the magnification and camera length of the TEM. This includes the previously fixed position and settings for the DSLR as well as the controlled perspective correction. Only the exposure time was adjusted due to the different TEM modes and the different light intensity of the VS to ensure equally bright images. All pixel measurements were done using "ImageJ," and examples of calibrations in both image mode and diffraction mode are shown in Figure 3.6.

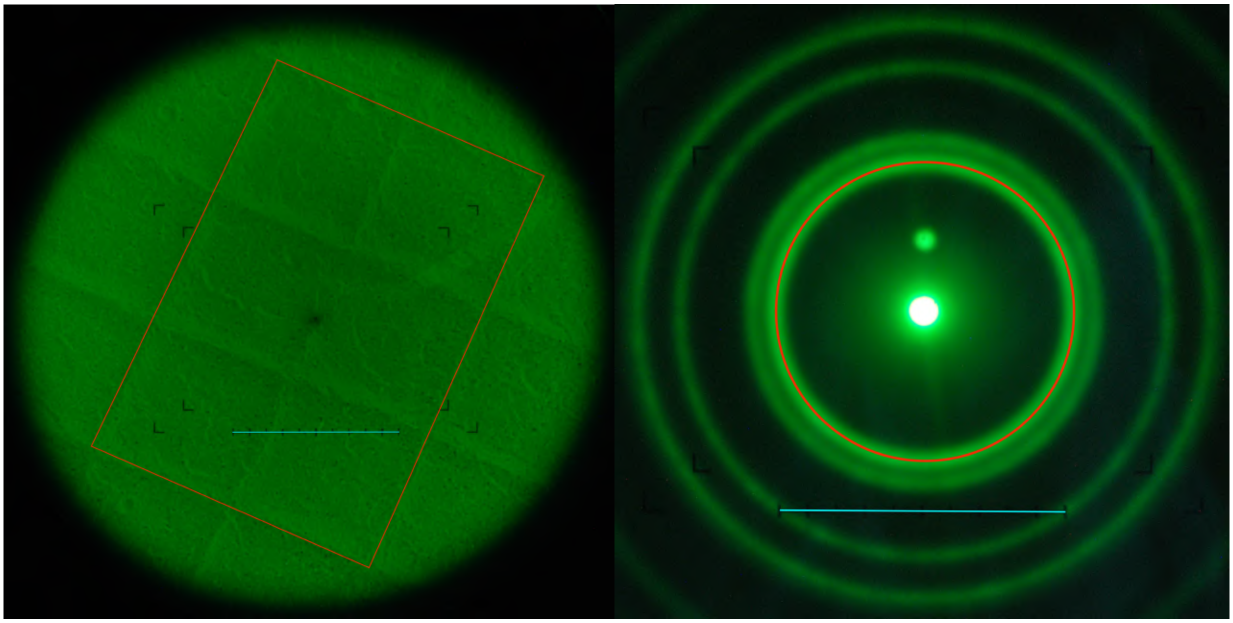

Figure 3.6: Calibration of the viewing screen in image mode and diffraction mode

Examples of calibration of the external VS camera. Measurement of the lattice spacing of gold (left) at x100k magnification over several edges in red. Measurement of the diffraction pattern (right) at a camera length of 250cm. The whole ring marked in red was used to obtain the radius for calibration. Measurement of the scale bar (blue) in both modes.

On the left is an example of the gold standard at x100k magnification in image mode and on the right is the same sample in diffraction mode at a camera length of 250cm. The red and blue lines visualize the measurements made in ImageJ. The red line corresponds to the measured part of the sample and the blue line corresponds to the scale bar.

Calibration in diffraction mode is done with the first diffraction ring of gold. At room temperature it has a face-centered cubic crystal structure with a lattice constant for a, b and c = 4.078 Å (Wyckoff, 1963). The d-space in plane [1 1 1] for gold is at $d1 = a/\sqrt{3}$, which gives $d1_G = 2.356\,\text{Å}$. Converting to reciprocal space with $k = 1/d1$ results in $k_G = 4.245\,1/\text{nm}$ for gold. This is used as the standardized length for calibrating the camera length in diffraction mode. To minimize the error of this pixel measurement, the whole area of the first diffraction ring is measured in pixels, as shown in Figure 3.6. The radius in pixels can be calculated with $r = \sqrt{\frac{Area}{\pi}}$. With the radius of the first ring both in 1/nm and pixels, and the length of the scale bar in pixels, the total length of the scale bar in 1/nm can be calculated with

$$Scalebar[1/nm] = k[1/nm] * Scalebar[Pixel]/Radius[Pixel] \tag{2}$$

for each camera length. The camera length in non-GIF mode ranges from 20cm to 250cm and only affects the radius of the diffraction ring in pixels. This results in the calibrated length of the scale bar in 1/nm.

The calibration of the scale bar in image mode is divided into two parts. The first part includes the magnifications where the distance between two lines is visible, ranging from x15k to x250k. In the second part, with higher magnifications from x300k to x1.2M, distinctive points of the sample were used (e.g. defects) to calibrate the scale bar.

Measurements of the distance between two lines were made using a line measurement from ImageJ. For magnifications with multiple visible squares, the circumference was measured instead of a single distance. Measuring over a larger distance reduces the measurement error, similar to the calibration in diffraction mode. An example of the measurement is shown in Figure 3.6 on the left, highlighted in red. For higher magnifications, the actual distance in nm was calculated between two defects or distinctive points on the standard visible at two successive magnifications. An example of the high magnification calibration is shown in Figure 3.7

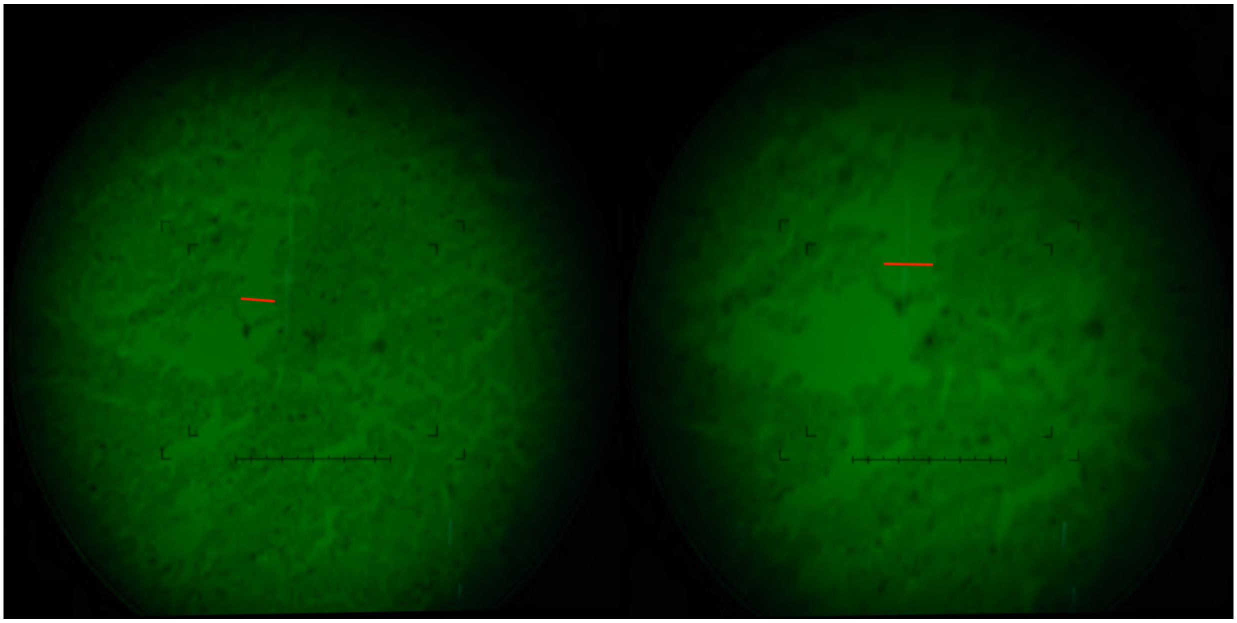

Figure 3.7: Calibration at higher magnifications with defects

Using landmarks and defects as orientation points to calibrate the scale bar at higher magnifications (x400k left and x500k right). The measurement line (red) covers the same distance at both magnifications.

On the left is a sample at x400k magnification and on the right at x500k. The chain-like structure connecting the two larger areas was used as an orientation point. With an already calibrated scale bar at x400k, the actual distance between the areas, highlighted in red, can be measured. This distance in nm is the same for the following magnification at x500k. For pixel measurements, the scale bar can be calibrated as in the previous cases with the scale bar in the know distance in nm and pixel and the scale bar in pixel. With this method, the scale bar can be calibrated up to the highest magnification of x1.2M. However, due to the increasing challenge of pixel-accurate measurements and other influences such as perspective correction, the accuracy of calibration at higher magnifications is less than at lower magnifications with visible line spacing.

The scale bar has been calibrated for each magnification and camera length of the TEM.It is now possible to make accurate measurements on a sample with the external VS camera. The actual dimensions of a sample can now be calculated using the calibrated length of the scale bar and the pixel dimensions of both the feature on the sample and the scale bar. An overview of all calibrations for each TEM mode is given in the Table 3.1. The whole system is set up and ready to provide an alternative to the post-GIF TEM camera.

Table 3.1: Calibrated scale bar for each magnification and camera length

Magnification	Scale Bar [nm]	Camera Length	Scale Bar [1/nm]
x15k	3454	20cm	98.7
x20k	2621	25cm	79.5
x25k	2096	30cm	66.7
x30k	1760	40cm	50.2
x40k	1299	50cm	40.4
x50k	1050	60cm	33.5
x60k	880	80cm	25.7
x80k	657	100cm	20.5
x100k	525	120cm	16.8
x120k	439	150cm	13.5
x150k	346	200cm	10.3
x200k	253	250cm	8.1
x250k	210		
x300k	178		
x400k	136		
x500k	107		
x600k	89		
x800k	63		
x1M	51		
x1.2M	42		

All calibrated scale bar lengths for each magnification (x15k - x1.2M) and camera length (20cm - 250cm). The scale bar for image mode is given in nm. The scale bar for diffraction mode is given in 1/nm.

3.2 Comparison with Post-GIF TEM Camera

The TEM has a built-in camera that is calibrated after each filament change. It is controlled by the "DigitalMicrograph" program, which can also be used for analysis. The following is a detailed comparison of the two systems, as well as a characterization of the new external VS camera. It begins with a comparison of their characteristics, namely magnification levels, field of view and contrast. Finally, the accuracy of both systems is examined. The goal for both systems is to have a measurement error of less than 5%.

3.2.1 Magnification Levels

The first aspect to be examined is the magnification level in image mode and diffraction mode. For each mode there is a displayed magnification and a real magnification. The displayed magnification refers to the magnification level and camera length displayed by the TEM software. These are called "TEM Non-GIF Magnification" and "TEM GIF Magnification" for each camera system. The real magnification refers to the magnification of the projected image of the specimen and is called "VS Magnification" and "GIF Camera Magnification".

The real magnification in GIF mode for each displayed magnification is frequently calibrated and stored in DigitalMicrograph. In non-GIF mode, the real magnification for each displayed magnification can be derived from the ration of the real length of the scale bar $D_0 = 40\,\mathrm{mm}$ and the calibrated length of the scale bar D_1 in nm:

$$RealMagnification = \frac{D_0}{D_1} \tag{3}$$

This is done in image mode for each non-GIF magnification. The result and the corresponding magnifications for the GIF camera are in the Table 3.2. The real magnifications are always displayed to the first decimal point to allow a better comparison between both camera systems.

Table 3.2: Real magnification in image mode

TEM non-GIF mode	Viewing Screen	TEM GIF mode	GIF Camera
-	-	x150	x2.1k
-	-	x200	x2.7k
-	-	x250	x3.4k
-	-	x300	x4.1k
-	-	x400	x5.8k
-	-	x500	x7.3k
-	-	x600	x9k
x15k	x11.6k	x800	x12.8k
x20k	x15.3k	x1000	x16.7k
x25k	x19.1k	x1200	x17.7k
x30k	x22.7k	x1500	x24.2k
x40k	x30.8k	x2000	x33k
x50k	x38.1k	x2500	x41k
x60k	x45.5k	x3000	
x80k	x60.9k	x4000	x60.7k
x100k	x76.3k	x5000	x71.3k
x120k	x91.1k	x6000	x83k
x150k	x115.8k	x8000	x108.8k
-	-	x10k	x133.3k
x200k	x158.4k	x12k	x159k
x250k	x190.7k	x15k	x198.9k
x300k	x224.4k	x20k	x264.2k
x400k	x294.7k	x25k	x324.5k
x500k	x375.3k	x30k	x378.9k
x600k	x450.6k	x40k	x488.8k
x800k	x631.1k	x50k	x622.6k
x1M	x791k	x60k	x755.9k
x1.2M	x957.9k	x80k	x1M
-	-	x100k	x1.2M
-	-	x120k	x1.5M

For each magnification in GIF mode and non-GIF mode, the corresponding real magnification is shown next to it. The two magnifications where both modes have matching real magnifications are highlighted in yellow.

This table presents the displayed magnifications for both systems (”TEM non-GIF mode”, ”TEM GIF mode”) alongside the calculated magnifications (”Viewing Screen”, ”GIF Camera”). Two key magnifications in image mode are highlighted in yellow, where the actual magnifications of the VS and the GIF camera closely match, ensuring an accurate comparison between the two systems.

The real magnification for the camera length L in diffraction mode can be calculated with the diffraction angle of the electrons $2\,\theta$ and the radius R of the first diffraction ring as mentioned in Figure 2.4:

$$L = \frac{R}{\tan(2\theta)} \tag{4}$$

The diffraction angle can be derived from the Bragg condition in Equation 1 where the wavelength of the electrons in the TEM at 200 kV is $\lambda_{TEM} = 2.508\,\text{pm}$ and the d-spacing of the anatase in the [1 0 1] plane is $d_A = 3.516\,\text{Å}$. The radius R in real space must be calculated from the calibrated scale bar in reciprocal space with

$$R = k * \frac{D_0}{D_1} \tag{5}$$

where $k = \frac{1}{d_A}$ is the radius of the first ring in reciprocal space, D_0 is the length of the scale bar in cm and D_1 is the length of the calibrated scale bar in 1/nm. This was done for each camera length in non-GIF mode and the results are shown in Table 3.3.

Table 3.3: Real camera length in diffraction mode

TEM non-GIF mode	Viewing Screen	TEM GIF mode	GIF Camera
20cm	16.2cm	1.5cm	12.3cm
25cm	20.1cm	2cm	47.5cm
30cm	23.9cm	2.5cm	25.9cm
40cm	31.8cm	3cm	35.7cm
50cm	39.5cm	4cm	48.9cm
60cm	47.6cm	5cm	59.1cm
80cm	62cm	6cm	66.9cm
100cm	78cm	8cm	77cm
120cm	94.9cm	10cm	94.4cm
150cm	118cm	15cm	111.8cm
200cm	155.1cm	15cm	139.7cm
250cm	195.9cm	20cm	186.3cm
-	-	25cm	232.9cm
-	-	30cm	279.4cm
-	-	35cm	326cm

For each camera length in GIF mode and non-GIF mode, the corresponding real camera length is shown next to it. The camera length with matching values is highlighted in yellow.

This Table shows the displayed camera length for both systems (”TEM non-GIF mode” and ”TEM GIF mode”) and the calculated camera lengths (”Viewing Screen” and ”GIF Camera”). There is one important setting, highlighted in yellow, where the camera length is nearly identical in both systems. This is used to ensure the most accurate comparison between the two systems in diffraction mode.

Having determined the real magnifications for both camera systems in image mode and diffraction mode, it is now possible to compare their analytical capabilities. The focus is on the settings that have the same real magnification, highlighted in Table 3.2 and Table 3.3.

3.2.2 Field of View

In this comparison, the field of view refers to the area of the sample that can be observed at one time (Wright and Barrett, 2013). It depends on the number of pixels of the image sensor and the pixel resolution. The number of pixels is constant for each sensor. The pixel resolution is the area covered by one pixel and depends on the magnification of the TEM. In addition, the focal length of the lens of the DSLR affects the pixel resolution in non-GIF mode. To keep this variable constant, the focal length has been set to 35 mm. The shape of the area that can be captured depends on the camera system. The field of view is the observable area in image mode and is round for the VS ($A = \pi * \frac{d_{sensor}^2}{4}$) and square ($A = d_{sensor}^2$) for the GIF camera. Both areas depend on the diameter of the image sensor (d_{sensor}), which can be calculated with:

$$d_{sensor} = NumberOfPixels * PixelResolution \tag{6}$$

for every magnification. The "NumberOfPixels" refers to the number of pixels of the diameter of the sensor of the GIF camera or the number of pixels which cover the diameter of the VS. The "pixel resolution" can be derived from the previously calibrated scale bar. This gives the field of view for each magnification in nm^2.

To compare the field of view, the same real magnification is compared for both systems. The field of view for the VS at the displayed magnification of x200k (real magnification of x158.4k) has an area of 756.971 nm^2. The field of view for the GIF camera at a displayed magnification of x12k (real magnification of x159k) has an area of 32.616 nm^2. This results in an area of the VS that is 23 times larger than the area of the GIF camera. The advantage of the VS is the larger field of view and makes it possible to examine a larger area of a sample at the same magnification.

3.2.3 Contrast

Contrast refers to the difference in brightness or intensity between different parts of an image (Rahimi-Nasrabadi et al., 2021). In analysis, high contrast helps distinguish features and structures of specimens from each other and from the background. In general, the intensity value ranges from 0 to 255 and can be measured for each pixel. The highest value corresponds to white and the lowest value corresponds to black. As the intensity decreases from 255, the corresponding pixel becomes grayer and darker. The maximum contrast value is 255 for the difference in intensity between black (0) and white (255).

With DigitalMicrograph, it is possible to draw a line across the region of interest and generate a 1D intensity plot along the length of the line. This can be used to measure the difference in intensity and compare the peak and average intensity. For this measurement, the image must first be converted to a grayscale image. This can be done with any standard image program.

For this comparison, the same real magnification is used for the image mode (non-GIF mode: x80k, GIF mode: x4000) and for the diffraction mode (non-GIF mode: 120cm, GIF mode: 10cm). For the image mode, two possible scenarios are investigated. First, the contrast between the sample and the background, and then the contrast between features on the sample. The sample used is TiO_2 nanoparticles, as a good contrast is necessary to distinguish between the particles and the background. Also, unique features on the sample help to take measurements at the exact same spot. The area of interest of the sample as well as the lines for measuring the contrast are shown in Figure 3.8.

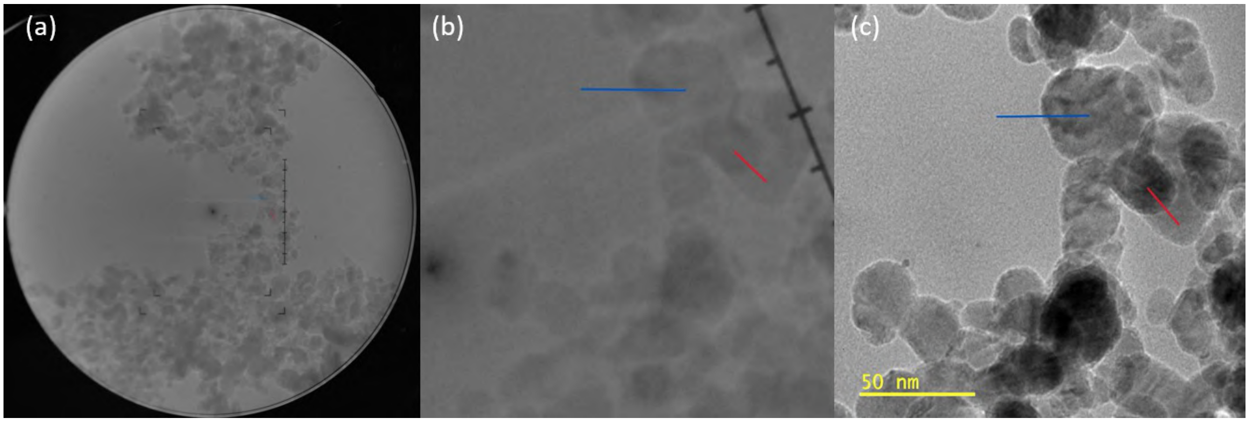

Figure 3.8: Contrast measurement in image mode

Contrast measurement for each system in image mode. Image of the VS on the left (a) and the GIF camera on the right (c). A cropped image of the VS in the center (b) to match the area of the GIF camera. All images show the intensity measurements in blue (background to particle) and red (particle to particle).

This is a measurement of the change in intensity between the background and a particle and between two particles. On the left is the area on the sample taken with the VS camera. On the right is the same area on the sample, but taken with the GIF camera. In the center of the Figure 3.8 is a cropped part of the image from the VS camera to match the area of the GIF camera and to give a better overview of the measurement. The blue and red lines represent the measurements. The blue line corresponds to the measurement of the intensity change from background to particle and the red line corresponds to the measurement between two particles. The lines are in the same position and have the same length for both camera systems. The result of the contrast measurement between particle and background (blue line in Figure 3.8) is shown in Figure 3.9.

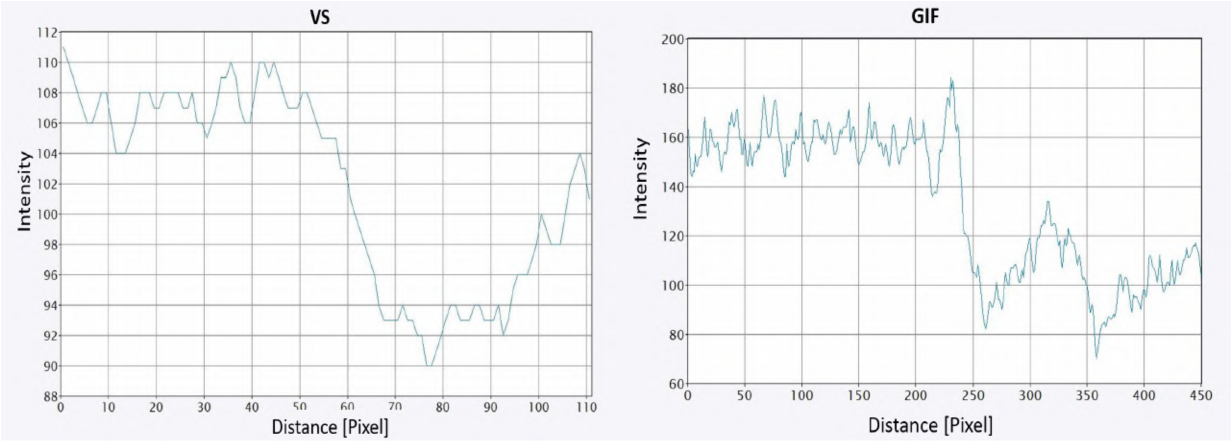

Figure 3.9: Contrast between background and particle

Measurement of the intensity (x-axis) over the distance of the line in pixels (y-axis). Comparison of the change in intensity of the VS (left) and the GIF camera (right) between the background and a particle of the sample (blue line in Figure 3.8). The GIF camera has better contrast due to the larger difference in intensity between the background and the particle. (Gatan Inc., 2024)

These are the 1D intensity plots of the measurement. On the left is the graph for the VS image and on the right is the graph for the GIF image. The x-axis of the graph is the length of the line in pixels and the y-axis is the intensity value. The length in pixels varies between the two cameras because of their pixel resolution. The highest value for the VS contrast is 20. This is the difference in intensity between the peaks at 110 and 90. In comparison, the highest contrast value for the GIF camera is 115, with peaks at 185 and 70. After averaging the intensity for the particle and background and measuring the change in intensity, the result is similar. The average contrast of the VS is lower at 15, with the average intensity of the background at 108 and that of the particle at 93. For the GIF camera, the average contrast is 65 with the background intensity at 160 and the particle at 95. The same comparison was done to examine the contrast between two particles (red line in Figure 3.8) and can be seen in Figure 3.10.

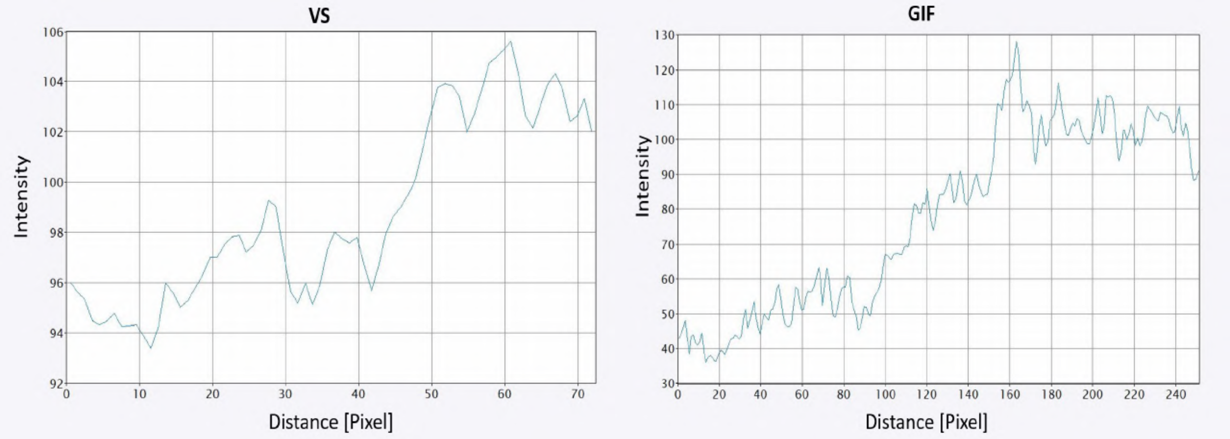

Figure 3.10: Contrast between two particles

Measurement of the intensity (x-axis) over the distance of the line in pixels (y-axis). Comparison of the change in intensity of the VS (left) and the GIF camera (right) between two particles of the sample (red line in Figure 3.8). The GIF camera has better contrast due to the larger difference in intensity between the particles. (Gatan Inc., 2024)

These 1D intensity plots correspond to the red line measurement of two overlapping particles from Figure 3.8. The arrangement and layout is the same as the previous comparison in Figure 3.9. The highest value for the contrast of the VS is 11, with a difference of 105 to 94. The highest value for the contrast of the GIF camera is 87, with a maximum of 124 and a minimum of 37. The average contrast follows a similar trend. The average contrast of the VS is 7 with the average intensity of one particle at 103 and the other particle at 96. The average contrast for the GIF camera is 55 with the average intensity of the background at 105 and the intensity of the particle at 50.

The same test was performed in diffraction mode with the same sample as before at the same real magnification for both systems (non-GIF mode: 120cm, GIF mode: 10cm). The contrast measurements were made on the first diffraction ring because it is the most pronounced with the highest intensity at its peak. The measurements are shown in Figure 3.11.

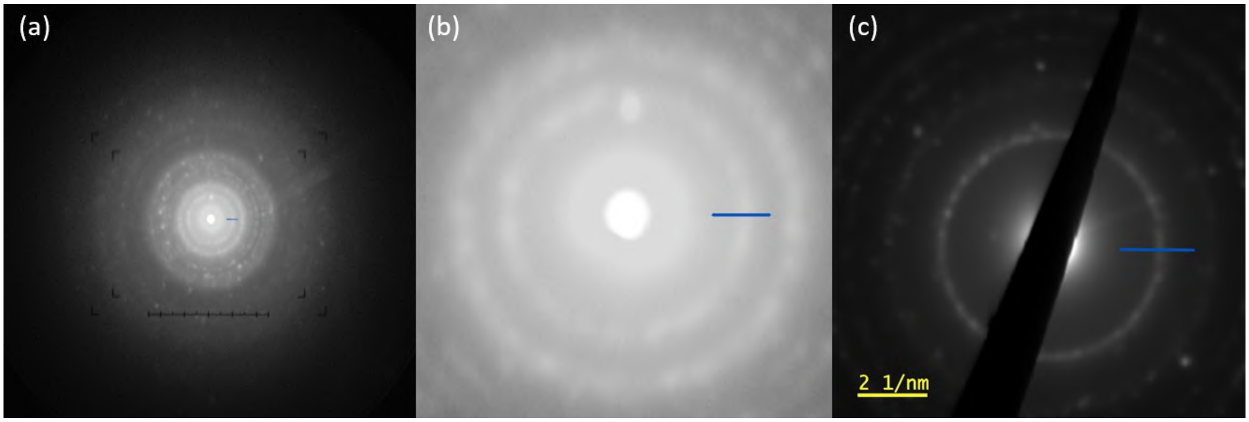

Figure 3.11: Contrast measurement in diffraction mode

Contrast measurement for each system in diffraction mode. Image of the VS on the left (a) and the GIF camera on the right (c). A cropped image of the VS in the middle (b) to match the area of the GIF camera. All images show the intensity measurements in blue.

On the left is the diffraction pattern on the VS. On the right is the same pattern captured by the GIF camera. In the center is a cropped image of the VS image to match the area of the GIF camera. The blue line in each image represents the intensity measurement. In Figure 3.12 is the corresponding 1D intensity diagram.

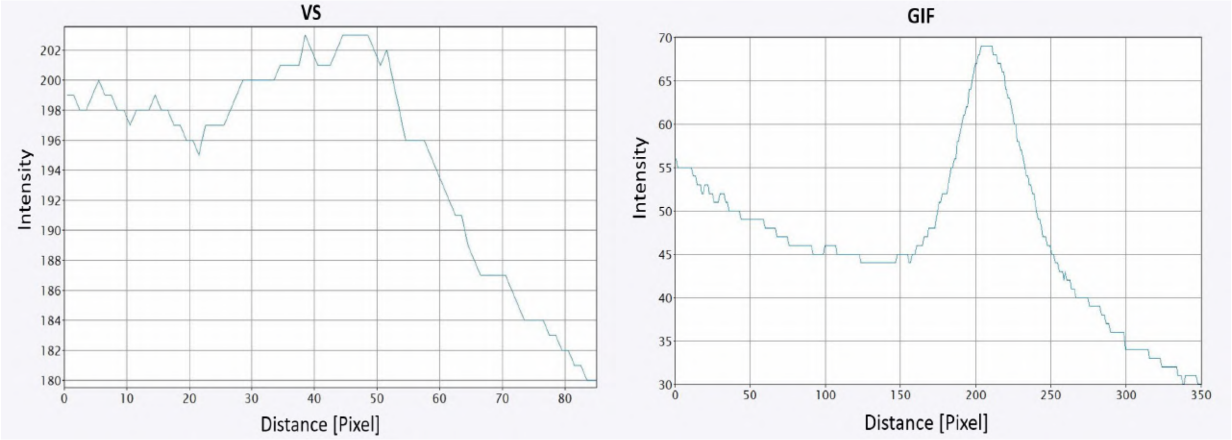

Figure 3.12: Contrast between diffraction ring and background

Measurement of the intensity (x-axis) over the distance of the line in pixels (y-axis). Comparison of the intensity change of the VS (left) and the GIF camera (right) in diffraction mode (blue line in Figure 3.11). The GIF camera has better contrast due to the larger difference in intensity between the peak of the ring and the background. (Gatan Inc., 2024)

The arrangement and layout is the same as the previous comparison in Figure 3.9. For the diffraction mode, only the peaks of the diffraction pattern are of interest, so only the maximum contrast is compared. The contrast value for the VS is 23, from the peak at 203 to the lowest point at 180, and for the GIF camera is 39, from the peak at 69 to the lowest point at 30. The total intensity decreases from the center of the diffraction pattern because this background noise is caused by the scattering of the electrons at the beam stopper and decreases with distance.

The GIF camera's overall contrast is better in both image mode and diffraction mode, which helps with accurate analysis. The value for the contrast of the VS is acceptable. The intensity can vary between measurements because it depends on the overall brightness of the image, which can be affected by many factors (e.g. sample, exposure time, ambient brightness). However, the ratio of the intensity peaks remains consistent.

3.2.4 Comparison of Measurement Error

After characterizing both cameras, their measurement capabilities will be compared to the gold standard from Chapter 3.1.3. The goal for the implementation of the external VS camera is to have a measurement error below 5%. The measurement error refers to the relative average deviation of the measured length from the actual length of the sample. With the known dimensions and material of the gold standard, it is possible to calculate the measurement error with both cameras in image mode and diffraction mode. The comparison of both systems is done at the same real magnifications for image mode and diffraction mode , as is shown in Figure 3.13 and Figure 3.14 respectively.

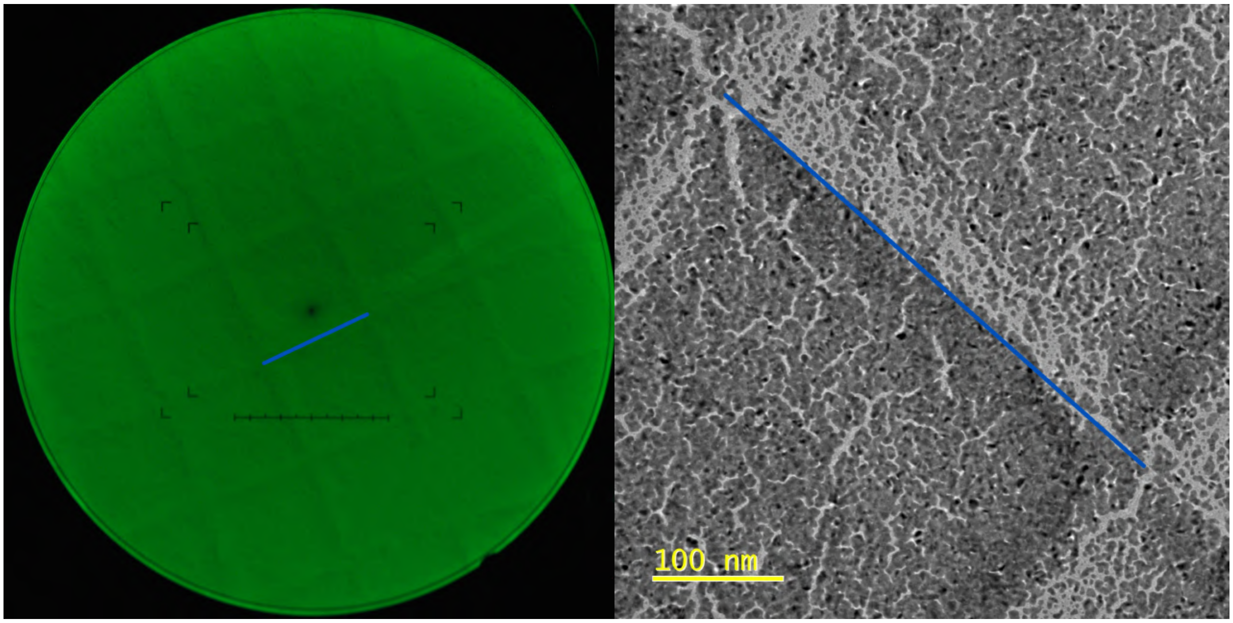

Figure 3.13: Measurement error in image mode

Comparison of the measurement error in image mode. The deviation of the distance between two lines on the standard (463 nm) was measured for both the VS (left) and the GIF camera (right).

On the left in Figure 3.13 is the image from the VS at x80k in non-GIF mode and on the right from the GIF camera at x4000 in GIF mode. Both have the same real magnification of x61k. The blue line is the measured distance. The real distance between the two lines is 463 nm. The results are shown in Table 3.4.

Table 3.4: Measurement error in image mode

	Standard [nm]	Measurement [nm]	Deviation [%]
GIF	463	451.2	-2.6
VS	463	486.8	4.9

Deviation of the measurement in image mode for both systems. Shows the standard length and the measured length in nm and the relative deviation in %. The GIF camera is the more accurate system because it has the smaller relative deviation.

This table shows the measurements for both systems in nm and their relative deviations from the standard in %. The measurement error in image mode and is -2.6% in GIF mode and 4.9% in non-GIF mode. The same measurement was made in diffraction mode. In GIF mode with a camera length of 10cm, only the first two rings of the diffraction pattern can be captured. This limits the comparison to these rings as shown in Figure 3.14.

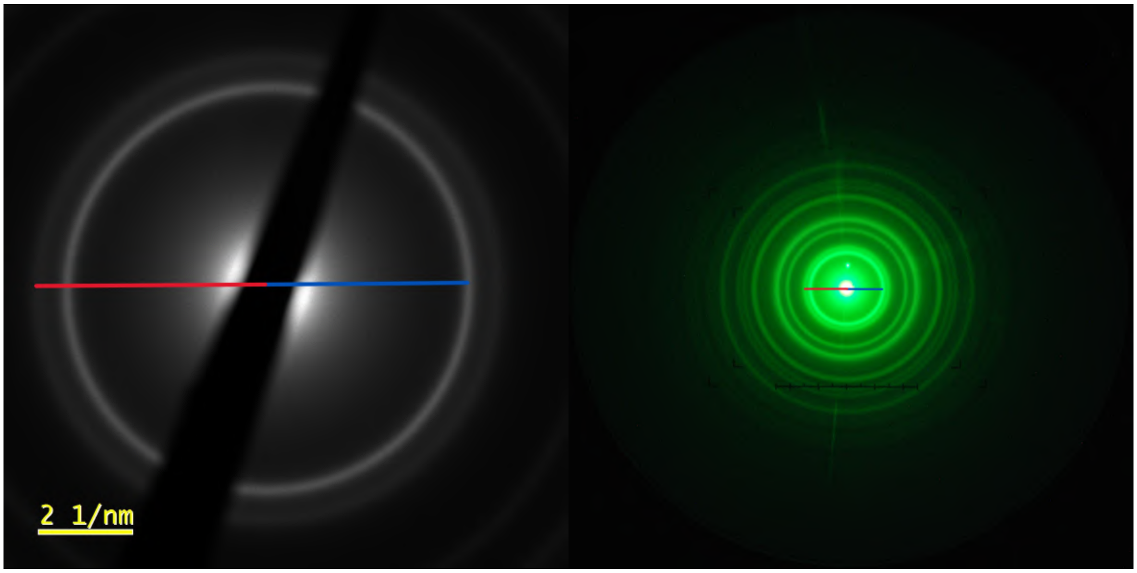

Figure 3.14: Measurement error in diffraction mode

Comparison of measurement error in diffraction mode. The radius of the first (blue) and second (red) diffraction ring were measured for both the VS (left) and the GIF camera (right).

On the left in Figure 3.14 is the image from the VS at 120cm in non-GIF mode and on the right is the image from the GIF camera at 10cm in GIF mode. Both have the same real camera length oof 94cm. The blue line represents the measured distance for each ring. The results of this measurement can be found in Table 3.5.

Table 3.5: Measurement error in diffraction mode

	Model r [1/nm]	VS r [1/nm]	Deviation [%]	GIF r [1/nm]	Deviation [%]
Ring 1	2.358	2.341	1.7	2.319	0.8
Ring 2	2.039	2.029	2.0	1.999	0.6
Average			1.8		0.6

Deviation of measurement in diffraction mode for both systems. Shows the radius of the first and second diffraction ring for the model and the measured radius in 1/nm. The relative deviation in % is shown next to each system measurement. The GIF camera is the more accurate system because it has the smaller relative deviation.

For each ring, the real distance and the measured distance in GIF and non-GIF mode are given in 1/nm. Their relative deviations are shown next to the measurement in %. The deviations are averaged over all measured rings. This results in a relative deviation of 0.6% in GIF mode and 1.8% in non-GIF mode.

Overall, the measurement errors for both systems, in both image mode and diffraction mode, are below 5% and thus suitable for measurements. Finally, it should be noted that this is not a substitute for a thorough analysis of the measurement system. The sample size and number of measurements is too small to make a definitive statement about the measurement error. However, it is a good representation and can be used as a first impression, especially for the external VS camera.

3.3 Resume

Getting the external VS camera up and running began with setting up and calibrating the DSLR. It is mounted on a custom-built tripod in front of the VS. The aperture is fixed at f/8 and the ISO sensitivity at 800. The exposure time is variable and depends on the image mode and diffraction mode, but is usually best at 2.5 s and 10 s respectively. The perspective of the images must be corrected for the angle of the camera relative to the screen using DxO Viewpoint. The pixel measurements are done with ImageJ.

Next, the calibrated external VS camera was compared to the already integrated internal post-GIF TEM camera. Several aspects of each camera system were examined. Starting with the general similarities and differences of both systems and their handling. This was followed by a detailed analysis focusing on magnification levels, field of view and contrast. To conclude, the measurement error of both systems was evaluated and compared. Each system has its own advantages, disadvantages and applications.

The advantage of the GIF camera is its wider range of magnification from x2.1k to x1.5M, higher pixel resolution and better contrast. It is also the more accurate system for measurement and sample analysis, as its measurement error is 0.6% in diffraction mode and -2.6% in image mode.

The advantage of the DSLR is its much larger field of view, which is 23 times larger than the GIF camera at the same magnification level. It is also the more stable system as it cannot be damaged by the electron beam of the microscope. The GIF camera is very susceptible to damage and can quickly be out of service for some time. As long as the TEM remains functional and the VS can be used, the DSLR is capable of capturing images, ensuring that research activities continue uninterrupted. Finally, the external VS camera system is easier to learn because it has fewer settings and is less prone to damage.

4 In Situ Transmission Electron Microscopy of TiO_2

After the successful commissioning of the external VS camera within the microscope environment, the in situ study of the thermal stability of Titania can begin. However, prior to the experiment, it is essential to have a thorough understanding of the material and its production process. Titania has been synthesized since the 1940s (Evonik, 2017) and was first studied with electron microscopes in the 1950s (Czanderna et al., 1958). Both the historical development of research and the current state of the art must be reviewed. Finally, the Protochips system used for the in situ study is presented.

4.1 Introduction to TiO_2

Titanium dioxide, also known as Titania, is an inorganic compound with the chemical formula TiO_2 that occurs naturally in minerals but is most commonly synthesized industrially (Koparde and Cummings, 2008). It consists of one titanium and two oxygen atoms and has different phases. In general, different phases correspond to different structures and orientations of the atoms in the material, even though they have the same chemical formula (Borchardt-Ott and Sowa, 2018). This can result in different properties and behaviors of a material depending on the phase. The most common phases of Titania are rutile, anatase and brookite (Hanaor and Sorrell, 2011). Rutile is the only stable phase, while anatase and brookite are the metastable phases at all temperatures. A phase in a stable phase, also called a stable equilibrium, is in its lowest energy state. A metastable phase, also called a metastable equilibrium, can change its phase when additional energy is introduced into the system. This allows the metastable phase to transform into the stable phase. The transformation from a metastable phase to a stable phase is a non-reversible process (Buschow et al., 2001). The focus will be on the transformation from the metastable anatase phase to the stable rutile phase. Brookite will not be discussed further as it is known to be an intermediate phase in the anatase-rutile transformation (Lee and Zuo, 2004). Its unique properties as a nanocrystalline material can be used for numerous material applications and is phase dependent. Rutile is mainly used as a white pigment in paints, sunscreens and foods (Ntsikelelo et al., 2020). Anatase is an interesting material for use in dye-sensitized solar cells, photocatalysis and optoelectronics as it is already a widely used material (Reyes-Coronado et al., 2008). It has non-toxic properties, is available at low cost and has strong oxidation and reduction capabilities under solar light. It is particularly interesting for use as a photocatalytic material because of its ability to decompose organic pollutants (Ntsikelelo et al., 2020). Since the unique properties of anatase for its specific applications are lost after transformation to rutile, it is essential to understand the thermal stability of the phases.

The crystal system for both phases is tetragonal and their class is ditetragonal dipyramidal (Rezaee et al., 2011; NAVROTSKY and KLEPPA, 1967). The phases differ in their cell parameters, volume and density. An overview of both structures and their unit cells can be seen in Figure 4.1.

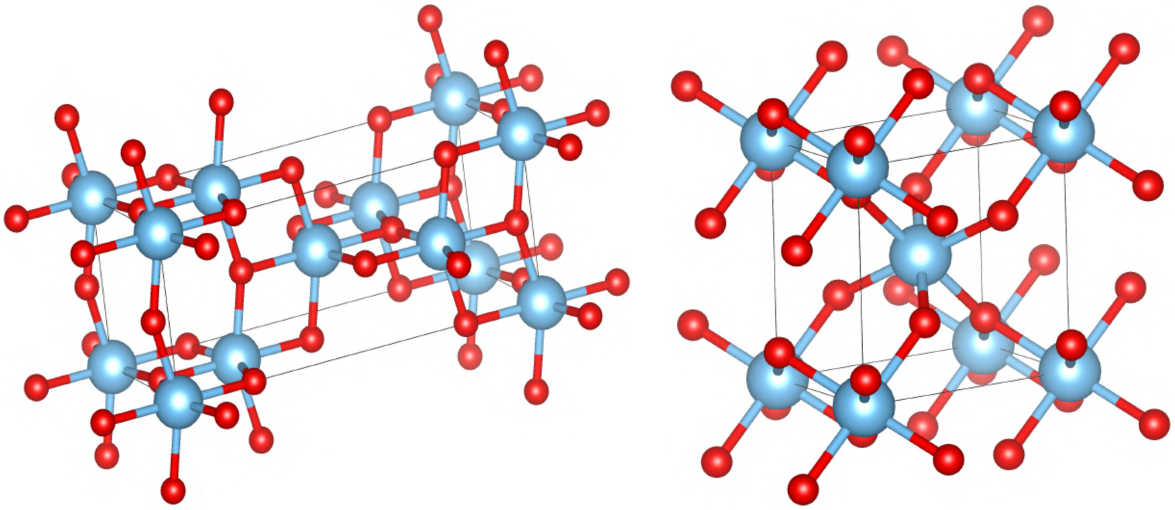

Figure 4.1: Crystal structure of anatase and rutile (generated with Momma and Izumi, 2024)

Unit cell of anatase (left) and rutile (right). Titanium atoms are shown as blue spheres and oxygen atoms as red spheres.

The titanium atoms are shown as blue spheres and the oxide atoms as red. The anatase unit cell is shown on the left and the rutile phase on the right in Figure 4.1. Both phases belong to the same tetragonal crystal system but to different space groups (anatase: $I4_1/amd$, rutile: $P4_2/mnm$). Rutile is the more compact phase because the unit cell contains only two TiO_2 compared to four in the anatase unit cell. Consequently, the cell parameters are also different, as shown in Table 4.1.

Table 4.1: Cell parameters of anatase and rutile

Cell parameters	Anatase	Rutile
$a = b$[Å]	3.785	4.594
c [Å]	9.514	2.959
$\alpha = \beta = \gamma$	90°	90°

Cell parameters for the anatase and rutile phase of Titania with the lattice constant (a,b,c) in nm and the angle (α, β, γ). (Rezaee et al., 2011; NAVROTSKY and KLEPPA, 1967)

Rutile has a more compact structure due to a much smaller c-cell parameter. The phase transformation from anatase to rutile depends on many different parameters. In general, the transition onset temperature, as determined by X-ray diffraction measurements, is around 600 °C (Hanaor and Sorrell, 2011). The effect of pressure and temperature is shown in Figure 4.2.

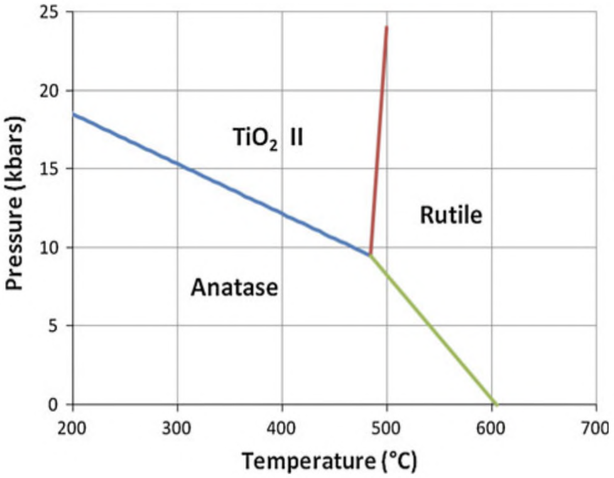

Figure 4.2: Pressure-temperature diagram of Titania phases (from Hanaor and Sorrell, 2011)

Influence of pressure (y-axis) on transformation temperature (x-axis) of the Titania phases in bulk material. Important is the transformation from anatase to rutile (highlighted in green). A decrease in pressure results in a higher transformation temperature (Hanaor and Sorrell, 2011).

Important is the transition temperature line from anatase to rutile shown in green in Figure 4.2. This visualizes the change in transition temperature under pressure. For the in situ experiments, where the pressure in the high vacuum of the microscope is very low, the transformation temperature is about 600 °C. However, this diagram is only valid for bulk pure anatase in air and should serve as a reference point. There are many influences on the phase transformation temperature, including (Hanaor and Sorrell, 2011):

- Particle size
- Particle shape (aspect ratio)
- Surface area
- Atmosphere
- Volume of sample
- Nature of sample container
- Heating rate
- Soaking time
- Impurities (from raw materials and container)
- Measurement technique

4.2 Production of TiO_2

Before reviewing the state of the art on the behavior of Titania, it is important to first consider its manufacturing process, as it significantly affects various properties of the final product. Parameters such as particle size, shape and surface area are directly related to the manufacturing process. Titania can be synthesized by various methods, such as the chloride or sulfate process. For the experiments, the AEROXIDE® TiO_2 P25 from Degussa, now Evonik, is used.

Evonik uses a pyrogenic process to produce metal oxides such as Titania (Evonik, 2017). The pyrogenic process is a flame synthesis in which all reactants are transferred to the gas phase and fed to the oxyhydrogen flame as a homogeneous mixture. Metal oxides are produced by the evaporation of metal chlorides. Hydrogen chloride gas (HCl) is produced as a by-product. The complete process for the production of metal oxides is shown in Figure 4.3.

Figure removed due to copyrights issues

Figure 4.3: Flame synthesis of metal oxides (translated from Evonik, 2017)

Schematic diagram of the flame synthesis process for the production of metal oxides. The educts (oxygen and metal chloride) are vaporized, combined and then burned with hydrogen in the burner. After cooling, the HCl is separated from the metal oxide and stored in a silo after deacidification (Evonik, 2017).

The metal chloride, in Titania's case titanium chloride ($TiCl_4$), is vaporized and mixed with air, primarily oxygen, in the mixing chamber. This homogeneous mixture is then fed into the burner with hydrogen, resulting in the rapid hydrolysis of $TiCl_4$ within a fraction of a second. The resulting aerosol is cooled and the solid phase is separated from the corrosive gas. During deacidification, hydrochloric acid (HCl) is removed from the surface of the titanium oxide product. The entire process is summarized by the following chemical reaction:

$$\mathrm{TiCl_4 + 2\,H_2 + O_2 \longrightarrow TiO_2 + 4\,HCl} \tag{7}$$

The main properties of the metal oxide are determined during flame synthesis. The product can be influenced by varying the concentrations of each reactant, the temperature of the flame and the time in the burner. This directly affects the resulting particle size, its distribution, specific surface area and surface properties. To understand the resulting composition of AEROXIDE$^{®}$ TiO_2 P25, the process is described in a simplified droplet model in Figure 4.4.

Figure removed due to copyrights issues

Figure 4.4: Simple model of particle genesis in the flame (translated from Evonik, 2017)

Formation of agglomerates during flame synthesis of nucleides. The evolution and combination of particles is shown in the upper half. The process during heating and cooling is shown below in a chamber. First the nucleides react and collide to form primary particles. These then collide to form aggregates. With cooling and further collisions, agglomerates are formed. The result is the AEROXIDE® P25 powder (Evonik, 2017).

The upper part of Figure 4.4 shows the formation of nucleides before their interaction in the flame, leading to the final product in larger agglomerates. Below is a visualization of the flame as a space with rapidly rising and falling temperatures. This space is divided into four sections corresponding to the different stages of agglomerate formation. It starts on the left when hydrolysis begins with the formation of tiny droplets (nucleides) in the flame after the metal chloride, oxygen and hydrogen combine in the chamber. The nucleides collide and merge to form larger droplets. These can also collide and gradually increase in size and weight, resulting in the formation of primary particles. When the primary particles reach a colder part of the flame, they begin to solidify. Collisions no longer result in complete fusion, but only partially. This starts the formation of aggregates from the primary particles. They continue to solidify in the cold region and are unable to fuse with other particles or aggregates. Instead, in the final section, multiple aggregates are deposited together through weak interactions and form agglomerates. This process can be used to produce high purity metal oxides with specific property profiles. The relative composition of the crystal phases can be precisely regulated through optimized process control.

The AEROXIDE® TiO_2 P25 is produced by this process and, due to the fine nature of the resulting aggregates, has minimal pigment properties, which is typically the most common application for Titania. It is therefore particularly useful in certain technical applications where a very high specific surface area is desired. It is mainly used as a catalyst carrier and as an active component in photocatalytic reactions or as a heat stabilizer for silicones (Evonik, 2017).

Radiographically, AEROXIDE® TiO_2 P 25 consists of approximately 85% anatase and 15% rutile. Despite the production conditions (flame hydrolysis), the thermodynamically more stable rutile phase is present to a much lesser extent. Typically, anatase transforms to rutile at elevated temperatures, especially when the flame reaches temperatures around 2000 °C. The rutile phase preferentially concentrates on the particle surface and is intensely interlocked with the anatase phase.

The final product of flame hydrolysis has a very high purity with a titanium dioxide content of over 99.5%. This is due to annealing at 1000 °C for two hours. This treatment is necessary to obtain a constant reference point, since the physisorbed water (drying loss) and the chemisorbed water (annealing loss) must be taken into account by weight due to the large specific surface area. The average particle size was measured to be about 24 nm with a standard deviation of 5 nm.

4.3 Time-Dependent Changes of TiO_2 at High Temperatures

Titania was obtained by flame hydrolysis as early as 1940. Starting in the 1950s, the properties of the phase transformation were studied using electron microscopy. Research on the material continues today, as the anatase phase is of interest for use in sustainable energy production in photovoltaic. Due to the many influencing factors, the thermal stability is still not fully understood.

The anatase-rutile transformation was studied as early as 1957. The anatase phase completely transformed to rutile when heat treated at 728 °C for 4 h. (Czanderna et al., 1958) Temperature also affects the rate at which anatase transforms into rutile. Below 610 °C the rate starts slow and increases rapidly above 730 °C. Czanderna (1957) stated that the "transformation process was found to be influenced by various factors, including time, temperature and the presence of thermal defects and foreign impurities". The study concluded that the atmosphere had no significant impact on the kinetics of the phase change, as it did not affect the experimental outcomes. However, another study in 1961 did find an influence of pressure on the transformation, albeit a small one. There, Titania transformed completely from anatase to rutile after 3 h at 900 °C. The transformation rate decreased with rising partial pressure of oxygen, air and argon, but grain growth did not seem to be affected (IIDA and OZAKI, 1961). In 1966, Vahldieic found that the transformation rate followed a slow of $dTdP = -0.02\,^{\circ}\mathrm{C\,bar}^{-1}$ (Vahldiek, 1966).

In 1997, the influence of particle size on transformation rate and temperature was studied, revealing that the transformation rate increased significantly when the reacting anatase was very finely crystalline (Gribb and Banfield, 1997). The transformation rate was tested between 465 °C and 525 °C, with an average anatase particle size of 25 nm. Both anatase and rutile particle sizes increased gradually over time, with the growth rate significantly accelerating at higher temperatures. At the highest temperature of 525 °C, 80% of the nanocrystalline anatase transformed into rutile after 24 h. This study supported previous findings (cf. Banfield et al., 1993; Suzuki and Tukuda, 1969) that phase stabilities are reversed at small crystal sizes, while Navrotsky and Kleppa found no phase transformation at 700 °C after 24 h (NAVROTSKY and KLEPPA, 1967).

A study was completed in 2001 that tested commercially available TiO_2 powders (Gouma and Mills, 2001). The titania powders had an average particle size of 100 nm. The powder was heated in a tube furnace at 1000 °C between 3 h and 24 h. The first complete phase transformation from anatase to rutile occurred after 8 h. From their experiments, they were able to conduct three possible scenarios for the transformation and growth of rutile from anatase, as shown in Figure 4.5.

Figure removed due to copyrights issues

Figure 4.5: Scenarios for anatase to rutile transformation (from Gouma and Mills, 2001)

Three scenarios for the transformation process from anatase to rutile. First, single rutile crystals are formed by sintering (a). Second, individual anatase particles transform and then adhere to each other (b). Third, anatase particles attach to a rutile particle and rotate to the same crystallographic orientation as the rutile particle (Gouma and Mills, 2001).

In the first scenario on the left (a), the anatase particles sinter and form a single crystal. This forms a large rutile particle after transformation. In the second scenario (b), single crystals of anatase transform to rutile. These transformed particles adhere to each other and rotate to achieve a single orientation, resulting in a single large rutile crystal. In the final scenario (c), anatase particles attach to a rutile particle. The anatase particles then rotate to obtain a favorable crystallographic orientation for the reaction. The particles interact to form a large single crystal of rutile.

In 2004, the absorption of anatase particles into rutile was observed (Lee and Zuo, 2004). The rutile particles then grew by coalescence. The phase transformation temperature was 750 °C. Once the rutile has nucleated, its growth is accelerated by the absorption of the surrounding anatase particle. The growth of the rutile particle stops when all the surrounding anatase particles are absorbed.

The influence of particle size on the transformation rate was further investigated in 2003, where different batches of TiO_2 powders were heated for 2 h at 550 °C, 600 °C, 650 °C and 700 °C (Hu et al., 2003). They found a nearly linear correlation between the average size of anatase and the percentage of transformation to rutile, as shown in Figure 4.6.

Figure removed due to copyrights issues

Figure 4.6: Linear correlation of particle size and transformation rate (from Hu et al., 2003)

The % of anatase transformed into rutile (x-axis) versus the average size of anatase in nm (y-axis). The spots correspond to experiments at different temperatures. The dashed trend line suggests a linear correlation between anatase particle size and the transformation rate with a critical size at 15 nm (Hu et al., 2003).

The x-axis is the percentage of anatase transformed to rutile. The y-axis is the average particle size of anatase in nm. The different shaped spots represent the heat treatment at different temperatures. There is a clear linear correlation between the percentage of transformed anatase and the corresponding particle size. This means that a larger anatase particle is more likely to transform into rutile. The intersection on the y-axis at 15 nm indicates that the critical crystallite size for anatase, from a thermodynamic point of view, is 15 nm for phase transformation. The onset of phase transformation depends on the growth of anatase particles to attain the critical size.

Another study in 2010 investigated the phase transformation temperature of nanocrystalline titania powders (Ayache et al., 2010). The transformation temperature of the powder with an average particle size of 32 nm was 650 °C after 4 h. Compared to the previous study (Gouma and Mills, 2001) with the same experimental setup but different particle size (100 nm), the transformation occurred much faster. This further supports the hypothesis that the transformation temperature decreases with decreasing particle size.

In 2020 an experiment was conducted to observe the change in particle shape of nanoparticle Titania (Ntsikelelo et al., 2020). The size of the particle depends on the annealing temperature. At 400 °C the average size is 19.799 nm. When heated to 700 °C the average particle size increases to 38.685 nm. They also confirmed by XRD and Raman spectroscopy the formation of a hybrid anatase and rutile phase at 400 °C. When heated in a tube furnace, the nanoparticles developed a spherical structure, with both the growth rate and the particle size increasing as the annealing temperature rose.

A study looking at the critical particle size for the transformation from anatase to rutile was done in 2021 (Bachina et al., 2021). They looked at both heat-stimulated crystallization and phase transformation of Titania. An amorphous titania-based precursor was synthesized and heated in a high temperature powder XRD to 1100 °C in steps of 100 °C every 10 min. The measurements are shown in Figure 4.7.

Figure removed due to copyrights issues

Figure 4.7: Correlation phase, crystal size and temperature (from Bachina et al., 2021)

Temperature in °C (x-axis) versus molar proportion in mol % in (a) and crystallite size in nm in (b). In (a) the amorphous phase changes completely to anatase from 200°C to 700°C and further transforms to rutile from 700°C to 900°C. In (b) the change in particle size is shown for anatase (from 300°C to 800°C) and rutile (from 800°C to 1100°C). This indicates a strong correlation between crystal size and transformation temperature (Bachina et al., 2021).

The first graph (a) illustrates the transformation from amorphous to crystalline structure and the phase transformation from anatase to rutile. The x-axis represents the temperature used in the experiment, ranging from 200 °C to 1100 °C, while the y-axis indicates the molar proportion of the phases. Initially, the powder is 100% amorphous. After heating to 200 °C the amorphous phase begins to crystallize into anatase. This process continues until the temperature reaches 700 °C and all of the amorphous phase crystallize into the anatase phase. From 700 °C to 900 °C the anatase phase completely transforms to rutile. Above 900 °C anatase is no longer present. In the second diagram (b) in Figure 4.7 the crystallite size in nm is plotted on the y-axis and the temperature range from 200 °C to 1100 °C is plotted on the x-axis. The anatase phase starts to crystallize at 300 °C with a particle size of 10 nm. With rising temperature the crystal size of anatase increases and reaches its maximum of 40 nm at 800 °C. With the phase transformation from anatase to rutile the particle size enlarges to 60 nm. A further increase in temperature doesn't change the size of the rutile particles. The study concluded that the average crystal size of anatase reaches between 35 nm and 45 nm as the phase transition to rutile occurs between 700 °C and 900 °C (Bachina et al., 2021).

Anatase phase transformation has been studied since 1959 and considerable progress has been made since then. Many factors influence the transformation temperature and rate, as a ”complicating factor in the understanding of nanoparticle formation is the multitude of experimental conditions used for synthesis of the different TiO_2 phases, making it difficult to compare mechanisms” (Reyes-Coronado et al., 2008). While atmospheric pressure has a small effect on the rate, particle size plays a large role, with smaller particles leading to lower transformation temperatures. The increased stability of nanocrystalline anatase is particularly noteworthy. In addition, factors such as particle orientation and proximity to other particles can also affect the transformation temperature. However, the exact particle size at which the anatase-rutile transformation becomes possible, as well as the critical size at which the transformation becomes inevitable, remains uncertain. Before answering these questions it is important to first get to know the specific behavior of the Titania from Evonik (AEROXIDE® TiO_2 P25) to be able to isolate its characteristics and their influence on the transformation from anatase to rutile.

4.4 In Situ Heating System

The Aduro holder from Protochips allows in situ heat treatment and thermal stability studies of Titania. With the holder and the Fusion Select Heating E-chip (E-FHDS-VO-10) it is possible to heat treat the sample inside the TEM. This system allows real-time analysis of phase transitions and structural changes in Titania under different temperature conditions (Protochips, n.d.(b)).

Protochips specializes in in situ experimental control to enhance the analysis and resolution capabilities of electron microscopy. They produce sample holders and chips that can electrically and thermally manipulate the sample inside the electron microscope. Especially interesting for the observation of the phase transformation from anatase to rutile is the possibility to heat the sample up to 1000 °C (Protochips, n.d.(b)). The whole setup consists of the E-chip, the Aduro sample holder and the peripherals.

The chip used to heat the sample is the Fusion-Select-Heating E-chip and is shipped in batches of 10. Each batch is assigned a serial number and each chip has its own unique number along with a corresponding calibration file (Protochips, 2020). The chip is 4 mm long, 4.65 mm wide and 300 µm high. There are electrodes on the top that are connected to a membrane in the middle. The ceramic heating membrane has a 40 nm thick supporting silicon nitride film. There are nine holes in the membrane with a diameter of 8 µm arranged in a 3x3 array with a spacing of 12 µm. These holes provide an electron transparent area for TEM imaging. The ceramic film around the holes on the membrane has a thick polycrystalline structure, making TEM imaging impossible. An image of the chip structure is shown in Figure 4.8.

Figure removed due to copyrights issues

Figure 4.8: Construction of a Fusion-Select-Heating E-chip (from Protochips, 2020)

Schematic overview of the E-chip from Protochips. The red base with yellow contacts on top has a ceramic membrane in between (highlighted in blue). An enlarged image of the membrane is shown next to the model. The membrane has a silicon nitride support film and 9 holes that are used for the study of the sample. The area around the holes is not transparent to the electron beam of a TEM (Protochips, 2020).

This figure shows a schematic overview of the chip's construction, with the base in red and the yellow electrical contacts on top. Both are connected by the membrane in the middle. The area of the membrane in Figure 4.8 is highlighted in blue and next to it is a close-up of the area, showing the layout of the holes. When an electric current is forced through the membrane, Joule heating occurs and only the area of the membrane is heated (Protochips, 2020). This results in the ability to ramp temperature rates up to $1000\,^{\circ}\mathrm{C\,ms^{-1}}$ (Protochips, n.d.(a)). The electrodes are connected to the sample holder by metal pins. An overview of the sample holder is shown in Figure 4.9.

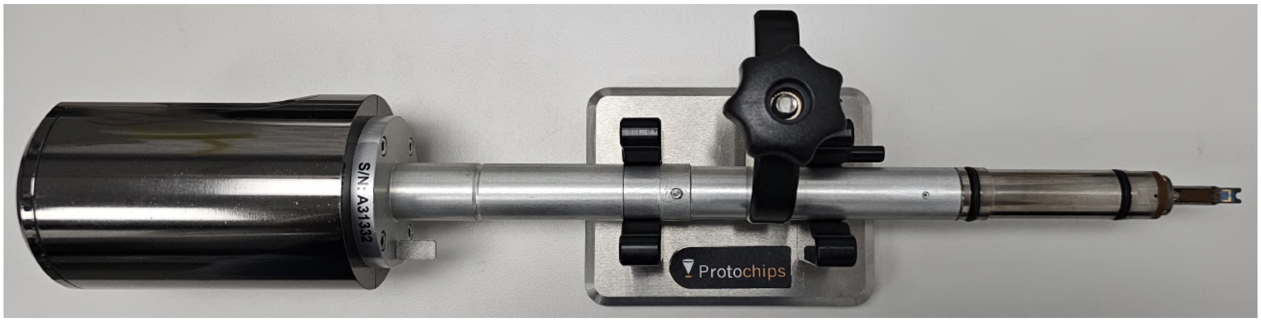

Figure 4.9: Overview Aduro sample holder

The Aduro sample holder has metal pins on the top (right) that hold the E-chip securely in place and provide electrical contact. The holder has four contacts on the back (left, behind the grip) that connect to the power supply.

The Aduro sample holder connects the sample to the peripherals and allows the user to control the sample environment. It features four metal pins at the tip that connect to the chip. In Figure 4.9, the tip is on the right, holding an E-chip. These are used to hold the chip securely in place and provide an electrical connection to the chip. The back of the sample holder is connected to the Keithley power supply by four cables. The power supply controls the current that reaches the sample holder. The power supply is connected to a computer that allows the user to define the experimental environment using the Fusion 500 program. The software interface is shown in Figure 4.10.

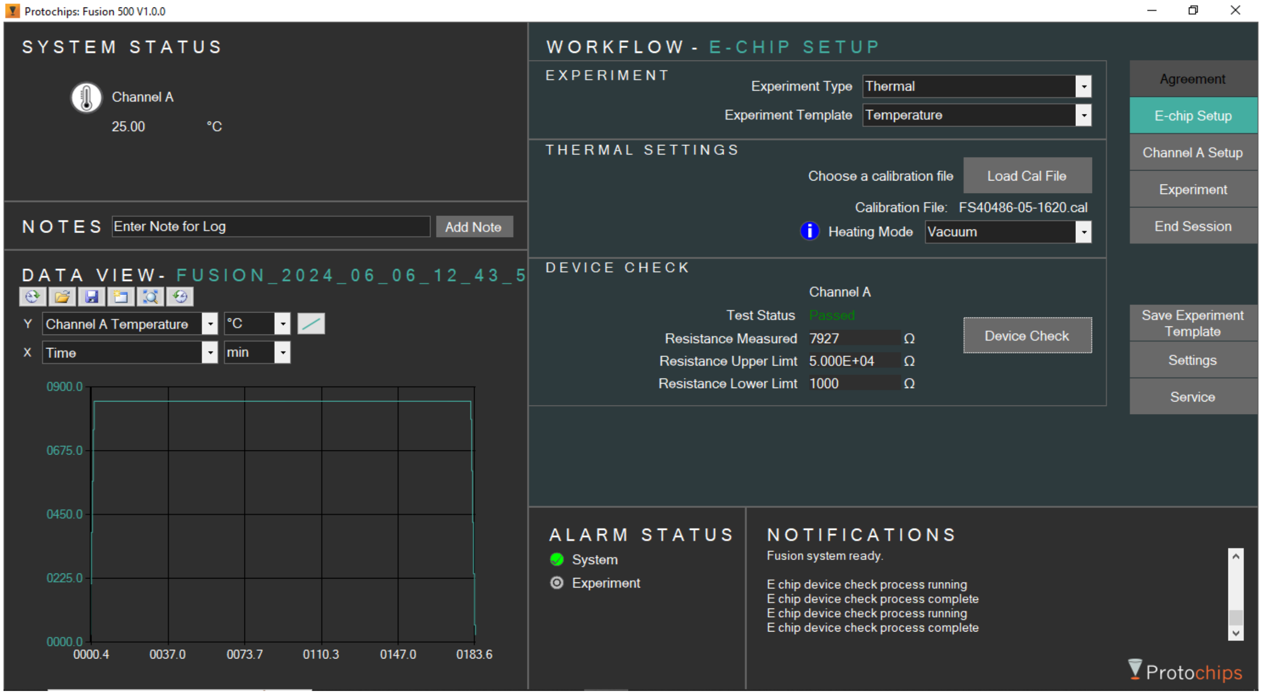

Channel A 25.00 °C

Enter Note for Log

Y: Channel A Temperature, °C
X: Time, min

Experiment Type: Thermal
Experiment Template: Temperature
Choose a calibration file
Calibration File: FS40486-05-1620.cal
Heating Mode: Vacuum

Channel A
Test Status: Passed
Resistance Measured: 7927 Ω
Resistance Upper Limt: 5.000E+04 Ω
Resistance Lower Limt: 1000 Ω

Fusion system ready.

E chip device check process running
E chip device check process complete
E chip device check process running
E chip device check process complete

Figure 4.10: Interface of Protochips Fusion 500

This program controls the experimental setup and environment of the Protochips system. The "System Status" monitors the current temperature. The "Workflow" sets up the experimental environment and checks for possible errors with the "DEvice Check". The "Data View" is used to monitor the progress of the experiment. (Protochips, 2024)

With this program it is possible to control the temperature of the sample as well as the time and rate. The program is divided into four main sections: "System Status", which displays the current temperature of the membrane, "Workflow", which controls the E-chip setup, "Data View", which monitors the temperature and time of the running experiment, and "Notifications", which logs the experimental process. In the Workflow section, the experiment type ("Thermal") and template ("Temperature") are set and the calibration file of the E-chip is loaded. For in situ experiments, the "Heating Mode" is "Vacuum". After the system is set up correctly, all cables are connected and the correct calibration file is loaded, the system must perform a "Device Check". This checks the entire system for possible errors by monitoring the resistance of the E-chip (Protochips, n.d.(e)). The result is displayed as "Passed" or "Failed" in the "Test Status". The Device Check must pass in order to proceed with the experiment to "Channel A Setup". An example of the interface is shown in Figure 4.11.

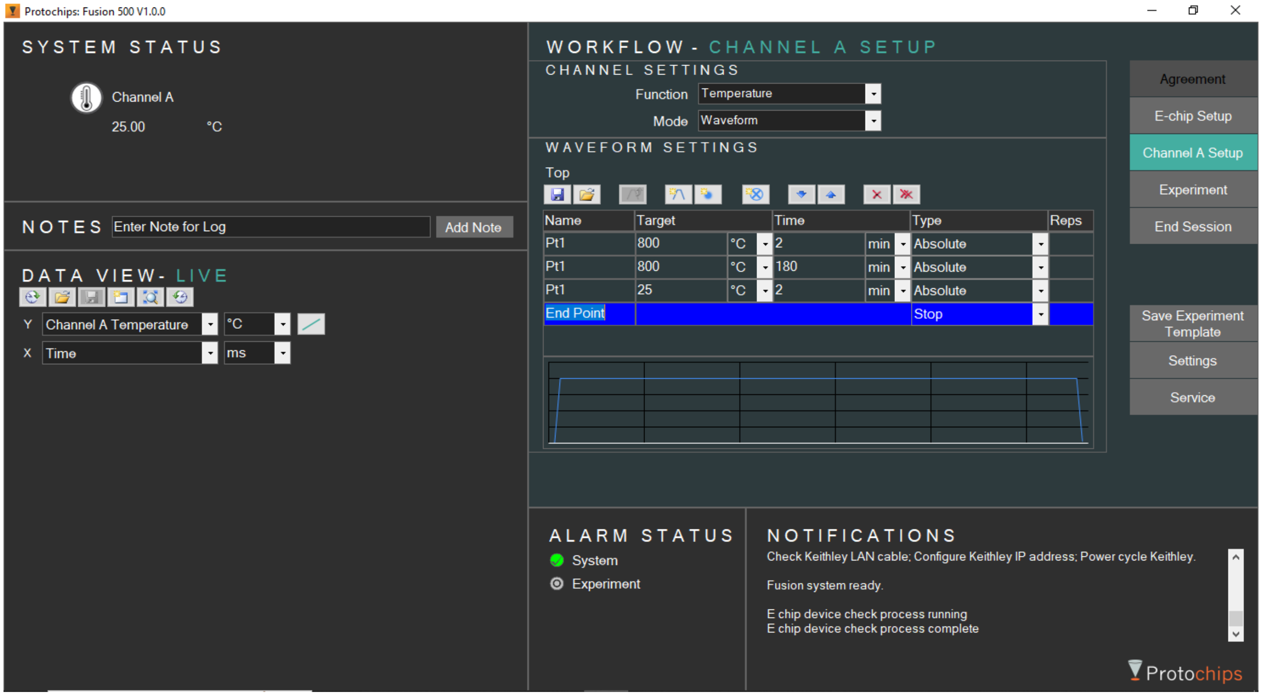

Channel A
25.00 °C

Enter Note for Log

Y Channel A Temperature °C
X Time ms

Function Temperature
Mode Waveform

Name	Target		Time		Type	Reps
Pt1	800	°C	2	min	Absolute	
Pt1	800	°C	180	min	Absolute	
Pt1	25	°C	2	min	Absolute	
End Point					Stop	

● System
○ Experiment

Check Keithley LAN cable; Configure Keithley IP address; Power cycle Keithley.

Fusion system ready.

E chip device check process running
E chip device check process complete

Figure 4.11: Fusion 500 - Channel a setup

After a successful "Device Check", the "Waveform" function can be used to set up the course of the experiment. The start and target temperatures can be set, as well as the temperature hold time, even for multiple cycles. The experiment must be terminated with an "End Point". (Protochips, 2024)

This is an example of the setup process for an experiment. In the Workflow section, the "Function" is already set with the E-chip setup. The "Waveform" mode is selected for the automatic course of an experiment. In this mode, the start and target temperatures, the heating and cooling rates, as well as the temperature hold time are set. This can be repeated for several cycles and the experiment must be completed with an "End Point".

5 Investigation of Phase Transformation of TiO_2

After introducing Titania, reviewing the current state of the art and outlining the Protochips system for in situ experiments with the TEM, the study of the thermal stability of Titania can be pursued. The goal is to study the transformation of anatase to rutile as a function of time and heat. First, the preparation and the experimental procedure are given, followed by a detailed discussion of the results. Since the results are not consistent with those reported in the literature, potential sources of error are analyzed to identify possible reasons.

5.1 Experimental Procedure

To study the thermal stability of Titania, the Protochips system is used with the Aduro sample holder. The sample is applied to the Fusion Select Heating E-chip (Serial No. FS40486-9). The sample used is the AEROXIDE® TiO_2 P25 from Evonik with an average particle size of 24 nm.

For sample preparation, the titania powder must be diluted in a solution to be applied to the membrane of the chip (Protochips, n.d.(d)). The Titania particles in the powder have agglomerated during the manufacturing process and are too large to observe the transformation of the particles (Evonik, 2017). In addition, the thickness of the applied sample is not controllable in powder form. Therefore, dilution of the powder results in a more dispersed sample, which is advantageous for TEM observation. The most commonly used solution is acetone (Lee and Zuo, 2004; Lee and Zuo, 2011). In a glass container, 3 ml of acetone is combined with a small amount of titania powder, about enough to cover the tip of a microspatula. The glass container is then placed in a sonic bath for 60 min to break up and disperse the agglomerates (Protochips, n.d.(c)). The finished solution is then dropped onto the front of the membrane of the E-chip. The chip needs to rest so that the acetone evaporates completely and does not cause problems in the vacuum chamber of the TEM.

After sample preparation, the Protochips system must be set up. The power supply must be turned on and allowed to warm up for one hour before starting the experiment (Protochips, n.d.(b)). The sample is mounted on the Aduro sample holder and placed inside the TEM. The sample holder, power supply and computer are connected by cables. The program is started and the calibration file for the E-chip is loaded. The experimental procedure can be set up after the Device Check.

To begin the thermal stability study of Titania, it is advisable to follow the manufacturer's recommendations. Evonik states in the product sheet for AEROXIDE® TiO_2 P25 that the anatase phase transforms completely to rutile at 800 °C after 3 h (Evonik, 2017). Another study (Ayache et al., 2010) with similarly sized particles at 25 nm observed a complete transformation at 900 °C after 3 h. Since the transformation rate seems to be correlated with the particle size and the growth of the particle with temperature, several experiments are performed with temperatures ranging from 800 °C to 1000 °C. The time held at the temperature is always 3 h. This covers the entire temperature range that the Protochips system is capable of, coupled with the time used by other studies.

This should also give an overview of the change in behavior with increasing temperature.

5.2 Discussion of Results

The same portion of the sample was observed in image mode and diffraction mode. In image mode, the change in particle size and shape can be observed. The change in crystal structure from anatase to rutile can be seen at the highest magnifications as the lattice spacing changes. The change in image mode is shown in Figure 5.1 at a magnification of x4000 in GIF mode.

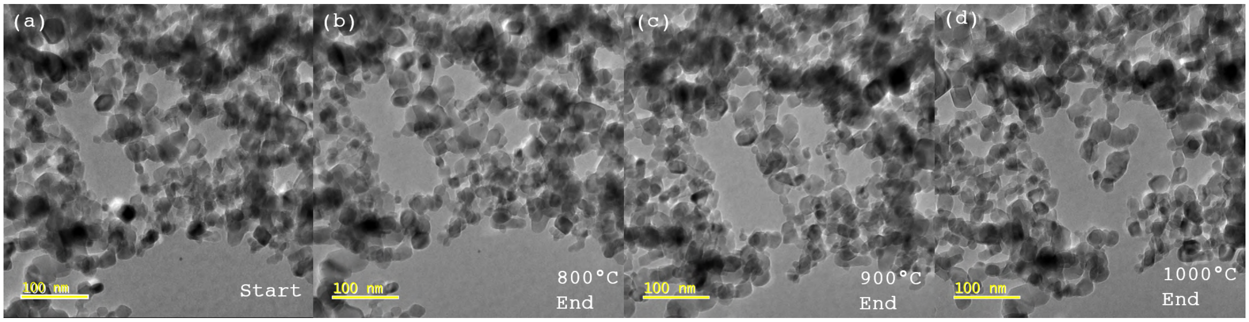

Figure 5.1: Evolution of Titania in image mode

The change in particle size, shape and distribution can be seen at a magnification of x2000 in GIF mode. The first image is before the heat treatment (a) and the adjacent images are after each experiment. After 3 hours at 800°C (b), the changes are small. After another 3 hours at 900°C (c), the features on the sample begin to change. After another 3 hours at 1000°C (d), there is a clear change. This could indicate a transformation from anatase to rutile.

On the left (a) is the observed location of the sample before any heat treatment. This location was chosen because the particles have a good distribution and the "lakes" in the center are distinct features that enhance a visual change of the particles. They also serve as a landmark to find the same location for each experiment. After each experiment, the images (b-d) in Figure 5.1 were taken. The sample was heated for 3 h at 800 °C (b), 900 °C (c) and 1000 °C (d). There is a clear visual change in the shape and distribution of the particles, especially after heating to 1000 °C. The particles appear to coalesce into a droplet-like shape. This is not melting of the particles as the melting temperature of TiO_2 is at 1843 °C (Kurt J. Lesker Company GmbH, 2020). This behavior is also observed in the literature as anatase usually grows in particle size by morphing together before transforming to rutile (Bachina et al., 2021). To confirm a complete transformation from anatase to rutile in image mode, the d-spacing of the particle can be measured at the highest magnification. The d-spacing for anatase in plane [1 0 1] is $d_{a1} = 3.52\,\text{Å}$ and for rutile in plane [1 1 0] $d_{r1} = 3.25\,\text{Å}$ (Hanaor and Sorrell, 2011). However, a first observation at high magnification of single particles shows only the lattice structure of anatase. An example is shown in Figure 5.2.

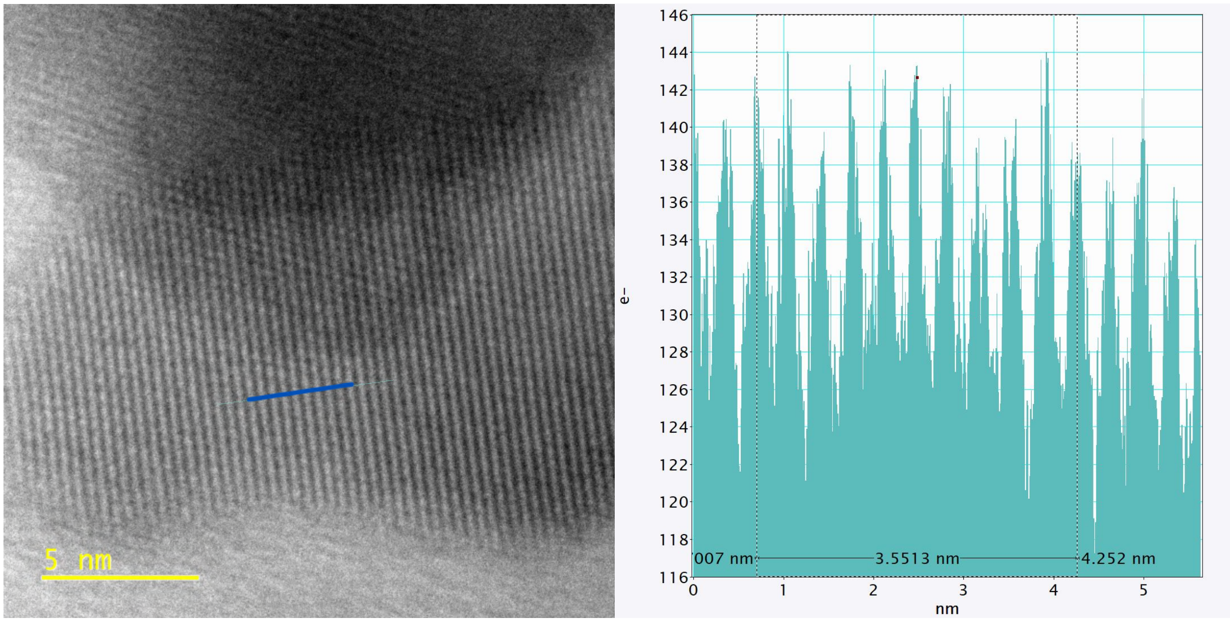

Figure 5.2: High magnification measurement of lattice spacing

High magnification image taken at x1.2M of a single particle (left) after the experiments. The measurement was done with DigitalMicrograph over multiple lattice spacings (right, Gatan Inc., 2024). The measured distance in nm on the x-axis and the number of electrons on the y-axis representing the intensity. The distance measured over 10 spacings is 3.55 nm. The lattice spacing corresponds to anatase (Rezaee et al., 2011).

The measurement was made at a magnification of x120k in GIF mode. The measurement, shown in Figure 5.2 as a blue line, was made over several lengths of the lattice to reduce the measurement error. This results in a measured distance of 3.55 Å for the lattice spacing and corresponds to anatase (3.52 Å, Rezaee et al., 2011). Thus, even after heating the sample to 1000 °C for several hours, it did not completely transform from anatase to rutile. Since this measurement can only test a small fraction of the total amount of particles, analysis of the diffraction pattern should give a clearer picture of the overall behavior of the material. Analysis of the diffraction patterns for different amounts of heating can also be used to try to track the kinetics of the transformation. The change in the diffraction pattern over different temperatures is shown in Figure 5.3.

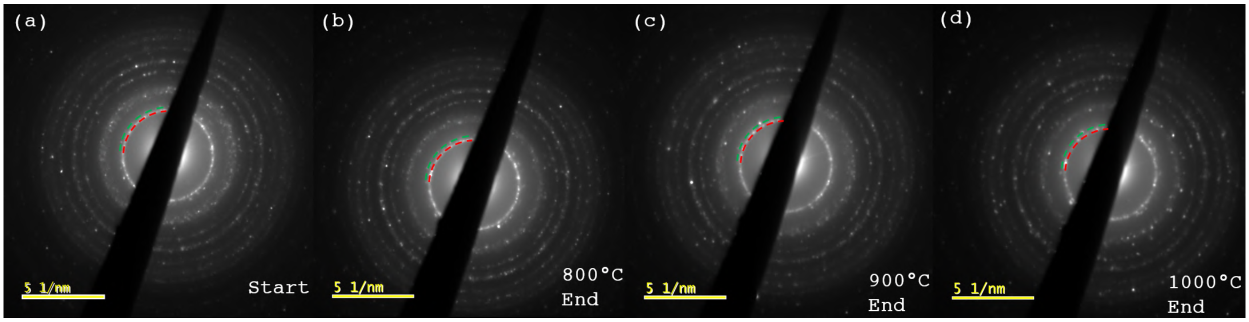

Figure 5.3: Evolution of Titania in diffraction mode

The change in the diffraction pattern over the course of the experiment can be seen at a camera length of 5cm. The first image is before heat treatment (a) and shows a prominent first anatase ring with some spots around it corresponding to the first rutile ring. For clarification, the first rings for both phases are highlighted with a dotted line (red = anatase, green = rutile). The adjacent images are after each experiment. After 3 hours at 800°C (b) and 900°C (c) there is no change. After another 3 hours at 1000°C (d), there appear to be more dots at the distance corresponding to the rutile ring. This could indicate a transformation from anatase to rutile at the highest temperature.

The diffraction pattern of Titania was measured at the same location as in Figure 5.1 with a camera length of 5cm. For reference, the first diffraction ring for anatase (red) and rutile (green) is shown in Figure 5.3. The first diffraction ring for anatase has the radius $r_{a1} = 2.8\,1/\text{nm}$ (Rezaee et al., 2011) and the first for rutile $r_{r1} = 3.1\,1/\text{nm}$ (NAVROTSKY and KLEPPA, 1967) in reciprocal space. The focus of the analysis is on the first ring for each phase as it has the highest intensity. In Figure 5.3 on the left (a) is the diffraction pattern before any heat treatment. It has a prominent first anatase ring. Around the anatase ring there are some spots corresponding to the first rutile ring. This means that the majority of the particles are in the anatase phase with some rutile particles in between. This corresponds to the specification given by Evonik for AEROXIDE® TiO_2 P25, as it should contain 85% anatase and 15% rutile. The following diffraction patterns in Figure 5.3 were taken after each subsequent heat treatment for 3 h at 800 °C (b), 900 °C (c) and 1000 °C (d). There seems to be a slight change in the intensity of the rutile ring during the experiment. There are more spots in the rutile ring at the end of the experiment compared to the beginning. To quantify the change in intensity of the first ring of each phase over the duration of the experiment, "CrysTBox" is used. This program can measure the change in intensity over the area of each ring by plotting the intensity over the distance to the central beam. This plot is shown in Figure 5.4.

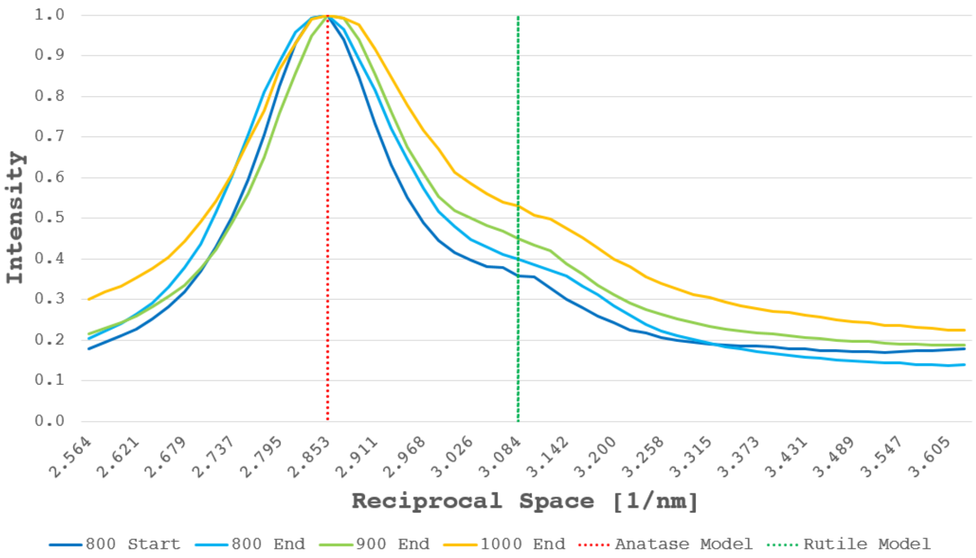

Figure 5.4: Intensity change during the experiment

Overview of the intensity changes of the first peaks of each phase during the experiments. The intensity (y-axis) versus the distance from the central beam in reciprocal space in 1/nm (x-axis). The plots correspond to the intensity at different temperatures. The first ring for each phase is indicated by a dotted line (red = anatase, green = rutile). There is an increase in intensity with increasing temperature and time at the peak of the first ring of rutile. However, an overall increase in intensity could be due to an increase in background noise from the SiN film of the membrane.

The goal is to measure a change in the intensity of the rutile over the course of the experiment. On the y-axis of the graph in Figure 5.4 is the intensity of the ring. Here the highest intensity value is 1 and is always located at the spot with the brightest ring. In this case at the peak of the first diffraction ring of anatase. The x-axis is the distance from the central beam in reciprocal space, ranging from 2.564 1/nm to 3.605 1/nm which includes the peak of the first ring of both anatase and rutile. The radius of the first ring of the model of the two phases is shown with a dotted line in red for anatase (2.844 1/nm, Rezaee et al., 2011) and green for rutile (3.078 1/nm, NAVROTSKY and KLEPPA, 1967). The plots correspond to the measurements. Dark blue is the first measurement before heat treatment, light blue after 3 h at 800 °C, green after 900 °C and orange after 1000 °C. All measurements are calibrated to the first anatase ring to match the peak of the model at 2.844 1/nm. There is a clear trend of increasing intensity with increasing time and heat during the experiment. The intensity of the first rutile ring starts at 0.357 before the heat treatment. After 3 h at 800 °C the intensity increases to 0.387. After 3 h at 900 °C the intensity increases further to 0.434. Finally, after 3 h at 1000 °C the intensity reaches 0.532. The change in intensity at the distance of the first rutile ring could indicate a partial transformation to rutile. However, it is also noteworthy that the overall intensity of the measurements, even between the rings, increases. So the higher intensity could also be due to increased background noise. This noise cannot be completely subtracted because the SiN of the membrane is always present.

Regardless of the small effect, the change in intensity is still far too small compared to the literature and the product specifications given by Evonik. The sample should transform completely from anatase to rutile after 3 h at 800 °C (Evonik, 2017). The sample was heated for a total of 9 h at temperatures above 800 °C. Further experiments were carried out with similar results. Another in situ measurement was done where the sample was dropped on the back of the E-chip to see if the contamination of the electrical contact had any effect on the resulting current. An experiment was also performed outside the TEM to see how pressure and oxygen could affect the transformation. The procedure was the same for all experiments and delivered the same result that the anatase phase has only slightly transformed to rutile. The only experiment in the literature with similar results (complete transformation after 8 h at 1000 °C) used Titania with an average particle size of 100 nm (Gouma and Mills, 2001). The fact that a complete phase transformation from anatase to rutile did not occur and that the temperature limits of the holder were reached could be due to a possible error that could have affected the experiments. The error could be in the sample used, the preparation method, the calibration of the system, or the functionality of the sample holder. A thorough error analysis should provide valuable insight.

5.3 System Error Analysis

The results of the measurement contradict the research on Titania's behavior gathered over the last 70 years. An error in the experimental system is the most likely scenario for this case. To begin the analysis of the system failure, it is advantageous to check whether the temperature of the heating system reaches the sample. The most effective way to do this is to test the system with a sample of known melting point and crystalline structure in the solid state. At the melting point the crystalline structure breaks down. This can be seen in diffraction mode as the rings of the diffraction pattern disappear (Borchardt-Ott and Sowa, 2018). The goal is to heat the sample and see if the temperature displayed matches the temperature reached. This is a way to test the heating capabilities of the system.

Aluminum (Al) was chosen to test the heating system because the melting point is at 660.3 °C (American Elements, 2024) and well within the heating range of the Protochips system. The sample was sputtered on the back of the E-chip because it would otherwise shorten the electrical circuit on the front and fail the device check. Sputtering the sample on the membrane of the chip ensures close contact between the membrane and the sample. The sputtered aluminum sample and a TEM image of the sample are shown in Figure 5.5.

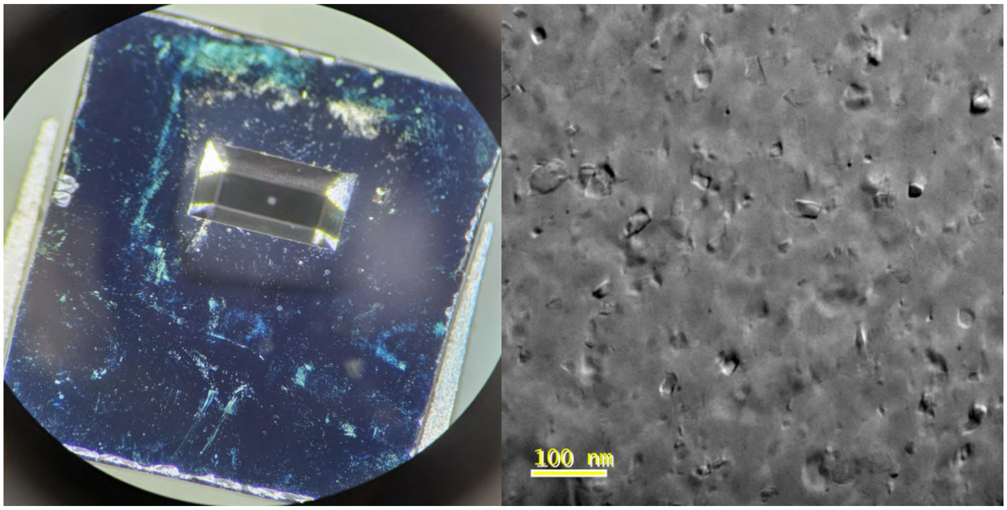

Figure 5.5: Overview of the sputtered aluminum sample

Image of the sputtered aluminum sample under a light microscope (left) and a TEM (right) at x2500 magnification in GIF mode.

On the left is the sputtered E-chip from behind. The sputtered aluminum can be seen as a gray/silver looking shadow. The sputtered layer is 30 nm ±5 nm thick. On the right in Figure 5.5 is a TEM image of the aluminum at a magnification of x2500 in GIF mode. For the heating experiment, the sample was mounted in the Aduro sample holder and the correct calibration file for the E-chip (serial no. FS40486-5) was loaded. The temperature was manually set and slowly increased. During the experiment the sample was observed in diffraction mode and the results are shown in Figure 5.6.

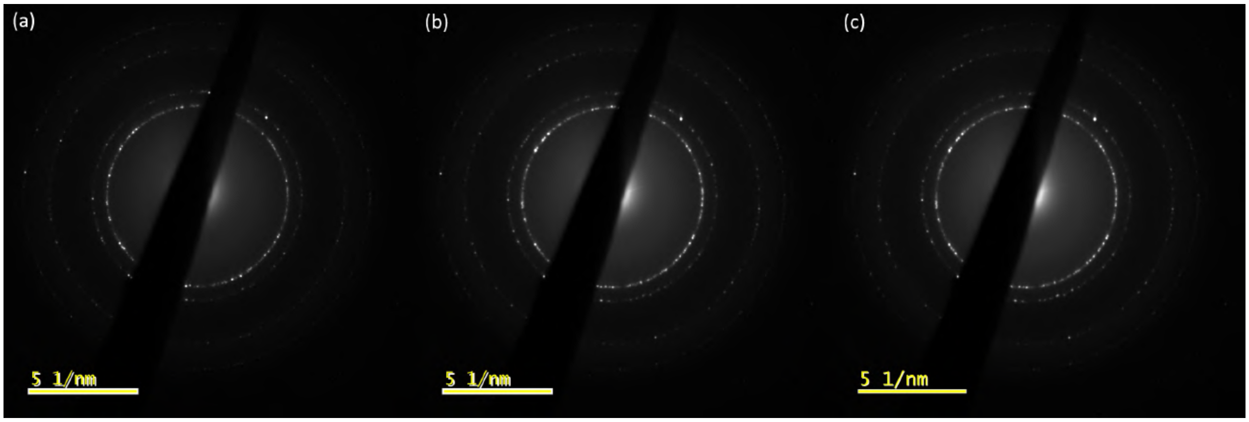

Figure 5.6: Al melting point test in diffraction mode

Diffraction pattern of aluminum at a camera length of 5cm. The rings are clearly visible throughout the experiment, before any heat treatment (a), at the theoretical melting point of 660°C (b, American Elements, 2024) and at the highest temperature possible with the heating system at 1000°C (c). No disappearance indicates that the temperature required to melt aluminum has not reached the sample or is not generated by the sample holder.

Shown are the diffraction patterns before (a), during (b) and at the end (c) of the experiment at a camera length of 5cm. On the left in Figure 5.6 is the diffraction pattern of aluminum before the experiment at room temperature. In the middle is the diffraction pattern at the theoretical melting point of 660 °C and on the right is the diffraction pattern at the highest possible temperature of 1000 °C. No change in the diffraction pattern indicates that the sample didn't melt until the temperature limit of the sample holder was reached. The experiment took a total of 30 min, which rules out the possibility that the heat didn't have enough time to reach the sample. With a thickness of about 30 nm, the sample is also thin enough to change immediately when the melting temperature is reached. However, during the experiment, the height of the sample changed because the focus had to be adjusted. This confirms that there is a temperature change (Protochips, n.d.(a)), just not high enough for the sample to melt. This could be due to a calibration error when setting up the system.

To further test this hypothesis, another sample with a lower melting point was selected. Zinc (Zn) has a melting point of 419.5 °C (American Elements, 2024). For the experiment, zinc nanoparticles (SkySpring Nanomaterials Inc. #9921XH) were dropped onto the front of the E-chip. The particles were not diluted to reduce the formation of ZnO as the melting point increases to 1975 °C (International Labor Organization, 2017). The disadvantage of this sample preparation is that the size and dispersion of the nanoparticles cannot be controlled and larger aggregates are formed. The particle size is between 80 nm and 100 nm (Skyspring nanomaterials, n.d.). An example for the zinc sample is shown in Figure 5.7.

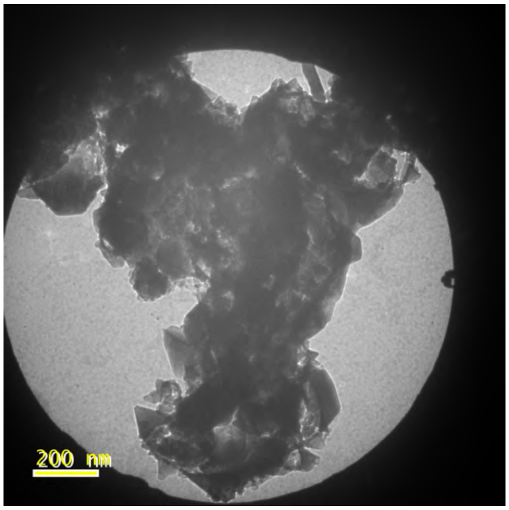

Figure 5.7: Overview of zinc nanoparticles

Image of zinc nanoparticles at x1200 magnification in GIF mode. The particles stick together and form a thicker layer as the particles are applied in powder form directly to the membrane.

The image is taken at x1200 magnification in GIF mode. It is clearly visible that the particles stick together due to the sample preparation. The setup was the same as for the sputtered aluminum sample with the correct calibration file for the E-chip (serial no. FS40486-7). The temperature was set manually and increased slowly. The sample was observed in diffraction mode during the experiment. The evolution of the diffraction pattern is shown in Figure 5.8.

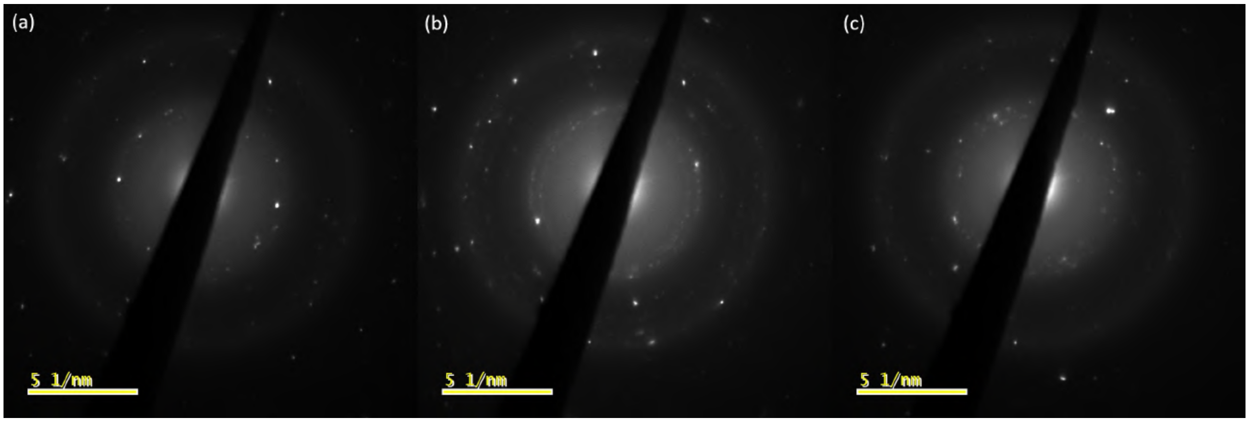

Figure 5.8: Zn melting point test in diffraction mode

Diffraction pattern of zinc at a camera length of 5cm. The rings are clearly visible throughout the experiment, before any heat treatment (a), at the theoretical melting point of 420°C (b, American Elements, 2024) and at the highest temperature possible with the heating system at 1000°C (c). No disappearance indicates that the temperature required to melt zinc has not reached the sample or is not generated by the sample holder.

Shown are the diffraction patterns before (a), during (b) and at the end (c) of the experiment at the camera length of 5cm. On the left in Figure 5.8 is the diffraction pattern of zinc before any heating. In the middle is the diffraction pattern at the theoretical melting point of 420 °C and on the right is the diffraction pattern at the highest possible temperature of 1000 °C. There is a slight change in the diffraction pattern between (b) and (c). The outer rings appear to be fading slowly. This could indicate an approach to the melting temperature. However, since the rings of the diffraction pattern are still clearly visible at 1000 °C after 30 min, the sample has not melted.

The conclusion of the experiments is that the Protochips system does not reach the specified temperature. The system heats up the sample somewhat due to the change in z-height and focus that must be adjusted as the temperature rises (Protochips, n.d.(a)). The most likely cause of this result is an incorrect calibration of the system. Normally the system is first set up and calibrated by a Protochips technician. This was done a year prior to this investigation. There may be an error in the calibration file or settings. A slight transformation from anatase to rutile supports the hypothesis that some heat is reaching the sample, although not at the specified parameters.

Given the minimal transformation of Titania from anatase to rutile during the experiments and the fact that the melting points of aluminum and zinc were not reached, the maximum temperature reached by the system is estimated to be below 420 °C, despite being set to 1000 °C. The slight transformation of anatase particles to rutile and the observed change in z-height indicate some heat generation. A rough estimate suggests the actual maximum temperature reached was around 400 °C, aligning with the lowest reported temperature for anatase to rutile transformation. Due to time constraints, further investigation of this hypothesis was not feasible. The next step is to have Protochips check and recalibrate the system, after which the investigation of the transformation temperature of Evonik's Titania can begin.

5.4 Resume

The purpose of the study is to observe the transformation from anatase to rutile. For the sample the AEROXIDE® TiO_2 P25 from Evonik with an average particle size of 24 nm was used. The powder is diluted in 3 ml acetone solution and dispersed in a 60 min sonic bath. The Titania should completely transform from anatase to rutile after 3 h at 800 °C.

The sample was heated several times in situ using the Protochips Aduro sample holder. For 3 h starting at 800 °C, 900 °C and 1000 °C. In image mode, only a slight change in particle size and shape was observed. The intensity of the first rutile ring in diffraction mode increased over the course of the experiment. This indicates a partial transformation of the sample from anatase to rutile. However, the amount transformed is only a fraction of the total amount of particles. Heating the sample for a total of 9 h at temperatures above 800 °C with only a small amount of transformation indicates an error in the experimental procedure. Repeating the experiment with different sample applications (dropped on the front and back of the chip) and heating outside the TEM leads to the hypothesis that there may be an error in the heating system.

The heating system was tested with zinc nanoparticles and sputtered aluminum because of their low melting point. Their crystalline structure changes as they melt and this can be observed in diffraction mode by the disappearance of the rings. The Protochips system couldn't reach the melting point of either sample (Al = 660.3 °C, Zn = 419.5 °C). This indicates that the calibration of the system is incorrect, so the displayed temperature and the actual temperature reached are different. The change in z-height during heating is due to thermal expansion of the membrane and sample and indicates that some heat is being generated.

The temperature reached is estimated to be about 400 °C. This is due to the partial transformation of anatase to rutile and not reaching the melting point of zinc. The lowest reported transformation temperature for anatase is 400 °C. The heating system must be checked and recalibrated by Protochips to ensure that the displayed temperature aligns with the actual temperature achieved. Once this is done, the investigation into the transformation temperature of Evonik's Titania powder can proceed.

6 Conclusion

The primary objective of this investigation was to commission a newly implemented external VS camera system and study the transformation of anatase to rutile using in situ transmission electron microscopy. Throughout the study, two key aspects were investigated: the performance of the external camera system and the evaluation of the phase transformation of TiO_2, focusing on potential errors in the heating system.

The external VS camera, mounted on a custom-built tripod, proved to be an effective alternative to the internal post-GIF TEM camera, with advantages and trade-offs. While the GIF camera offered superior magnification levels, higher pixel resolution and better contrast, the external VS camera excelled with its significantly larger field of view, which is 23 times larger at equivalent magnification levels. This advantage, combined with its stability and resistance to electron beam damage, makes the external camera system highly reliable, especially for long-term experiments where interruptions due to equipment failure could hinder progress. In addition, the external system was easier to operate and less prone to damage, making it a user-friendly alternative for routine tasks.

However, when the precision of the two systems was compared, it was found that the GIF camera had a lower measurement error in both diffraction mode (0.6%) and image mode (-2.6%), making it the more accurate system for detailed sample analysis. Nevertheless, the external camera system met the accuracy requirements for general TEM applications, below 5%, and its ease of use made it a valuable addition to the lab's toolkit.

As for the in situ heating experiments, AEROXIDE® TiO_2 P25 from Evonik, with an average particle size of 24 nm, was used as the sample. The sample was subjected to heat treatments at temperatures of 800 °C, 900 °C and 1000 °C for a total of 9 h. The expected full transformation from anatase to rutile, typically observed after 3 h at 800 °C (Evonik, 2017), was not achieved. Despite repeated heating, only minor changes in particle size and shape were observed, along with a marginal increase in rutile intensity in the diffraction mode. This indicated incomplete transformation, suggesting an underlying problem with the experimental procedure.

Further tests using sputtered aluminum and zinc nanoparticles with known melting points at 660.3 °C and 419.5 °C (American Elements, 2024), respectively, revealed that the Protochips heating system was unable to reach the melting points of either material. This observation indicated a calibration error in the system, as the temperatures displayed did not match the actual temperatures reached. The transformation from anatase to rutile began at approximately 400 °C, which is consistent with the lowest reported transformation temperature for this phase transition. However, this was well below the intended temperature of 800 °C.

To resolve this issue, the heating system will need to be recalibrated by Protochips to ensure that the temperatures displayed on the system accurately reflect the actual temperatures achieved during the experiments. Once this recalibration is complete, further studies can begin to more accurately determine the transformation temperature of the Evonik titania powder. By addressing this calibration issue, the phase transformation behavior of TiO_2 can be studied in more detail, providing valuable insight into its properties at high temperatures.

In addition, studying the influence of different particle sizes on the transformation temperature could provide deeper insights into the thermodynamic behavior of TiO_2. The integration of advanced analytical tools, such as real-time monitoring, as well as combined heating and electrical manipulation techniques, could improve the understanding of phase stability and transformation kinetics in nanocrystalline materials. These future investigations will help to optimize the use of TiO_2 in various applications, from photocatalysis to energy storage.

References

American Elements. (2024). *Reference sheet: Melting points*. Retrieved October 13, 2024, from https://www.americanelements.com/zinc-nanoparticles-7440-66-6

Ayache, J., Beaunier, L., Boumendil, J., Ehret, G., & Laub, D. (2010). *Sample preparation handbook for transmission electron microscopy*. Springer.

Bachina, Almjasheva, O., Popkov, V., Nevedomskiy, V., & Gusarov, V. (2021). Heat-stimulated crystallization and phase transformation of titania nanoparticles. *Journal of Crystal Growth*, *576*.

Banfield, J. F., Bischoff, B. L., & Anderson, M. A. (1993). Tio2 accessory minerals: Coarsening, and transformation kinetics in pure and doped synthetic nanocrystalline materials. *Chemical Geology*, *110*, 211–231.

Beun, R. J. (1994). *Introduction to the electron microscope*. Instituut voor Perceptie Onderzoek (IPO).

Borchardt-Ott, W., & Sowa, H. (2018). *Kristallographie: Eine einführung für studierende der naturwissenschaften*. Springer.

Buschow, J., Cahn, R., & Veyssière, P. (2001). *Encyclopedia of materials: Science and technology*. Elsevier.

Czanderna, A. W., Rao, C. N. R., & Honig, J. M. (1958). The anatase-rutile transition. part 1.—kinetics of the transformation of pure anatase. *Transaction of the Faraday Society*, *54*, 1069–1073.

DIN e.V. (1995). Fundamentals of metrology (DIN 1319:1995).

Evonik. (2017). *Aeroxide® - pyrogene metalloxide*. https://products.evonik.com/assets/49/30/TO_13_AEROXIDE_Pyrogene_Metalloxide_DE_DE_244930.pdf

Fultz, B., & Howe, J. (2013). *Transmission electron microscopy and diffractometry of materials* (4th ed.). Springer.

Gatan Inc. (2024). Digitalmicrograph (ver. 3.6.0).

Gouma, P. I., & Mills, M. J. (2001). Anatase-to-rutile transformation in titania powders. *Journal of the American Ceramic Society*, *84*(3), 619–622.

Gribb, A. A., & Banfield, J. F. (1997). Particle size effects on transformation kinetics and phase stability in nanocrystalline tio2. *American Mineralogist*, *82*, 717–728.

Hanaor, D. A. H., & Sorrell, C. C. (2011). Review of the anatase to rutile phase transformation. *46*, 855–874.

Hu, Y., Tsai, H.-L., & Huang, C.-L. (2003). Phase transformation of precipitated tio2 nanoparticles. *Materials Science and Engineering: A*, *344*, 209–214.

IIDA, Y., & OZAKI, S. (1961). Grain growth and phase transformation of titanium oxide during calcination. *Journal of the American Ceramic Society*, *44*(3), 120–127.

International Labor Organization. (2017). *Zinc oxide*. Retrieved October 13, 2024, from https://chemicalsafety.ilo.org/dyn/icsc/showcard.display?p_card_id=0208

JEOL. (n.d.). *JEM-2100plus*. Retrieved October 13, 2024, from https://www.jeol.com/download_catalogues.php#tem

Koparde, V. N., & Cummings, P. T. (2008). Phase transformations during sintering of titania nanoparticles. *ACS Nano*, *2*(8), 1620–1624.

Kurt J. Lesker Company GmbH. (2020). *Safety data sheet - titanium oxide (tio, tio2, ti2o3, ti3o5, ti4o7 powder and pieces)*. Retrieved October 13, 2024, from https://www.lesker.com/newweb/deposition_materials/pdf/msds_tio2.pdf

Labs, D. (2024). Dxo viewpoint (ver. 4.19).

Lee, G. H., & Zuo, J.-M. (2004). Growth and phase transformation of nanometer-sized titanium oxide powders produced by the precipitation method. *Journal of the American Ceramic Society*, *87*(3), 473–479.

Lee, G. H., & Zuo, J.-M. (2011). *TEM observation of growth and phase transformation in nanometer-sized titanium oxide powder* (Vol. 46). Journal of Materials Science.

Luo, Z. (2016). *A practical guide to transmission electron microscopy: Fundamentals*. Momentum Press.

Momma, K., & Izumi, F. (2024). *Vesta3 for three-dimensional visualization of crystal, volumetric and morphology data (ver. 3.5.8)*.

Murphy, D. (2012). *Fundamentals of light microscopy and electronic imaging* (2nd ed.). Wiley-Blackwell.

NAVROTSKY, A., & KLEPPA, O. (1967). Enthalpy of the anatase-rutile transformation. *Journal of the American Ceramic Society*, *50*(11).

Nikon. (2007). *Nikkor user's manual*. Retrieved October 13, 2024, from https://downloadcenter.nikonimglib.com/de/products/219/D60.html

Nikon. (2008). *Nikon D60 user's manual*. Retrieved October 13, 2024, from https://downloadcenter.nikonimglib.com/de/products/132/AF-S_DX_NIKKOR_18-55mm_f_35-56G_VR_II.html

Ntsikelelo, M., Malevu, T., Koao, L., Motloung, S., Tshwafo, M., & Shevchuk, V. (2020). Transformation from anatase to rutile titania using hydrothermal method:investigation of morphology and thermal stability. *Sensors and Materials*, *32*, 1511–1522.

Pella, T. (n.d.). *Technical notes: Magnification calibration diffraction grating replica product no. 607*. Retrieved October 13, 2024, from https://www.tedpella.com/technote_html/607%20TN.pdf

Peterson, B. (2010). *Understanding exposure: How to shoot great photographs with any camera* (3rd ed.). Amphoto Books.

Protochips. (2020). *Fusion select: E-chip ordering guide*. Retrieved October 13, 2024, from https://success.protochips.com/s/?language=en_US&t=1728856795488

Protochips. (2024). Fusion 500 (ver. 1.0.0).

Protochips. (n.d.[a]). *Application note: Thermal drift and settle times measured for different temperature excursions in the TEM*. Retrieved October 13, 2024, from https://success.protochips.com/s/?language=en_US&t=1728856795488

Protochips. (n.d.[b]). *Fusion user manual*. Retrieved October 13, 2024, from https://success.protochips.com/s/?language=en_US&t=1728856795488

Protochips. (n.d.[c]). *Sample prep: Fusion: Preparing one-dimensional nanostructures on fusion e-chips*. Retrieved October 13, 2024, from https://success.protochips.com/s/?language=en_US&t=1728856795488

Protochips. (n.d.[d]). *Sample prep: Preparing particles on fusion e-chips*. Retrieved October 13, 2024, from https://success.protochips.com/s/?language=en_US&t=1728856795488

Protochips. (n.d.[e]). *Technical note: Closed loop temerature control*. Retrieved October 13, 2024, from https://success.protochips.com/s/?language=en_US&t=1728856795488

Rahimi-Nasrabadi, H., Jin, J., Mazade, R., Pons, C., Najafian, S., & Alonso, J.-M. (2021). Image luminance changes contrast sensitivity in visual cortex. *Cell Reports*, *34*.

Reyes-Coronado, D., Rodríguez-Gattorno, G., Espinosa-Pesqueira, M. E., Cab, C., de Coss, R., & Oskam, G. (2008). Phase-pure tio2 nanoparticles: Anatase, brookite and rutile. *Nanotechnology*, *19*, 145605.

Rezaee, M., Mousavi Khoie, S. M., & Liu, K. H. (2011). The role of brookite in mechanical activation of anatase-to-rutile transformation of nanocrystalline tio2: An xrd and raman spectroscopy investigation. *CrystEngComm*, *13*, 5055–5061.

Skyspring nanomaterials. (n.d.). *Zinc nanopowder*. Retrieved October 13, 2024, from https://ssnano.com/inc/sdetail/zinc-nanoparticles--nanopowder---zn--99-9--80-100nm-/272?srsltid=AfmBOop_W5M-edJQ9IMLCj82YXMVlbIjwxqPgBm3MTXflF87VwprLI2V

Suzuki, A., & Tukuda, R. (1969). *Kinetics of the transition of titanium dioxide prepared by sulfate process and chloride process* (Vol. 42). Bulletin of the Chemical Society of Japan.

Vahldiek, F. (1966). Phase transition of titanium dioxide under various pressures. *Journal of the Less Common Metals*, *11*, 99–110.

Williams, D. B., & Carter, C. B. (2008). *Transmission electron eicroscopy: A textbook for materials science* (2nd ed.). Springer.

Wright, C., & Barrett, S. (2013). Biomimetic vision sensors. Elsevier.

Wyckoff, R. W. G. (1963). *Crystal structures - volume 1* (2nd ed.). Interscience Publishers.

Appendix

Table 6.1: Values for the intensity change during the experiment

800 Start		800 End		900 End		1000 End	
RS [1/nm]	Intensity	RS [1/nm]	Intensity	RS [1/nm]	Intensity	RS [1/nm]	Intensity
2.679	0.320	2.660	0.379	2.660	0.336	2.672	0.442
2.699	0.369	2.679	0.438	2.679	0.376	2.691	0.491
2.718	0.430	2.699	0.514	2.699	0.423	2.710	0.542
2.737	0.503	2.718	0.604	2.718	0.488	2.729	0.608
2.756	0.595	2.737	0.706	2.737	0.561	2.748	0.689
2.776	0.705	2.756	0.812	2.756	0.650	2.768	0.765
2.795	0.826	2.776	0.886	2.776	0.759	2.787	0.867
2.814	0.931	2.795	0.958	2.795	0.858	2.806	0.930
2.834	0.993	2.814	0.992	2.814	0.950	2.825	0.991
2.853	1.000	2.834	1.000	2.834	1.000	2.844	1.000
2.872	0.939	2.853	0.967	2.853	0.994	2.863	0.993
2.891	0.849	2.872	0.891	2.872	0.941	2.882	0.977
2.911	0.733	2.891	0.815	2.891	0.854	2.901	0.916
2.930	0.633	2.911	0.723	2.911	0.764	2.920	0.848
2.949	0.551	2.930	0.645	2.930	0.676	2.939	0.780
2.968	0.489	2.949	0.575	2.949	0.610	2.958	0.717
2.988	0.445	2.968	0.517	2.968	0.555	2.978	0.670
3.007	0.416	2.988	0.479	2.988	0.519	2.997	0.613
3.026	0.397	3.007	0.447	3.007	0.502	3.016	0.587
3.046	0.381	3.026	0.429	3.026	0.484	3.035	0.561
3.065	0.378	3.046	0.411	3.046	0.468	3.054	0.540
3.084	0.357	3.065	0.400	3.065	0.450	3.073	0.532
3.103	0.357	3.084	0.387	3.084	0.434	3.092	0.508
3.123	0.328	3.103	0.371	3.103	0.420	3.111	0.498
3.142	0.302	3.123	0.358	3.123	0.388	3.130	0.475
3.161	0.280	3.142	0.334	3.142	0.364	3.149	0.453
3.180	0.259	3.161	0.312	3.161	0.334	3.168	0.428
3.200	0.243	3.180	0.284	3.180	0.312	3.187	0.399
3.219	0.226	3.200	0.262	3.200	0.292	3.207	0.381
3.238	0.217	3.219	0.240	3.219	0.276	3.226	0.357
3.258	0.208	3.238	0.223	3.238	0.264	3.245	0.339

Values for the intensity plot in Figure 5.4. For each plot the values for Reciprocal Space (RS) and Intensity are shown. The values for the peaks of the first diffraction ring are highlighted in red for anatase and green for rutile.

Table 6.2: Calibration of the magnifications with line spacing

Magnification	Scale Bar [Pixel]	Length Square [Pixel]	Scale Bar [nm]
x15k	858	115	3454.1
x20k	872	154	2621.5
x25k	892	197	2096.3
x30k	863	227	1760.1
x40k	850	303	1298.7
x50k	864	381	1049.9
x60k	918	483	879.9
x80k	920	648	657.3
x100k	860	759	524.6
x120k	906	955	439.2
x150k	906	1214	345.5
x200k	1008	1848	252.5
x250k	1010	2229	209.7

Values for the calibration of the scale bar with the length of the gold standard in image mode. With the scale bar in pixels, the distance of between lines in pixel and the real distance (463 nm) the scale bar can be calibrated in nm.

Table 6.3: Calibration of the magnifications with defects

Magnification	Scale Bar [Pixel]	Measured Length [Pixel]	Scale Bar [nm]
x300k	607	1364	178.3
x400k	605	1355	135.7
x500k	761	907	106.6
x600k	1007	1927	88.8
x800k	1012	1922	63.4
x1M	1010	688	50.6
x1.2M	948	782	41.8

Values for the calibration of the scale bar with defects in the gold standard in image mode. With the scale bar in pixels, the length between two defects in pixel and nm the scale bar can be calibrated in nm.

Table 6.4: Calibration of the camera length

Magnification	Scale Bar [Pixel]	Area [Pixel]	Radius [Pixel]	Scale Bar [1/nm]
20cm	1388	11204	59.7	98.7
25cm	1382	17092	73.8	79.5
30cm	1380	24208	87.8	66.7
40cm	1386	43208	117.3	50.2
50cm	1382	66266	145.2	40.4
60cm	1386	97056	175.8	33.5
80cm	1378	162240	227.3	25.7
100cm	1382	258340	286.8	20.5
120cm	1381	382082	348.7	16.8
150cm	1384	593828	434.8	13.5
200cm	1380	1019838	569.8	10.3
250cm	1382	1630728	720.5	8.1

Values for the calibration of the scale bar in diffraction mode. With the scale bar in pixels, the radius of the first diffraction ring in pixel and 1/nm the scale bar can be calibrated in 1/nm. The radius in pixel is calculated from the area of the first diffraction ring in pixel.

Declaration of Authenticity

I hereby declare that the thesis on the above topic has been written independently, and no sources or aids other than those specified have been used, with verbatim and analogous quotations marked as such. As part of the double degree programme with the Institut national de la recherche scientifique, this thesis will only be submitted to Munich University of Applied Sciences and the Institut national de la recherche scientifique. It has not yet been submitted to any other examination authority and has not been published

Philipp Wieland, Munich, 14. October 2024